Field and Numerical Studies of an Instrumented Highway Embankment in Degrading Permafrost

By

David James Flynn

A Thesis submitted to the Faculty of Graduate Studies of

The University of Manitoba

in Partial Fulfillment of the Requirement for the Degree of

MASTER OF SCIENCE

Department of Civil Engineering

University of Manitoba

Winnipeg, Manitoba

Abstract

There is a growing need to improve the understanding of the behaviour of infrastructure in permafrost regions. Permafrost affects nearly half of the land surface in Canada, especially in the north. Further development of natural resources in northern Canada will provide socio-economic benefits to the region and its residents. Linear infrastructure, such as highways, is an important part of that development. The integrity of infrastructure in northern regions is negatively impacted by thawing and degradation of the underlying permafrost initiated by changes in both air and ground temperatures. Subsequent deformations due to settlement and lateral spreading can lead to potentially hazardous driving on highways.

The author's research focused on a section of highway embankment on Provincial Road (PR) 391 located 18 km north of Thompson, Manitoba. The purpose of the research was to further understanding of the thermal and deformation behaviour of an embankment subjected to degrading permafrost conditions. The author's research consisted of laboratory testing, instrumentation installation, data monitoring, and numerical modelling. Laboratory tests on four-inch (101.6 mm) diameter Shelby tube samples characterized the soil at the site. Data were collected remotely via satellite, and included ground temperatures, pore water pressures, and displacements both laterally and vertically. Ground temperatures indicated a frost bulb, a region of frozen ground, under the embankment. Thermal models using TEMP/W simulated the current ground thermal regime and projections of future thermal behaviour of the embankment. Deformation numerical models using SIGMA/W incorporated changes in the size of the frost bulb over a freeze-thaw cycle to simulate the deformation behaviour of the embankment. The numerical models were compared with the collected data.

Acknowledgements

Table of Contents

List of Figures

List of Copyrighted Figures for which Permission was Obtained

Chapter 1:   Introduction

1.1   Background

Permafrost affects nearly half of the ground surface in Canada, primarily in the north and high elevation regions. Isolated patches of permafrost a few metres thick, called sporadic discontinuous permafrost, on the northern edge of the boreal forest give way to continuous permafrost in the artic that may be several hundred metres thick. Permafrost is defined as ground, whether it is soil or rock, that has remained at a temperature colder than 0°C for a period of two or more consecutive years. Changes in air temperature can lead to changes in temperature at the ground surface and are accordingly reflected in the permafrost at lower depths. Air temperature changes occur due to factors such as fluctuations in meteorological conditions, precipitation, and wind speed. Natural phenomena and human activity both contribute to changing climate as a result of volcanic activity, solar radiation, and greenhouse gases. Regions containing permafrost are vulnerable to temperature changes that can lead to undesirable performance of local infrastructure. This is particularly true in regions of discontinuous permafrost where the average ground temperatures remain close to 0°C.

Development in the north is important in terms of social and economic benefits as well as national security and maintaining Canadian sovereignty. The Canadian North is sparsely populated and communities are often remotely connected. It is a matter of fairness and equality that these communities are provided the same standard of living and access to essential services as their southern counterparts. The north is home to large quantities of natural resources such as petro carbons, minerals, and hydro power. Transportation infrastructure is crucial to develop these vital resources and to provide services to the remote communities and their residents.

Canada is the second largest country in the world by land area and has more coastline than any other country, yet much of it is unprotected due to its inaccessibility. Thawing of summer ice could lead to increased shipping out of Churchill, Manitoba and potentially open the Northwest Passage. Development can strengthen Canadian sovereignty in the Arctic which has taken greater importance given the increased frequency of territorial disputes between several northern countries.

Highway, railroad and airport runway embankments have been, and continue to be, constructed in regions affected by permafrost. Construction in northern Canada uses similar procedures to those used in the south. In most cases, the fills have higher thermal conductivities than the original materials. This enhances heat transfer to underlying soils and leads to thawing of previously frozen ground. Asphalt pavement surfaces absorb a high amount of heat from the sun and transfer it into the embankments. Often, the degradation of the embankment begins at the toe and gradually extends into the centre.

Ground temperatures decrease over the winter. The freezing front gradually progresses deeper and subsequent changes in temperature at lower depths react more slowly compared to changes observed near the ground surface. Heaving can occur seasonally when the water freezes and expands to form ice lenses in frost susceptible soils such as silty sands, silts, and silty clays (Konrad, 2008). Distinct ice lenses develop due to the migration of water towards the freezing front due to negative water potentials. Thawing can occur naturally during spring or due to human activity such as construction. Disturbance of the existing ground cover can change the thermal regime beneath the surface and lead to thawing of ice lenses and permafrost (Hinkel et al. 2003). As thawing occurs, water from the melting ice moves towards the ground surface or is absorbed by the surrounding soil. Thawed soil is more compressible and weaker than frozen soil.

The soil deforms and weakens due to increased pore water pressures from the melting ice reducing the effective stresses and weakening the soil. The weakened soil often cannot tolerate the existing loads which results in settlements, lateral spreading, and reduced stability. The thickness and lateral extent of permafrost distribution can vary dramatically from location to location especially in regions of sporadic isolated permafrost. As a result, the consequences are non-uniform across a region and cause differential settlements, variable degrees of lateral spreading, and alternating stable and unstable sections of infrastructure. Linear and static infrastructure such as embankments and buildings can be severely affected to the point of serviceability or ultimate failure.

The design, construction, and maintenance of new infrastructure and refurbishment of existing infrastructure has to take into account the effects of building on foundation soils with engineering properties that may degrade due to climate change and land use. Construction in permafrost regions requires special attention and techniques. These techniques as well as more detailed information regarding permafrost conditions are discussed in Chapter 2.

Transport Canada, Manitoba Infrastructure and Transportation (MIT), and the University of Manitoba (UM) have collaborated to improve practices for the design and maintenance of highways constructed in permafrost regions. This thesis presents work at a project site located on an embankment of Provincial Road 391, located 18 km north-west of Thompson, Manitoba. The site is contains discontinuous permafrost and is the only road connection to mining towns, hydro generating stations, and First Nations communities in north-western Manitoba.

1.2   Hypothesis and Objectives

This thesis examines the following hypotheses:

(1) Frozen ground regions (frost bulbs) are still present under the existing PR 391 embankment.

(2) The main operating mechanism for the settlement of the road embankment at the PR 391 test site, in addition to thaw consolidation, is associated with shear straining of the thawed soils along the edge of the frost bulb under the middle of the embankment.

The objective of hypothesis (1) is to highlight the influence of frost bulbs on thermal regimes beneath road embankments in degrading permafrost regions. The objective of hypothesis (2) is to explain the deformation behaviour of the road embankment. The hypotheses will be addressed with a combination of a site investigation, instrumentation, field monitoring, laboratory testing, and numerical modelling. Instrumentation yielded pore water pressure, temperature, and displacement data, respectively. The data have been used to calibrate numerical models for the purpose of replicating the behaviour of the highway embankment at the project site. Material properties were obtained through laboratory tests and existing literature.

Secondary objectives were met while testing the hypotheses. These included the following:

(1) A remote monitoring system was developed to collect data from isolated project sites. Data were used to assess both hypothesis (1) and (2). A commercially available satellite system combined with a typical data acquisition system communicated to the site from any location with internet access in order to collect data or update the monitoring program.

(2) Laboratory tests were conducted on 4-inch (101.6 mm) diameter Shelby tube specimens to determine soil properties. The tests were used to classify the soil at the site. Previous laboratory tests used the more conventional 2-inch (50.8 mm) diameter specimens (Batenipour, 2012). Results of the two different sample sizes were compared for consistency.

1.3   Scope of Thesis

Research is being undertaken to improve understanding of mechanisms and processes associated with the performance of highway embankments on degrading permafrost. The focus of the author's research is a section of embankment along Provincial Road (PR) 391 located about 18 km north of Thompson, Manitoba. The project site has been used since October 2008 and contributed to the research of two PhD theses at the University of Manitoba (U of M).

Dr. Batenipour established an instrumentation-monitoring program at the PR 391 project site, contrasted results of laboratory tests performed at different temperatures, and developed frost heave predictions for unstable and stable sections of the highway embankment (Batenipour, 2012). The project site was one of two sites used by Dr. Kurz to develop a framework for the thermal modelling and an elasto-themo-viscoplastic (ETVP) model (Kurz, 2013).

The scope of this thesis is based on original research conducted by the author to build upon the previous projects at the same location. New field instrumentation, monitoring, laboratory testing, and numerical modelling were all included within the scope of this thesis. The continuity of research at the same locations provided a longer range of time over which data were collected at the toe and mid slope of the embankment.

In this project, new instrumentation was installed in September 2012 at the shoulder and centreline which were not permitted in the earlier research. A remote access data acquisition system was developed to collect data and modify the monitoring program. In the earlier research, data had to be collected on site on a monthly basis. Four-inch Shelby tube soil samples were procured and laboratory tests were conducted at the University of Manitoba. Numerical modelling consisted of thermal and load-deformation modelling. It used data collected from the project site, empirical relationships found in literature and laboratory tests from Kurz (2013).

1.4 Overview of Thesis

Following this Introduction in Chapter 1, Chapter 2 summarizes information related to understanding the work and concepts of the research project. The chapter describes the extent of permafrost, inherent material properties, and the challenges and approaches associated with engineering projects in permafrost regions.

Chapter 3 provides background information on PR 391 and the author's new investigations at the site. The chapter also includes information from earlier and recent drilling and the results of laboratory tests that determined index properties and mechanical properties of the soil.

Chapter 4 describes the instrumentation and monitoring program conducted as part of this research project. The instrumentation measures temperature, ground water, and movement. The section on the monitoring program describes the processes used to collect data. The collected data are presented and discussed.

Chapter 5 describes two types of numerical models that were developed specifically for the project site: thermal and load-deformation model. Modelling results are presented, analyzed, and compared with field measurements.

Chapter 6 summarizes the results of the project, states the author's conclusions, and suggests recommendations for future work. Data, pictures, reports, and papers related to the project are included in the Appendix. The folders in the Appendix are sorted by chapter.

Chapter 2: Literature Review

2.1 Introduction

This chapter provides background information on permafrost, its distribution and classification, common periglacial landforms, and properties of frozen and unfrozen soil. The chapter goes on to discuss the impact of climate change on permafrost and infrastructure before briefly reviewing four research sites used to study highway embankments in permafrost regions.

2.2 Permafrost

Permafrost is ground, either soil or rock, that remains at or below 0°C for two years or more (Williams, 1986). Two consecutive winters and summers is enough time to differentiate permafrost from the active layer, the layer near the ground surface subjected to an annual freeze-thaw cycle. Figure 2.1 shows an idealized temperature envelope called a trumpet curve for a particular location over a year. The annual maximum and minimum temperatures create the bell of the trumpet curve at the ground surface. The intersection of the maximum temperature and 0°C represents the transition between the active layer and the top of the permafrost table. The depth where the difference between the annual maximum and minimum temperatures is negligible is called the depth of mean zero annual amplitude (DMZAA). The ground below the DMZAA is warmed by a geothermal gradient typically between 2.5 to 3.0°C per 100 m (Fridleifsson et al., 2008). The depth at which the increasing average ground temperature intercepts the freezing point (or melting point) due to the geothermal gradients denotes the bottom of the permafrost layer.

2.3   The Extent of Permafrost

Permafrost affects approximately 20 to 25% of world's land surface area (Arenson, 2013). As shown in Figure 2.2 (Brown et al., 2001), permafrost is found extensively throughout the northern hemisphere in Canada, Alaska, Greenland, Russia, and China. In the southern hemisphere, permafrost is located in Antarctica and the Andes Mountains of South America. The extent of permafrost coverage in Canada is vast, as shown in Figure 2.3 (Smith et al., 2010). Permafrost affects nearly half of the land area in Canada (Brown, 1967). Aside from latitude and altitude, the occurrence of permafrost depends on various factors including solar radiation, vegetation, climate, snow accumulation, drainage, topography, and thermal properties at the ground surface (NRC, 2012). Permafrost is typically found at high latitudes but can also be observed at high altitudes in lower latitudes where it is referred to as alpine or mountain permafrost, most notably in the Qinghai-Tibetan Plateau in China. Alpine permafrost occurs in the mountains in western and eastern Canada as well. Subsea permafrost exists under the channels between some Arctic Islands in areas that were previously dry land prior to rising sea levels (NRC, 2012).

Ground ice is the general term for naturally occurring ice in the ground, and often occurs in permafrost terrains even though the strict definition of permafrost is related to the ground temperature. Ground ice forms broadly in three ways: (1) as small crystals coating the surfaces of soil particles called pore ice, (2) as layers of ice parallel to the ground surface called ice lenses or veins, and (3) as pure ice intrusions of assorted shapes (Hinkel et al., 2003). The presence of ground ice depends on the soil type as it is more commonly found in fine-grained and organic soils as opposed to coarse-grained soils (NRC, 2012).

Permafrost classification is divided into continuous, discontinuous, sporadic discontinuous, and isolated (NRC, 2012). The most northern regions of the Canadian Arctic are classified as continuous permafrost regions since permafrost is found everywhere beneath the ground surface except for under some lakes too deep to completely freeze (Batenipour, 2012). Discontinuous permafrost regions contain scattered patches of unfrozen and only 50% to 90% of the land area is affected by permafrost. Unfrozen ground becomes even more common in the sporadic discontinuous regions where permafrost only affects between 10% and 50% of a land area. Less than 10% of the land area is affected by permafrost in isolated permafrost regions such as central Manitoba near the north side of Lake Winnipeg.

The thickness of permafrost in each permafrost region varies as demonstrated in Figure 2.4 (Brown et al., 1981). The coldest and thickest permafrost can be found in high latitude and high altitude regions that have survived several glacial periods. The permafrost in Siberia is nearly 1500 m thick (French, 1996). In Canada, continuous permafrost can be as thick as 500 m in Resolute Bay while further south in Norman Wells, NT it is 40 to 60 m. Meanwhile, the thickness of permafrost in a sporadic discontinuous permafrost location like Hay River, NT ranges between 0 and 12 m (Arenson, 2013).

2.4 The Behaviour of Frozen Soil

The intrinsic mechanical and thermal properties of soil are significantly affected by changes in temperature. The implementation of engineering projects in permafrost regions requires understanding the impact of temperature changes on soil behaviour. The same understanding is also important for the selection of material properties used in the numerical modelling when actual laboratory test data are unavailable. Freeze-thaw processes and long-term temperature

changes influence the properties of frozen ground. Frozen soil contains soil particles, void space, liquid water, and ice. The physical, chemical, and mechanical properties of the individual components can be affected by heating and cooling (Ghahremannejad, 2003). Farouki (1986) summarized the effects that changes in soil temperature can have on various thermal properties including specific heat, thermal conductivity, thermal diffusivity, and unfrozen water content.

The heat capacity represents the heat added or subtracted from a substance as a result of temperature changes. The heat capacity of a soil depends on the water content and whether the soil is frozen or unfrozen. The latent heat of fusion of water (heat released during the phase change between ice and water) affects the thermal properties of soil. In fine-grained soils, heat is gradually released as the soil freezes, but the rate slows down at lower temperatures. The heat capacity in fine-grained soils spikes suddenly just below 0°C, and then drops quickly at lower temperatures (Low et al., 1968). An empirical formula provided by Andersland and Ladanyi (2004) calculates the heat capacity of a soil as a function of its dry density, unfrozen water content, and the heat capacity of its constituents.

The rate at which heat is transferred through a mass by conduction is called the thermal conductivity. Ice is four times more thermally conductive compared to liquid water, and the thermal conductivity of frozen soil is consequently greater than the same soil when unfrozen (Kurz, 2013). Johansen (1975) developed an empirical method to determine applicable thermal conductivities for frozen and unfrozen mineral soils. The equation uses the degree of saturation and the thermal conductivity of dry and saturated soils. The thermal conductivity of a soil increases with increases in dry density and/or the degree of saturation. Harlan and Nixon (1978) summarized a variety of empirically based techniques that define thermal conductivities based on soil type, dry density, water content, and degree of saturation. Techniques have been developed

to measure the thermal conductivity of soil directly using a thermal probe. For example, Kurz et al. (2012a) directly measured thermal conductivities with a thermal probe and compared the results to empirical methods. Kurz et al (2012a) carried out laboratory test on clay specimens from two project sites in Northern Manitoba (including the PR 391 project site) at four different temperatures: 10°C, 3°C, -10°C, and -16°C. The results demonstrated consistency with empirical methods developed (Harlan and Nixon, 1978) as shown in Figure 2.5 and Figure 2.6.

Frozen ground is less compressible than unfrozen ground and typically possesses higher strength in a three-phase system (soil, water, and ice) where the frozen ground contains unfrozen water. Wissa (1969) found sand particles cemented by ice drastically reduced the compressibility of the soil skeleton. The strength of frozen ground depends on soil density, ice content, salinity, the degree of confinement, and the strain rate (Andersland and Ladanyi, 2004).

Ting et al. (1983) divided the principal mechanisms of shear strength of frozen soil into three main categories: ice strength, soil strength, and the interaction between ice and soil. Ge et al. (2013) studied the mechanical properties of naturally frozen ice-rich silty soils. The study stated ultimate compressive strengths and Young's moduli decreased as temperatures increased in frozen soil and permafrost. Other researchers investigated the mechanical behaviour of frozen clay at high confining pressures under axial and triaxial compression found strength increased as temperatures decreased (Chang et al., 2008).

Early research suggested that the hydraulic conductivities of frozen and unfrozen soils were equivalent at the same water content, but this assumption often led to over-predictions of water flow. An impedance factor ranging between 1 and 1000, depending on total ice content, was introduced to reduce the hydraulic conductivity of frozen soils (Tarnawski and Wagner, 1996).

2.5 Periglacial Landforms

Periglacial landforms are features related to cold climates, and to past geomorphological processes not directly connected to glaciers. Heginbottom et al. (2012) stated that organizations like the U.S. Geological Survey expanded the definition to include features related to frost action especially freeze-thaw processes and permafrost. The identification of periglacial landforms can help establish the rough boundaries of permafrost using observational methods like aerial photography instead of more invasive techniques. The following paragraphs feature some common periglacial landforms and characteristics.

Most of the distinctive terrain features of permafrost and periglacial processes are related to ground ice (Heginbottom et al., 2012). When the ground freezes, the water in the soil seeks out the coldest part of the soil. According to the second law of thermodynamics, the net transfer of heat energy can only flow from a warmer body to a colder body and never in the opposite direction unless some external work is applied to the system. In winter, freezing air temperatures cause soil surface temperatures to drop below 0°C and the freezing front moves deeper into the ground (Farouki, 1986). Cryosuction, the suction in soil related to freezing, generates negative potentials and draws more water towards the freezing front to create segregated ice lenses.

Regions subjected to freeze-thaw cycles often experience frost action such as frost heaving or frost jacking. Frost action requires three main factors: freezing temperatures, water supply, and frost susceptible soil (Konrad and Lemieux, 2008). Frost heaving is the upward heaving of the ground surface due to the volumetric expansion of water as it freezes and the additional formation of segregation ice lenses. The volume of water expands by 9% as it freezes to ice, but the majority of the expansion observed in frost heaving is due to ice lens formation caused by cryosuction (Black, 1991).

Frost action can also develop patterns on the ground surface in the form of strips, circles, or polygons. Repeated freezing and thawing sort finer grained material to the centre of the patterned ground and coarser grained materials on the perimeter which is considered "sorted" patterned ground. "Unsorted" patterned ground usually takes a more hummocky appearance (Heginbottom et al., 2012).

On a larger scale, polygonal ground is created by a series of ice wedges in generally flat terrain. Thermal expansion and contraction regularly creates cracks in the ground over winter. The cracks tend to create hexagonal or quadrilateral shapes that can be between 5 and 15 m in diameter. The meltwater that fills the cracks in the spring eventually freezes in winter and further expands the cracks. The process continues and creates masses of more or less pure ice up to 5 m in length called ice wedges (Heginbottom et al., 2012).

Piprakes, or needle ice, are common in any region that experiences freeze-thaw cycles. They grow vertically downward from the ground surface, similar to ice wedges. Cryosuction draws water up to below the ground surface to develop elongated crystals of ice up to 40 cm in length (Davis, 2001).

Anomalous layers or bodies of unfrozen ground in a permafrost region are called taliks. Taliks form when freezing temperatures in winter do not reach the permafrost table, and are often found under water bodies such as lakes and rivers. The thawing of ice-rich permafrost or the melting of massive ice produces thermokarst landforms so called because of their similarities to karst topography in limestone areas. Melting ground ice creates or enlarges thermokarst lakes (thaw lakes) and depressions in the ground.

Pingos are among the most dramatic of periglacial landforms. They are conical or elongated perennial frost mounds that reach up to 50 m in height and consist of an icy core

covered with vegetation and soil (Heginbottom et al., 2012). When lakes in permafrost regions drain, the underlying talik begins to freeze. The growth of permafrost creates high pore water pressures in the core of the talik because of water expelled during freezing. The ground surface is thrust upward to relieve the high pore water pressures and subsequently creates a pingo (Heginbottom et al., 2012). The core consists of one or more layers of ice lenses that may be separated by frozen sediments. Pingos can be classified as either open-system (a consistent water supply like artesian water) or closed-system (a trapped limited supply of water).

Palsas are small frost mounds typical of discontinuous permafrost regions that generally develop in wetland environments. They consist of a peaty mound with alternating layers of segregated ice and peat and can reach up to 7 m in height (McGregor et al. 2010). The insulating peat layer shields the ice from thawing during the summer months.

Drunken trees are common in the presence of ground ice and frost action. Tree growth in permafrost regions is often stunted by the cold weather and the presence of ice. The tree trunks protrude in random directions due to frost heaving, palsa formation, or other processes.

2.6 Changes to Permafrost.

Permafrost regions are highly susceptible to long-term effects of warming temperatures. A negative net heat balance, with average ground temperatures below 0°C, maintains permafrost conditions. Human activities and changes in climate affect heat transfer into the ground and disturb the existing thermal regime. Consequently, the heat balance becomes positive, and contributes to short-term and long-term effects on permafrost.

Climate change is having global impact, and the effects are greater in some regions like the Arctic. General warming trends were observed throughout the 20th century and reports

indicated temperature increases as high as 5°C in Arctic regions (IPCC, 2001). In the last three decades, the average temperature of permafrost has increased 1- 2°C (IPCC, 2013). Climate models predict a 16.0 - 19.7% reduction in land surface area in Canada affected by permafrost by the end of the 21st century (Zhang et al., 2008). Figure 2.7 represents the historical freezing indices measured in Yellowknife, NT. In the past 70 years, winters have been getting progressively milder in Yellowknife, and projected trends predict winter will lose 0.5% of its freezing capacity each decade (Hayley and McGregor, 2007). Ground temperature projections in the northern hemisphere over the next 100 years are shown in Figure 2.8 (Heginbottom et al., 2012), and there is a noticeable increase in temperatures in permafrost regions.

As previously mentioned, human activity disrupts the natural equilibrium of heat transfer into the ground and affects the extent and thickness of permafrost and can lead to permafrost thawing (Brown, 1997). Construction activities often strip away the insulating vegetative layer to directly expose permafrost to sources of heat like solar radiation and warm air temperatures. The ground thermal regimes are also altered because the fill material from construction and the natural subgrade have different thermal properties. Snow cleared from highways insulates the ground along embankment side slopes and ditches and prevents heat loss that normally occurs during winter. At the same time, cold temperatures penetrate under the road more easily. Additionally, the thermal regime in permafrost regions can be altered by wildfires caused by humans or lightning strikes.

Permafrost is generally classified as either warm or cold. Cold permafrost has an average annual ground temperature well below freezing (less than -2°C) while warm permafrost has an average annual ground temperature just below freezing (greater than -2°C) (IPCC, 2013). More energy is required to increase the temperature of warm permafrost enough to induce thawing

compared to increasing the temperature of cold permafrost by the same amount. As a result, the ground temperature change is greater in cold permafrost regions than in warm permafrost regions even if both regions experience the same climatic changes (Burns, 2007). The difference is related to the heat capacity of the soil and the latent heat of fusion of water (mentioned in Section 2.4 The Behaviour of Frozen Soil). The latent heat of fusion of water is 333.9 Joules per gram (Lide, 1994). The heat capacities of liquid water and ice are 4.184 and 2.09 Joules per gram per degree Celsius, respectively. As an example, 342.3 Joules per gram are required to melt ice that experiences a 2°C temperature increase from -1°C to +1°C. Meanwhile, only 4.18 Joules per gram are required to increase the temperature of ice by 2°C from -10°C to -8°C. Cold and warm permafrost would behave similarly though the frozen and unfrozen heat capacities are different to reflect the soil constituents. Chapter 5 discusses the heat capacities selected for the soils used in the thermal numerical modelling using the empirical method provided by Andersland and Ladanyi (2004).

Thawing permafrost threatens the stability of infrastructure. Thawing of ground ice permafrost can lead to thickening of the active layer, ground subsidence, and development of uneven and occasionally unstable thermokarst terrain. Thaw consolidation during thawing of frozen ground occurs as the result of applied stresses and the self-weight of the frozen soil. Loads sustained for a long period of time may cause stability and serviceability issues such as slope failures, foundation failures, or differential settlements (Harris, 1988). Creep is the time-dependent deformation of soil. Thaw consolidation can generate excess pore water pressures when the melting rate exceeds the dissipation rate of pore water. Consequently, the bearing capacity of ground affected by permafrost is reduced as it warms, and can lead to failure of

foundations of buildings, roads, and pipelines. Low lying coastal areas are at risk because permafrost warming can leave the soil more vulnerable to erosion (AMAP, 2012)

Permafrost has been identified as a "geoindicator" for monitoring and assessing environmental change (Berger and Iams, 1996). Permafrost in Arctic regions often has a high organic content, and stores 44% of the global near-surface carbon (AMAP, 2012). Large quantities of methane hydrates are also stored in sub-sea permafrost. Greater amounts of methane and carbon dioxide will potentially be released into the atmosphere due to permafrost thawing, adding to the greenhouse gases already affecting climate change. Permafrost regions are very sensitive to change. Disturbances at the ground surface can scar the landscape irreparably, taking decades or longer to recover as was observed along the Qinghai-Tibet Highway (Jin el al., 2008). Thawing permafrost can cause land to dry out or become waterlogged. Consequently, the physical and chemical conditions of ecosystems are altered which affects the vegetation and organisms they support (AMAP, 2012).

2.7   Design, Construction, and Maintenance in Permafrost Regions

Significant impacts on infrastructure in permafrost regions are anticipated due to permafrost changes induced by human activity and climate change. Design, construction, and maintenance practices in permafrost regions must differ from those in non-permafrost regions to account for the unique ground conditions. All infrastructure projects must be implemented to address the related permafrost challenges in the most effective and economically efficient way during their expected lifespan. Infrastructure must provide the basic necessities of life, like housing and healthcare, and also promote responsible development of natural resources, like forests, oil, gas, and minerals, for the socio-economic benefits of the region. At the same time, infrastructure

must reduce its environmental impact. Several provinces and territories in Canada already have substantial existing infrastructure in permafrost regions. Infrastructure encompasses a wide variety of uses from foundations of buildings, to mining operations, to hydroelectric generating stations, and also linear infrastructure such as highways, railways, runways, and pipelines. Frost jacking, frost heaving, thaw consolidation, and the impact of future temperatures are among the challenges encountered in permafrost regions.

Strategies and technologies developed to address the requirements of variable permafrost conditions are based on technologically advanced methods as well as common sense. Permafrost can be successfully managed during construction if disturbance of the natural thermal regime is minimized. Several passive permafrost mitigation measures have proven effective on their own and in tandem with one another. This section provides an overview of some, but not all, currently available permafrost construction techniques and considerations.

2.7.1. Preliminary Work and Site Assessment

Preliminary work ahead of any infrastructure project involves initial assessment of needs and requirements, and the methods that should be undertaken to minimize the impact on permafrost. Aerial photography can identify many periglacial landforms. Aerial photography is a useful observational tool to assess the extent of permafrost at a site, especially useful for route evaluations of linear infrastructure like highways, railways, and airport runways. A site visit must be done to confirm the aerial photography assessment using a combination of drilling, sampling, in-situ testing, laboratory testing, and geophysical methods. Geophysical methods like ground penetrating radar can identify possible permafrost zones (depending on the soil types and other factors) without disturbing the thermal regime.

2.7.2. Construction Practices

The benefits and drawbacks of winter or summer construction must be considered in each project. Winter construction can be hindered by weather conditions, but frozen ground is stronger and less compressible than unfrozen ground which allows the placement of rock fill for embankments and the crossing of sensitive terrain. Construction days are longer in the summer and compaction of granular fills is more easily achieved (McGregor et al., 2010). Several factors must be considered in the selection of borrow material to minimize the disturbance of the local thermal regime such as the distance between the borrow pit and the site, the impact on the local soil profile during and after extraction, location of the staging area, and the thermal properties of the borrow material. Thaw consolidation is a consequence of placing the borrow material at a staging site or its final location. Pre-thawing can induce thaw consolidation prior to construction by stripping the vegetation to expose the permafrost. Gravel or darker material placed on the surface during the summer can accelerate thawing. Pre-thawing results are difficult to predict and the technique should only be considered for discontinuous permafrost regions (Beaulac and Doré, 2006). Reduction of the subgrade weight using light weight fill may reduce the amount of settlement, both vertically and laterally, and can be especially useful in regions of discontinuous permafrost. Typical materials include expanded polystyrene blocks, foamed concrete, rubber tire sheets, or even organics like peat or wood chips. The material can also be chosen to double as an insulating layer.

2.7.3. Drainage and Snow Accumulation Control

Construction can disturb existing ground thermal regimes because of alterations to drainage and natural snow accumulation patterns. Subsequent permafrost degradation can potentially cause damage to infrastructure. Poor drainage along highway embankments can increase the amount of

stagnant water in the ditches. The water can accelerate thawing of permafrost along embankment slopes especially at the toe. Well-designed cross and longitudinal drainage ensures water does not pond along embankments. However, culverts may lead to differential settlements on the road surface so the Transportation Association of Canada (McGregor et al., 2010) provides recommendations for drainage installation. Routine maintenance clears roads of snow which allows cold temperatures to penetrate further under the road surface. Cleared snow accumulates at the toe of the embankment. Snow is an insulator and retains the warm ground temperatures longer than if there was no snow cover. As a result, the snow cover could initiate permafrost degradation at the toe. Whenever possible, snow removal should be extended to include the shoulder and the side slopes.

2.7.4. Decreasing Heat Transfer to the Ground

Heat transfer into the ground can be reduced by increasing the thermal resistance between the subgrade and the infrastructure. A layer of polystyrene or polyurethane insulation embedded under the foundation of a building or the road bed reduces the penetration of heat from the structure (Regehr et al., 2012). In continuous permafrost regions, insulating layers often replace gravel fill. However, insulation limits heat extraction during the winter and may not be ideal for discontinuous permafrost regions (McGregor et al., 2010). High albedo road surfaces use different coloured road surfaces to reduce solar radiation absorption along highways. Awnings serve a double purpose as a sun shed to reduce exposure of the side slopes to direct solar radiation, and as a snow shed to reduce the amount of snow accumulation (McGregor et al, 2010).

2.7.5. Heat Extraction from the Ground

Heat extraction techniques improve thermal stability by reducing the temperatures of the subgrade. Methods developed to cool the subgrade include air convection embankments, ventilation ducts, heat drains, and thermosyphons. Thermosyphons are among the most effective and expensive methods. The Alaska oil pipeline used thermospyhons in the foundation supports (thermopiles), as shown in Figure 2.9, extensively throughout its 800-mile (12,800 km) length. Thermosyphons are tubes placed in the ground partially filled with liquids such as ammonia or carbon dioxide. The top and bottom of the thermosyphon are called the condenser and evaporator, respectively. When the ground temperature is warmer than the air, heat from the ground causes the liquid to vaporize in the evaporator. The gas rises to the condenser above ground, and exposure to the cooler air temperatures causes the gas to condense to a liquid and release the heat. Air convection embankments (ACE) partially or completely consist of coarsely-graded rock fill as shown in Figure 2.10. ACEs allow cold air to sink into the embankment during the winter and often use organic covers to reduce heat penetration during the summer (Remchein et al., 2009). Ventilation ducts extract heat by natural air convection through pipes installed horizontally in the ground to accelerate the penetration of cold air into ACEs. The ducts are only effective in the winter and should be closed in the summer so warm temperatures do not infiltrate the embankment (McGregor et al., 2010). Heat drains consist of a pipe and a geocomposite installed parallel to the road surface with regularly placed vertical standpipes providing an outlet for warm air and intake for cold air.

2.8. Highway Embankments Research Sites in Permafrost

This section provides brief overviews of research that has been conducted at other project sites on highways in permafrost regions in Canada and the world. Included are the Qinghai-Tibet Plateau in China, Thompson Drive in Fairbanks, Alaska, the Alaska Highway near Beaver Creek, Yukon, and Provincial Road (PR) 290 near Gillam, Manitoba.

2.8.1. Qinghai-Tibet Plateau, China

The Qinghai-Tibet Engineering Corridor (QTEC) in China connects Golmud, Qinghai to Lhasa, Tibet though the alpine permafrost regions of the Qinghai-Tibetan plateau. The corridor is greater than 4000 m elevation for close to 80% of the 1120 km length. The elevation even exceeds 5000 m for 50 km. Several notable linear infrastructure projects have been constructed in the corridor including the Qinghai-Tibet Highway (QTH) in 1954, pipelines from 1972 to 1977, fibre optic cables in 1997, the Qinghai-Tibet Railway (QTR) from 2001 to 2006, and transmission lines from 2005 to 2006 (Jin et al., 2008). Permafrost degradation and thawing was an important consideration for each project. The QTH has experienced severe deformations because the original construction in the 1950s initiated permafrost thawing which accelerated after an upgrade to an asphalt surface in the 1970s (Jin et al.). Ground temperature monitoring conducted in the 1980s precipitated major rehabilitation of the QTH in the 1990s. Rehabilitation included the installation of insulation, ventilation ducts, and thermosyphons (Fortier et al., 2012). Greater thermal stability was achieved in sections that had protective measures such as thermosyphons (Wu et al., 2014) and ventilation ducts (Sun et al., 2011).

2.8.2. Thompson Drive in Fairbanks, Alaska

The Alaska Department of Transportation constructed Thompson Drive from 2003 and 2005 to provide direct access to the University of Alaska Fairbanks campus. The 800 m long stretch of road connected Tanana Drive and Geist Road over two sections of previously undisturbed permafrost. Thaw settlement was a serious concern for construction and maintenance, especially for the 10 m high embankment required for the bridge over the Alaska Railway. The design implemented ventilation ducts, air convection embankments (shown in Figure 2.10), and thermosyphons to cool the subgrade and maintain the thermal regime (Goering, 2004). The Thompson Drive project was notable for developing hairpin thermosyphons that kept both the evaporator and condenser under the road surface to reduce the roadside danger and improve aesthetics. Test sections were instrumented with thermistors to monitor the success of the cooling strategies. The hairpin thermosyphons effectively removed heat from the centre of the embankment during the winter months (Xu and Goering, 2008). The air convection embankments reduced subgrade temperatures over the winter while the ventilation ducts performed better at the base of the embankment slope than the mid slope (Xu and Goering, 2008).

2.8.3. Alaska Highway near Beaver Creek, Yukon

The Alaska Highway provides a vital transportation link between Alaska and the rest of the mainland United States via north-western Canada. Construction in 1942 was completed in only eight and one-half months to enhance security in the United States during World War II. The highway encompasses sporadic to continuous permafrost regions as well as warm and cold permafrost. The warm and ice-rich discontinuous zones are especially vulnerable to degradation due to disturbances of the thermal regime. Changes in climate and highway reconstruction have

induced permafrost degradation and subsequently led to severe settlements and longitudinal cracking. In 2008, Yukon Highways and Public Works undertook an ambitious highway research project to determine cost-effective mitigation techniques to reduce permafrost degradation under the highway embankments. In April 2008, twelve (12) experimental test sections were constructed along a 600 m stretch of highway located 8 km south of Beaver Creek, Yukon. The mitigation techniques implemented included air convection embankments (ACE), light coloured bituminous surface treatments, heat drains, longitudinal culverts, side slope snow clearing, and snow sheds (Remchein et al., 2009). The test sections were monitored with thermistors, surface temperature loggers, and weather monitoring equipment. Each of the mitigation strategies demonstrated various levels of success in early assessments of the test sections. Longitudinal culverts reduced the thickness of the active layer and air convection embankments decreased permafrost temperatures (Lepage et al., 2012). Heat drains were not effective, but the intake/outlets may have been damaged during construction (Lepage et al., 2012).

2.8.4. PR 290 near Gillam, Manitoba

The construction embankments in Northern Manitoba use similar practices to those used in warmer regions of the province and often induces permafrost degradation. Manitoba Infrastructure and Transportation (MIT) installed 26 thermistors along a section of Provincial Road (PR) 290 northeast of Gillam to monitor the ground thermal regime. The project site was located in a region close to the transition from discontinuous permafrost to continuous permafrost. The thermistors were installed to a depth of 9 m at the centreline of the road, and at the toe on both the north and south embankment slopes. Ciro (2006) developed thermal and deformation numerical models with 2004 Geo-Slope software based on the three years of ground temperature data collected by MIT between 1996 and 1998. No in-situ or laboratory tests were

performed and all material properties were taken from typical values stated in literature. The TEMP/W thermal model indicated that permafrost degradation begins at the toe and spread laterally. Ciro (2006) proposed the peat layer under the embankment may preserve the permafrost. The SIGMA/W deformation model simulated vertical and lateral displacements. Ciro (2006) noted that the Geo-Studio software lacked the ability to couple the thermal and deformation analyses. Deformation of the embankment can occur without a new load being applied because the strength and compressibility of the ground changes as it freezes and thaws. A hypothetical load needed to be applied in the model because the simulated changes in the extent of the frozen ground from the thermal model could not be directly integrated into the deformation model. Ciro (2006) divided each year of the deformation model into freezing and thawing stages. The size and shape of the frozen ground was approximated at each stage. The embankment was unloaded during the freezing stages and re-loaded in the thawing stages. The simulated vertical and horizontal data suggested displacements will go inwards towards the centreline of the embankment. No displacement data was available for comparison.

2.9. Justification for this Research Project

Permafrost affects infrastructure built in cold regions across the globe. Permafrost is highly sensitive to changes in its thermal regime due to climate warming and human activity. The social and economic development of Northern Canada is inherently linked with the quality of transportation infrastructure that connects the region to the rest of Canada through various zones of permafrost. Many studies have monitored ground thermal regimes or evaluated the effectiveness of mitigation strategies intended to reduce permafrost degradation. The project sites are generally in regions where the permafrost is either extensive discontinuous or continuous.

Less attention has been given to sites with degrading permafrost on the fringe of discontinuous permafrost.

The original research at PR 391 project site consisted of a site investigation, field instrumentation, data collection, laboratory testing, and numerical modelling (Batenipour, 2012). Ground temperature data were only collected at the mid slope and toe of the embankment which limited the effectiveness of the numerical model to simulate the behaviour of the ground thermal regime under the centre of the embankment. A deformation numerical model had also been developed for an embankment in Northern Manitoba, but it was located along PR 290 near Gillam in a region with more extensive permafrost than the PR 391 site (Ciro, 2006). The model only used literature recommended values for soil properties and had no displacement data for comparison.

The goal of the author's research project was to maintain the momentum of the previous research performed at the PR 391 project site by Drs. Batenipour and Kurz. Ground temperature data were now collected at the toe, mid slope, shoulder, and centreline of the embankment. The expanded ground temperature monitoring allowed the author to develop thermal numerical models to simulate the current behaviour of the embankment and make long term projections with greater accuracy than the previous research. The author developed a deformation numerical model for the PR 391 project site to examine the deformation behaviour of a highway embankment in degrading permafrost on the southern edges of the region of discontinuous permafrost. Laboratory tests also provided more site specific mechanical material properties. The author collected embankment displacements both vertically between the toe and centreline as well as laterally at the shoulder. This made it possible compare simulated deformations to actual measured displacements.
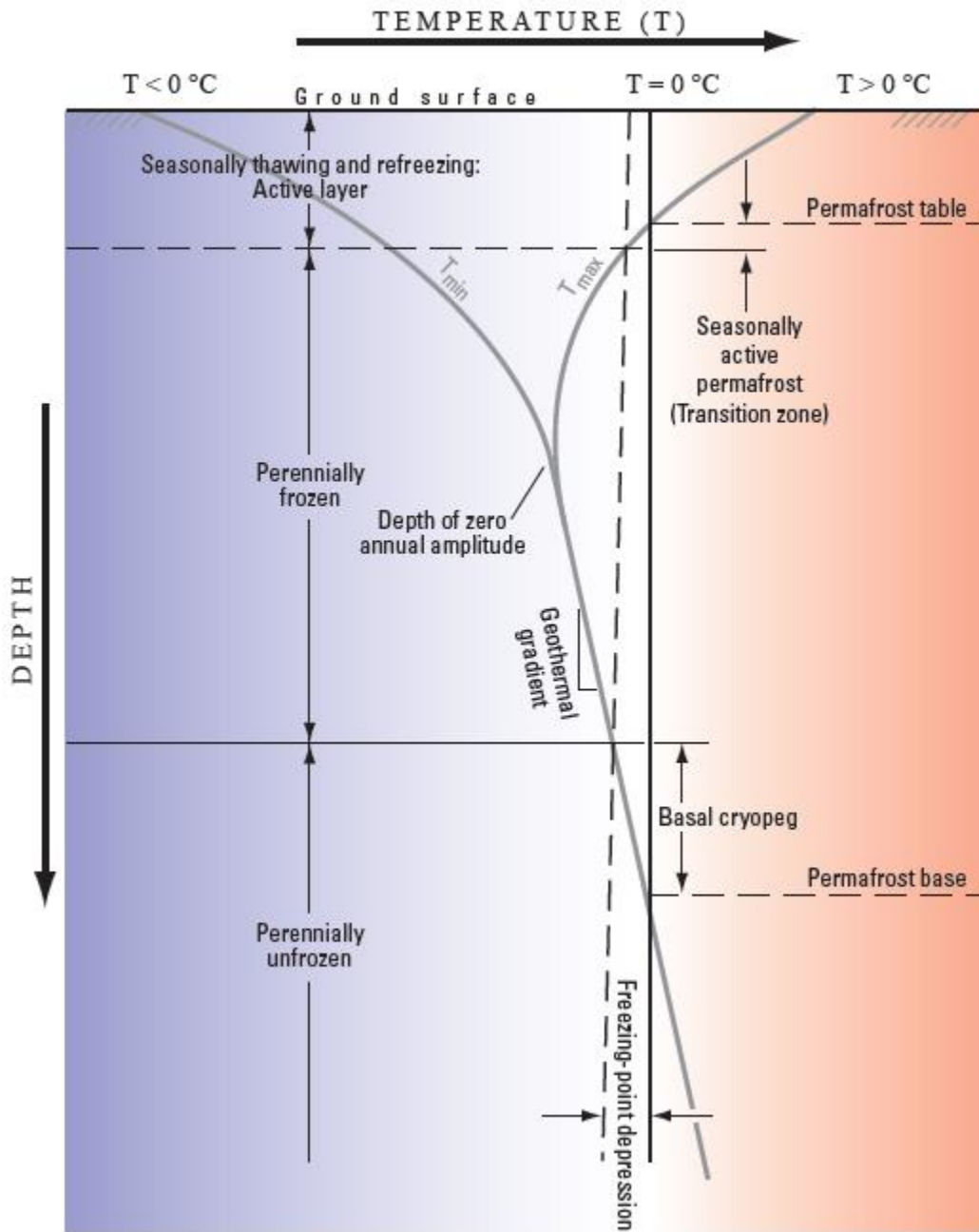
Figure 2.1: Temperature Envelope in a Permafrost Environment (Heginbottom et al., 2012) (Used with permission)
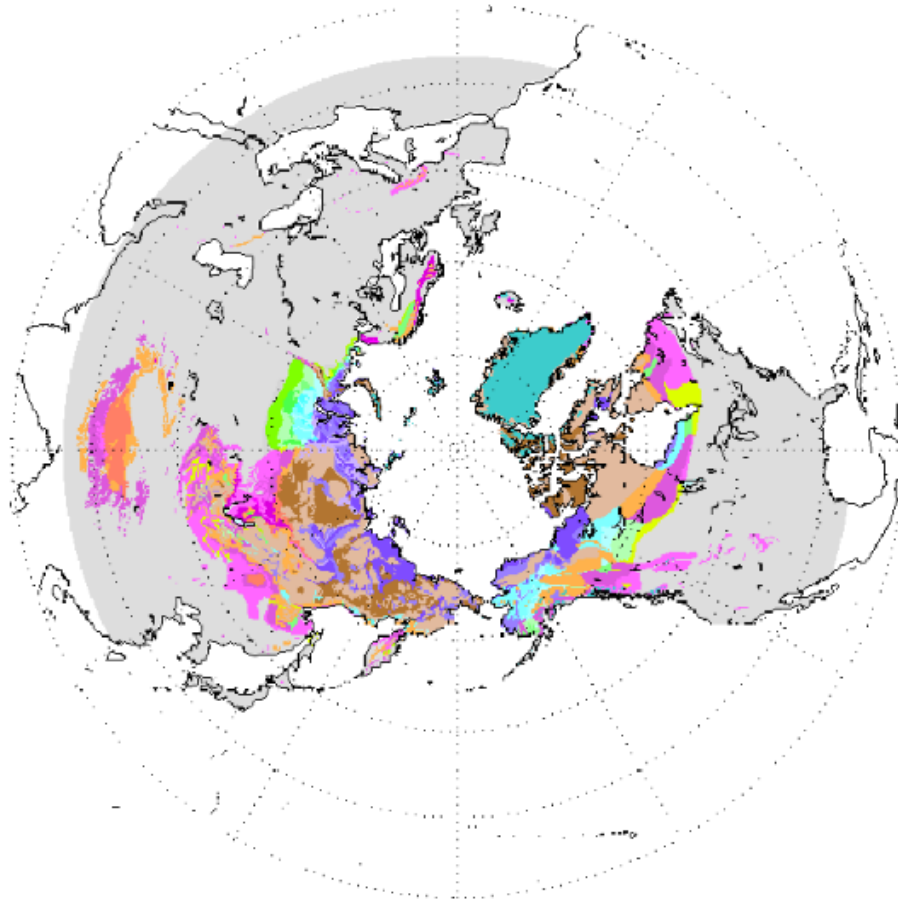
Legend for EASE-Grid Permafrost and Ground Ice Map

Permafrost Extent (percent of area)	Ground Ice Content (visible ice in the upper 10-20 m of the ground; percent by volume				
	Lowlands, highlands, and intra-and intermontane depressions characterized by thick overburden cover (>5-10m)			Mountains, highlands, ridges, and plateaus characterized by thin overburden cover (<5-10 m) and exposed bedrock)	
	High (> 20%)	Medium (10-20%)	Low (0-10%)	High to medium (>10%)	Low (0-10%)
Continuous (90-100%)	Ch	Cm	Cl	Ch	Cl
Discontinuous (50-90%)	Dh	Dm	Dl	Dh	Dl
Sporadic (10-50%)	Sh	Sm	Sl	Sh	Sl
Isolated Patches (0-10%)	Ih	Im	Il	Ih	Il

Variations in the extent of permafrost are shown by the different colors; variations in the amount of ground ice are shown by the different intensities of color. Letter codes assist in determining to which basic permafrost and ground ice class any particular unit belongs. Letter codes are defined in the documentation that accompanies the data files.

Ice caps and glaciers

Figure 2.2: Circum-Arctic Map of Permafrost and Ground Ice Conditions (Brown et al., 2001) (Used with permission)
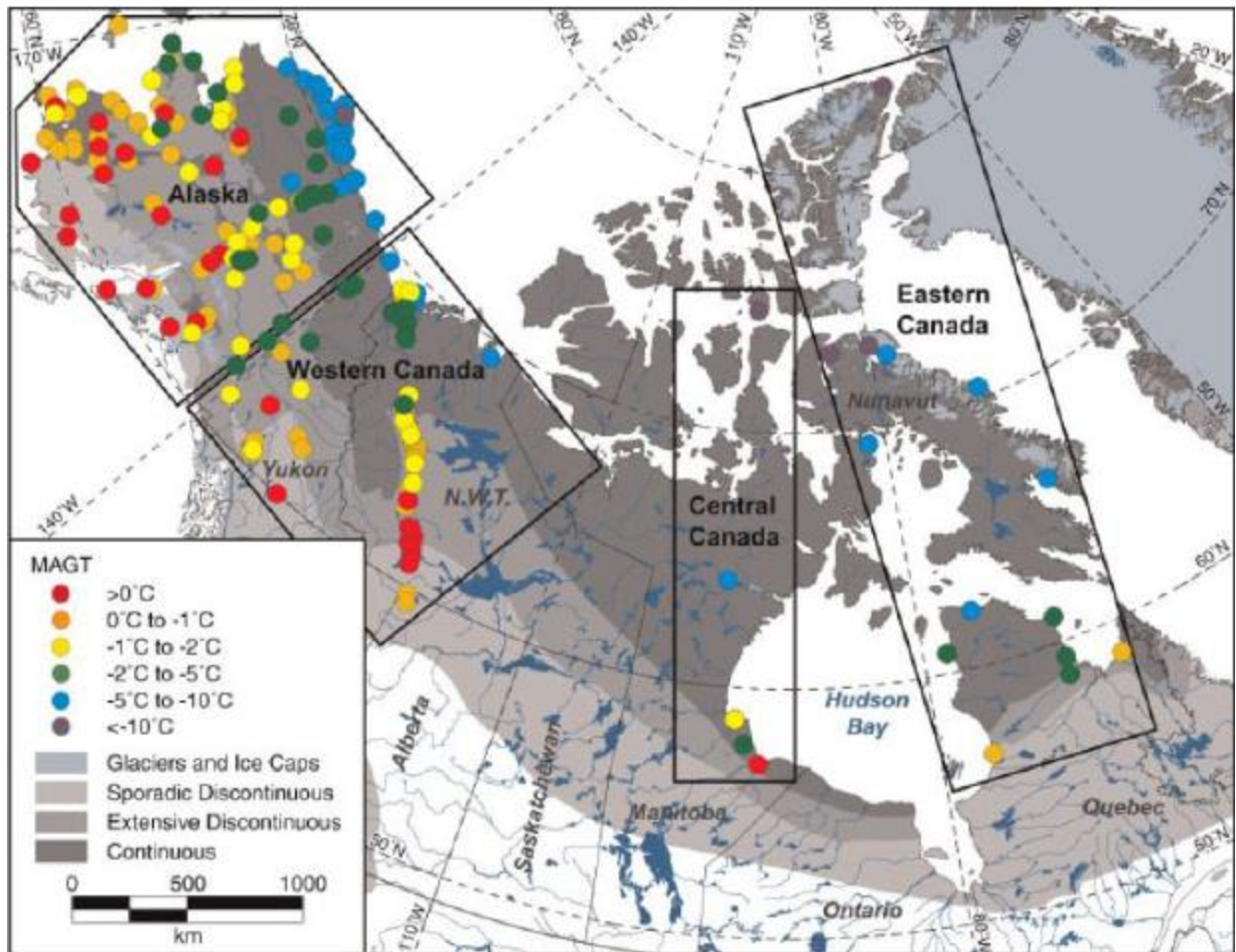
Figure 2.3: Permafrost Monitoring Stations in Canada (Smith et al., 2010) (Used with permission)

NORTH   SOUTH

Resolute NWT   Norman Wells   Hay River

0.5m   Active Layer   1.5 - 3m

400m   Permafrost   45m   12m

Unfrozen Ground

Continuous Permafrost Zone ──►◄── Discontinuous Permafrost Zone
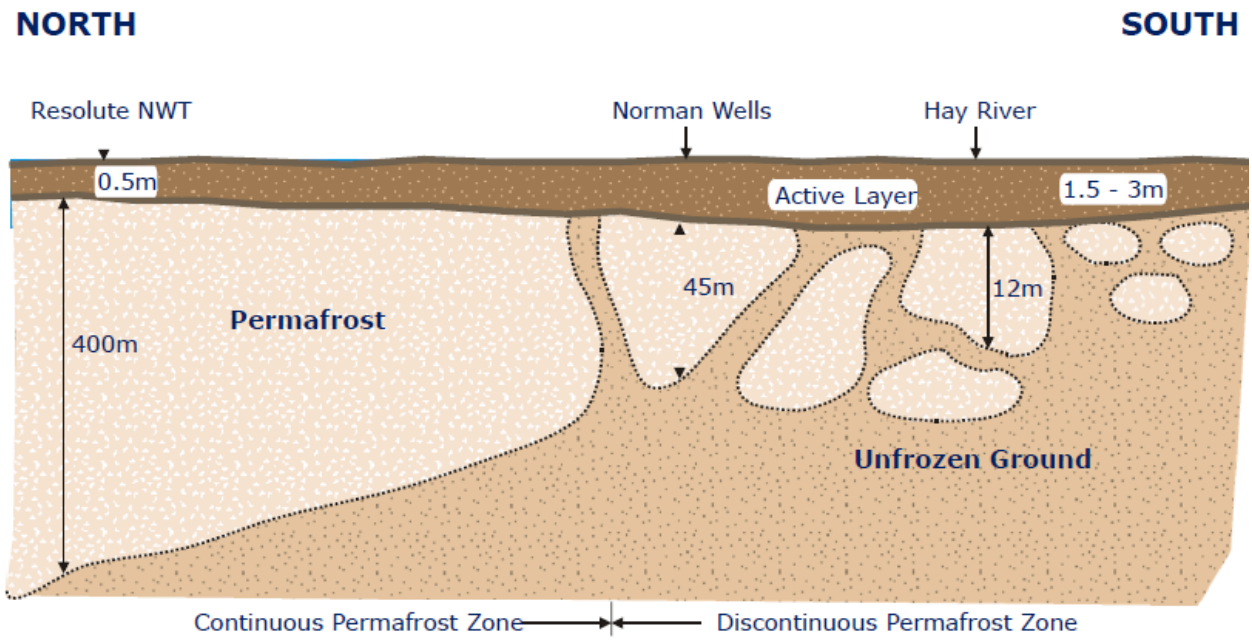
Figure 2.4: Variations of permafrost thickness in Canada (Brown et al., 1981) (Used with permission)
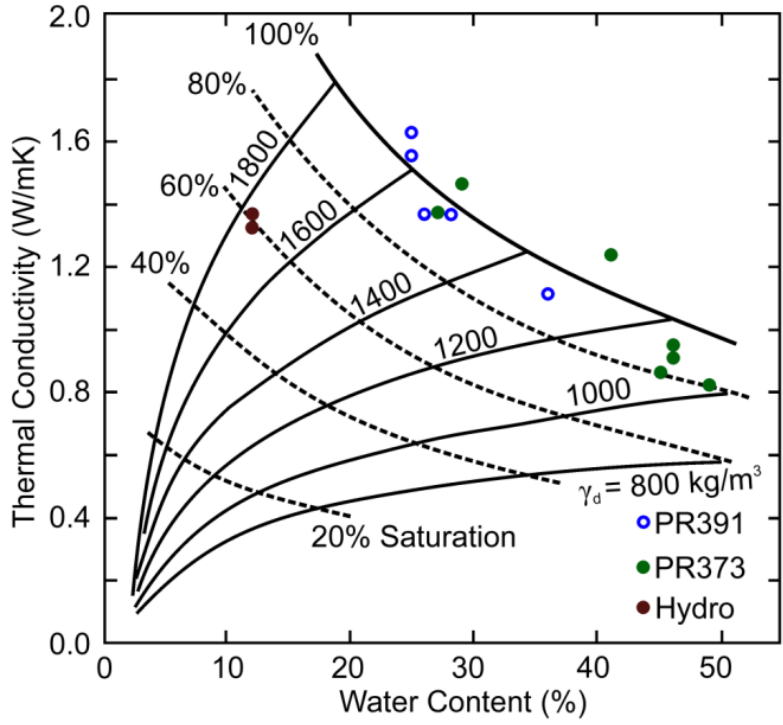
Figure 2.5: Unfrozen Silty and Clay Thermal Conductivity (Kurz et al., 2012a) (Used with permission)
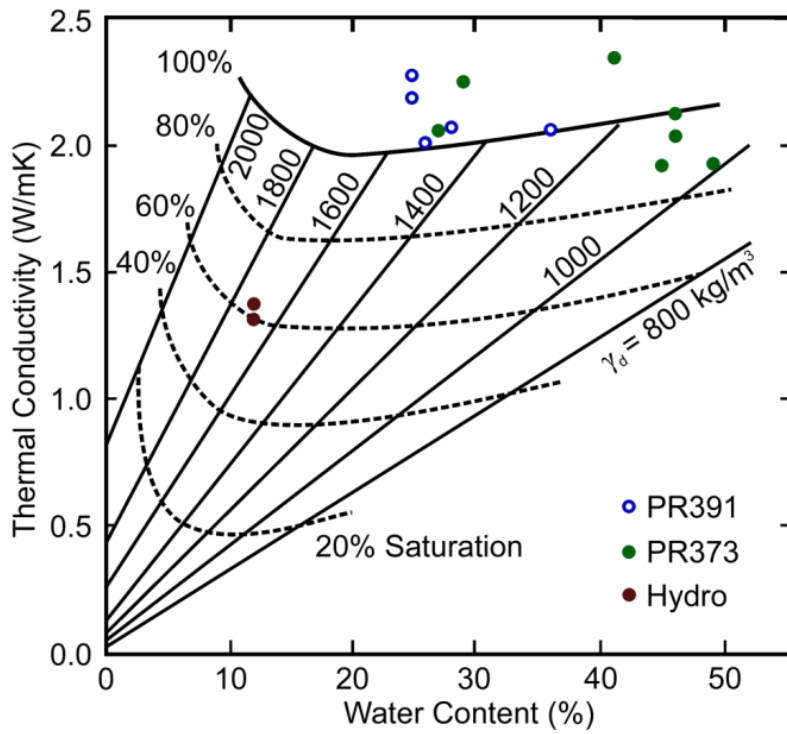
Figure 2.6: Frozen Silty and Clay Thermal Conductivity (Kurz et al., 2012a) (Used with permission)
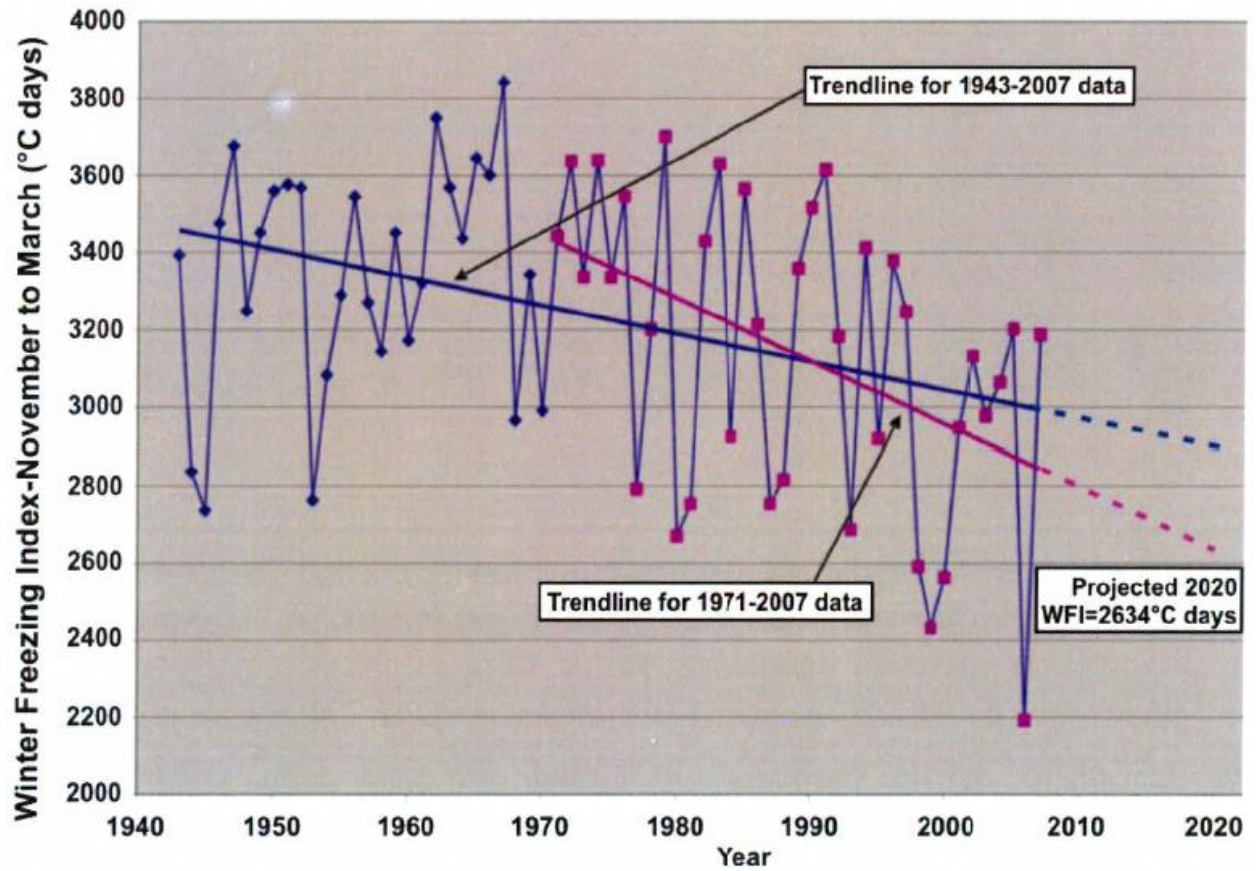
Figure 2.7: Climatic Variability near Yellowknife, NWT (Hayley & McGregor, 2007) (Used with permission)
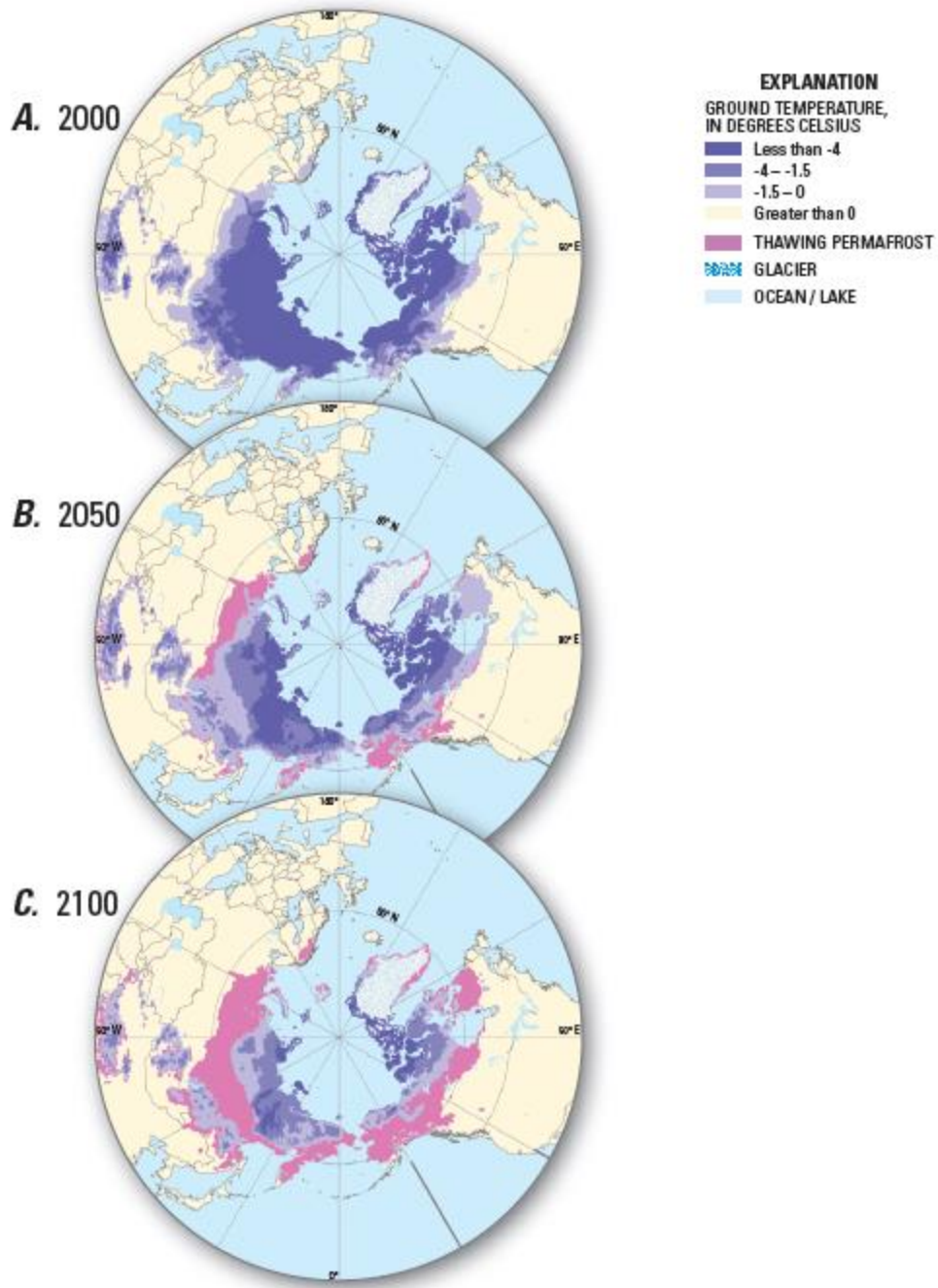
Figure 2.8: Modelled circumpolar permafrost temperatures (mean annual temperature at the permafrost surface) for A, 2000; B, 2050; and C, 2100 (Heginbottom et al., 2012) (Used with permission)

Figure 2.9: Thermopiles used as a passive heat extraction device for the Alaska pipeline near the Yukon River

Figure 2.10: Air Convection Embankment used on the approach for the bridge over the Alaska Railroad on Thompson Drive in Fairbanks, Alaska.

Chapter 3:   Site Characterization and Laboratory Testing

The following chapter discusses the development of Provincial Road (PR) 391, and the characterization of the project site and its surrounding area. The laboratory testing program conducted on samples taken from the shoulder of the embankment at the site in 2012 is presented and compared to the results obtained in 2008 from Batenipour (2012).

3.1   Background

Permafrost is prevalent throughout northern Manitoba and covers more than half of the land area as shown in Figure 3.1. Isolated patches of permafrost first appear near the northern tip of Lake Winnipeg. The permafrost transitions further north from sporadic discontinuous to extensive discontinuous permafrost. The permafrost becomes continuous closer to Hudson Bay.

Almost all infrastructure built in this part of the province interacts with permafrost conditions. A well-known example is the Hudson Bay Railway (HBR) between The Pas and Churchill, Manitoba (OMNITrax, 2012). Completed in 1929, the HBR is a vital link to several communities and is used to export Canadian resources such as wheat. However, considerable maintenance costs hinder the operating capacity of the track as it must traverse over 1000 km of variable permafrost conditions. This has led to issues such as large settlements (shown in Figure 3.2) and derailments. Other transportation infrastructure facing similar difficulties in northern Manitoba includes airport runways and highways.

The project site is located 18 km outside of Thompson, Manitoba on PR 391 as shown in Figure 3.3 with approximate coordinates 55°50'44" north latitude and 98°01'13" west longitude. PR 391 is an all-weather road that provides the only land transportation link between southern

Manitoba and the towns, First Nations communities, mines, and hydroelectric generating stations in northwestern Manitoba. It also provides the only land connection to Kinoosao, Saskatchewan.

Development of transportation infrastructure in northwestern Manitoba began after the discovery of mineral deposits in the 1950s. Several First Nations communities, such as Nelson House and South Indian Lake, preceded the discovery of these deposits. Lynn Lake was founded in 1950 and Thompson soon followed in 1956 (Lynn Lake, 2014). Further development included two Laurie River generating stations to power the mine operations (Manitoba Hydro, 2014). Further development in northwestern Manitoba necessitated the construction of an all-weather road. PR 391 was first constructed in the mid-1960s as a compacted earth road in a region classified as discontinuous permafrost. The highway was upgraded to gravel in the 1970s and then to a bituminous asphalt surface in the 1980s. Problems arose when discontinuous permafrost detected along sections of the highway during the initial construction showed signs of degradation, especially under the embankments. The changes in the underlying thermal regimes led to thawing and caused potentially hazardous driving conditions such as differential settlements and lateral spreading. Manitoba Infrastructure and Transportation (MIT) attempted to reduce the consequences of degrading permafrost with the construction of stabilizing berms and insulating peat berms adjacent to the embankments in the 1990s. The berms provided minimal improvement and they eventually settled into the foundation soil below grade (Batenipour, 2012). MIT allowed problem sections, such as the project site shown in Figure 3.4, to revert back to a gravel surface because it was easier to maintain than an asphalt surface. Current maintenance mainly consists of adding gravel fill and grading the road. Many sections now have several metres of gravel fill. Exact maintenance records specifying the quantities of gravel and location of its application were not available.

3.2   PR 391 Site Description

Boreholes drilled at the toe of the embankment in 1991 revealed frozen soil at depths from 1.9 m to 10.5 m. Boreholes drilled in 2005 encountered frozen soil at the toe between depths 4.6 m and 10.7 m. However, drilling at the toe and mid slope in 2008 no longer encountered frozen soil beneath the active layer. In September 2012, drilling was performed at the shoulder and centreline for the first time to install additional instrumentation as part of the author's research. During this drilling, frozen and ice-rich soil was found at the shoulder between depths 6 m and 9 m (Figure 3.5) and at depths between 4.5 m and 11 m under the centreline.

The site is in a depression between two higher points of ground and is poorly drained with standing water year-round within 20 m of the toe of the embankment. Drilling indicated approximately 6 m of gravel fill at the centreline. The embankment is much thicker than the original construction due to the ongoing maintenance that compensates for settlements. The soil at the site consists of a 1 m thick upper layer of clayey peat-silt from the stabilizing berm that is underlain by highly plastic clay. The clay is brown, silty, and firm in the upper layers and becomes grey and very soft closer to the gneissic bedrock found at a depth of 18 m. An approximate cross section of the project site is shown in Figure 3.6. A borehole log from drilling at the shoulder is included in the Appendix.

3.2.1. Geophysics Investigation

Geophysical surveys are an indirect, non-intrusive method for detecting, monitoring, and interpreting sub-surface conditions. Geophysical surveys can be used to establish some properties of permafrost and its distribution horizontally (mapping) or vertically (sounding). Four main geophysical techniques are used for permafrost terrain applications: electrical resistivity, electromagnetic, seismic, and ground penetrating radar methods (Hauck, 2013). Each method has

positive and negative attributes related to surveying permafrost. A geophysical survey was conducted at the project site using two techniques: electrical resistivity and ground penetrating radar. This was the first geophysical investigation conducted at the PR 391 project site.

Ground penetrating radar (GPR) uses the penetration and reflection of high-frequency radio waves (UHF/VHF frequencies) to define shallow zones of rock and soil. It has been effective for determining the location of permafrost (McGregor et al., 2010). GPR consists of a radar control unit, a transmitter antenna, a receiver antenna, data storage, and a graphic display. Short radio wave pulses are continuously transmitted into the earth. Some of the energy is reflected back to the unit. The amount of energy reflected back to the unit is related to the difference in dielectric constants of the materials encountered and penetrated. Abrupt changes in the amount of energy reflected are related to abrupt changes in materials and can define the subsurface layers. GPR can be most effective in differentiating soil and rock units or the presence of other objects like water tables, buried tanks and pipes, or permafrost. The time it takes the energy to return can be related to the depth. The depth at which GPR is effective depends on the electrical conductivity of the material. For granular materials or rock, GPR can be effective to a depth of 15 m. Detection can reach much greater depths depending on the frequency, but the resolution decreases. GPR is less effective for less electrically conductive fine grained materials like clay and can be limited to 5 m or less.

Electrical resistivity (ER) determines variations in materials in both vertical and horizontal directions below the ground surface. The resistivity of soil and rock depends on its composition. ER surveys induce a current in the ground between electrodes at the surface set at a known distance apart. The change in electrical potential between the electrodes determines the resistivity of the soil or rock. Capacitively coupled resistivity systems such as the OhmMapper

are less susceptible to the limitations experienced by electrode based systems at boundaries of frozen ground due to high contact resistance. An OhmMapper system consists of a transmitter, as many as five receiver nodes, and a data logger. The transmitter induces a current through the ground. A second circuit completed between the ground and the receiver nodes measures the resistivity of the ground. Multiple passes are made across the same survey line while the distance between the receiver nodes are varied. The depth of detection depends on the distance between the receiver nodes.

Golder Associates in Winnipeg conducted the geophysical survey at the project site on September 24 and 25, 2012. Results are provided in the Appendix. The GPR and OhmMapper surveys both used the same 45 m survey line that ran perpendicular to the highway embankment. The survey began on the south side of the embankment and finished on the instrumented north side. The GPR used two different bi-static antennas with intervals of 0.25 m and 0.50 m. The results of the 50 MHz and 100 MHz surveys are shown in Figure 3.7 and Figure 3.8, respectively. The results of this particular GPR have poor resolution and are not useful. An anomaly detected 1.5 m beneath the surface on the north shoulder of the embankment is likely due to the trench that was dug to bury the instrumentation cables. Quality equipment and experienced operators of the equipment are required to properly interpret the results and obtain detailed and accurate profiles.

The OhmMapper took voltage readings at 1 m intervals and had receiver nodes spaced 5 m and 10 m apart. The results are shown in Figure 3.9. There is a large area of elevated resistivity that begins under the centre of the embankment approximately 4 m below the ground surface. Higher values of resistivity are associated with materials with lower water content such as rock, clean gravel, and sand, while materials like silt and clay have lower resistivity values.

Despite the association with lower water contents, this area below the centreline corresponds with the same depth that frozen soil was encountered during drilling at the centreline. The resistivity is also a stark contrast with the surrounding soil in the embankment which is known to be gravel fill. The OhmMapper provided a reasonable estimate of the position of the frozen/unfrozen boundary.

3.3. Laboratory Testing

A series of laboratory tests was carried out to understand the properties of the soil under the embankment. Large four-inch (101.6 mm) diameter Shelby tube soil samples were taken at the shoulder in 2012 for laboratory tests that included water content, Atterberg limits, hydrometer analysis, one-dimensional consolidation tests, and consolidated undrained triaxial tests. Information about the samples and the test program is shown in Table 3.1. The same laboratory tests were conducted during the initial research phase in 2008 (Batenipour, 2012). At that time, more conventionally sized two-inch (50.8 mm) diameter Shelby tubes were obtained from the toe of the embankment. The laboratory tests performed for this research supplement the previous test results. A comparison between the results from two different sample tube diameters used for the triaxial tests is shown in Section 3.3.4 Triaxial Tests.

3.3.1. Soil Samples

Six (6) four-inch (101.6 mm) diameter Shelby tube samples were acquired in September 2012. Two samples were taken from above, three inside of, and one underneath the frozen ground region. Frozen ground made it difficult to obtain intact samples. Four Shelby tubes were damaged when they were pushed into the frozen ground. An example of a damaged Shelby tube is shown in Figure 3.10. As a result, only 6 to 8 inches (150 to 200 mm) of intact sample were

41

acquired out of the maximum 24 inches (610 mm) in the damaged Shelby tubes. The Shelby tubes were sealed with wax to retain their moisture contents during transport to the University of Manitoba. Ideally, tests would be performed at in-situ conditions including temperature. However, it was not possible to keep the samples frozen during the transport back to Winnipeg and tests were performed on thawed samples.

3.3.2. Water Content, Atterberg Limits, and Hydrometer Analysis

Index property tests, including natural gravimetric water content, Atterberg limits, and hydrometer analysis, were conducted to classify the soil at the site. These tests are useful for classifying fine-grained soils and identifying groups or soils with similar properties. They show the natural variability at a site, although they are not immediately useful for design or analysis purposes.

The natural gravimetric water content, w, is also called the water content and describes the amount of water in a soil. The water content is the ratio of the weight of water to the weight of dry soil in a specimen. The test procedure to determine moisture content followed ASTM D2216 – 10. The test involves weighing a specimen before and after placing it in a minimum 105°C oven for at least 24 hours.

Atterberg limits follow the test procedures outlined in ASTM D4318 – 10 to determine the liquid limit, plastic limit, and plasticity index of a soil. These limits represent the water contents that separate the solid, semisolid, plastic, and liquid states of fine grained soils. The liquid limit, w_L, is the water content at which a soil changes from a plastic to a liquid state, while the plastic limit, w_P, is the water content at which a soil changes from a semisolid to a plastic state (Budhu, 2007). Soils become weaker as their water content increases. While a soil on the dry side of the plastic limit behaves like a stiff and brittle solid, a soil on the wet side of the

liquid limit typically behaves essentially like a liquid and has lower shear strength. Soils exhibit plastic behaviour when their water content is between the liquid limit and plastic limit. This range is called the plasticity index, I_P, and is calculated using Equation 3.1.

[Eq. 3.1] $I_P = w_L - w_P$

The liquidity index, I_L, can be determined from the results of the water content and Atterberg limit tests as shown in Equation 3.2. It can be qualitatively correlated to shear strength estimates.

[Eq. 3.2] $I_L = \frac{w - w_P}{I_P}$

A hydrometer analysis determines the proportion of clay and silt particles in a specimen that have passed through the number 200 sieve. The tests follow the procedures outlined in ASTM D422 − 63. A small amount of dry fine-grained particles are placed in suspension in distilled water. A hydrometer measures how the suspension settles over time (Budhu, 2007). The length that the hydrometer stem protrudes above the suspension relates to the current density of the suspension and reflects the settlement of different sized particles using Stoke's Law. Larger and heavier particles settle faster than smaller particles.

Values of water contents, Atterberg limits, plasticity index, liquidity index, and the clay and silt fractions are shown in Table 3.2. Plots for the water content and Atterberg limits are shown in Figure 3.11a. Test results for the water contents are shown as specific points while the Atterberg limits are represented as range bars. Plots for the hydrometer analysis are shown in Figure 3.11b and show the clay fraction. The red data indicate samples from 2012 that the author tested, while the blue data indicate tests that had been performed with 2008 samples. A depth of 0 m refers to the elevation of the natural ground surface at the toe of the embankment.

Water contents increased with depth and sometimes exceeded the liquid limit. Liquidity indices generally increased from the surface to greater depths, and are significantly higher than 1.00 at 12 m depth. The water contents are lower closer to the surface and represent the exposure of soil to seasonal freezing-thawing or wetting-drying processes. Higher water contents and liquidity indices generally correlate to lower shear strength; the soil generally becomes softer and weaker at greater depths.

A greater proportion of silt was measured in the samples at the shoulder from 2012 at shallower depths compared with the samples from 2008 at the toe at similar depths. Silts usually have a lower liquid limit than clays (Budhu, 2007), and lower liquid limits were measured at the shoulder compared to the toe. The clay and silt fractions are about equal for samples at the shoulder, while the clay fraction at the toe in general is slightly larger than the silt fraction.

3.3.3. One-Dimensional Consolidation Tests

The one-dimensional consolidation test, also known as the oedometer test, examines the compression and consolidation behaviour of clay soil specimens. The test applies a series incremental loads, in both loading and unloading sequences, and measures compression to determine the compression index (C_c), the unload-reload index (C_r), and the preconsolidation pressure (σ'_{zc}). An extended period of loading can determine the secondary compression index, $C_{\alpha e}$. The test data can also be used, albeit less reliably, to calculate the hydraulic conductivity, k.

Four oedometer tests were conducted at room temperature on samples taken from beneath the shoulder at the project site in 2012. The procedures for the test followed the standard tests methods for one-dimensional consolidation properties of soils using incremental loading as outlined in ASTM D2435/D2435M − 11. Results were compared to results of oedometer tests from 2008 specimens that originated below the toe.

The apparatus in an oedometer test includes a cell assembly and consolidation test frame with a lever arm. The cell assembly consists of a cell that holds an oedometer ring, porous stones, filter paper, and a top cap. A stainless steel oedometer ring with a height of 64 mm and a diameter of 19 mm holds the clay soil specimen and prevents lateral spreading. Porous stones were saturated in distilled water, as recommended for samples taken from saturated field conditions, and placed on the top and bottom faces of the specimen to allow water to move freely vertically. Filter papers prevented the migration of soil from clogging the porous stones. The cell assembly was mounted to the test frame and the lever arm was lowered until contact was made with the top cap placed on the top porous stone. Loads applied to the lever arm during the test were transferred vertically to the soil specimen through the top cap. Movement of the soil specimen from the applied loads was measured by a dial gauge located on the lever arm.

The tests began when an initial seating load of 11 kPa was applied and the cell assembly was filled with distilled water. The small initial load prevented the specimen from swelling after the water was added. Loads were changed based on an incremental load ratio of 1.0 which meant for every increase or decrease, the load was doubled or halved, respectively. Each load was applied for 24 hours, sufficient time for excess pore water pressures to dissipate and for the thickness of the specimen to reach a constant value. The loading schedules for all tests were identical and are included in the Appendix.

Primary consolidation is the initial change in soil volume after an applied load has expelled water from the voids and transferred the load from excess pore water pressures to the soil structure (Budhu, 2007). Secondary compression, also known as creep, is a time-dependent response of the soil to the load when its internal structure rearranges over a long period of time after excess pore water pressures have dissipated. It is widely accepted that creep can occur

45

during primary consolidation in soft clays, but is a much slower and long-lasting process than

primary consolidation (Budhu, 2007). Recent work suggested that strains in creep can be divided

into an 'instant' elastic component and a non-recoverable plastic component (Yin et al., 2002).

Other work introduced viscoplastic behaviour to limit long term creep (Kelln et al., 2008), and

also incorporated temperature in an elastic-thermo-viscoplastic (ETVP) model (Kurz, 2013).

Primary consolidation can be characterized by the compressibility parameters C_c, and C_r.

The compressibility parameters for the author's oedometer specimens were determined during

loading and unloading sequences when the void ratio, e, was plotted against the log-scale of

normal stress, σ'_z, as shown in Figure 3.12. The void ratio is defined as the ratio between the

volume of void space, V_V, and the volume of solids, V_S, shown in Equation 3.3.

[Eq. 3.3] $$e = \frac{V_V}{V_S} = \frac{G_S \cdot \rho_w - \rho_d}{\rho_d}$$

Equation 3.3 requires the specific gravity (G_s - assumed to be 2.70), the density of water

($\rho_w - 1000$ kg/m^3), and the dry density of the soil (ρ_d). The dry density of the soil is the ratio of

dry mass of the soil to the total volume. It changes as the volume of the specimen changes during

the test. The heights of the specimens 24 hours after each load increment were used to calculate

the volume. All specimens were loaded to 640 kPa and then unloaded to 21 kPa.

The preconsolidation effective stress, σ'_{zc}, is commonly understood to be the greatest

vertical overburden effective stress that the soil has experienced in its history. Soil is classified as

over-consolidated if the preconsolidation effective stress exceeds the stress it is currently

experiencing. This is a simplistic definition as over-consolidated behaviour can be produced by

other processes such as aging, cementation, and changes in ground water potentials. The

preconsolidation effective stresses in the author's tests were determined using the method

proposed by Casagrande (Budhu, 2007). A soil is considered normally consolidated when the

current stress equals or exceeds the preconsolidation effective stress. Few clays in the field are found to be normally consolidated. In Figure 3.12, the normally consolidated phase is characterized by the Normal Consolidation Line, NCL. The compression index, C_c, is the slope of this line and can be calculated by Equation 3.4.

[Eq. 3.4] $C_c = \frac{e_1 - e_2}{log(\sigma'_{z2}/\sigma'_{z1})} = \frac{|\Delta e|}{log(\sigma'_{z2}/\sigma'_{z1})}$

Soil unloaded or reloaded below its greatest load is characterized by an unload-reload cycle, which usually indicates hysteresis. The Unload-Reload Line, URL, represents the average line through this cycle and is shown in Figure 3.12. The average slope of the URL is the unload-reload index. Sample calculations of the compression index and the unload-reload index are shown in Figure 3.12.

Creep is characterized by the secondary compression index, $C_{\alpha e}$, also known as the coefficient of secondary compression. Batenipour (2012) determined the secondary compression index when the specimen was loaded to its maximum stress for an extended period of time until the change in void ratio over log (time) reached a small constant rate. The author incrementally loaded specimens to a maximum stress of 1280 kPa for 16 to 17 days. Equation 3.5 determined the secondary compression index based on the slope of a void ratio versus log-scale of time plot during the extended loading period as shown in Figure 3.13 (Kelln et al., 2008).

[Eq. 3.5] $C_{\alpha e} = \frac{e_1 - e_2}{log(t_2/t_1)} = \frac{|\Delta e|}{log(t_2/t_1)}; \ t_2 \gg t_1$

Table 3.3 summarizes the soil properties obtained in all of the oedometer tests. Preconsolidation effective stresses are plotted in Figure 3.11c. The red data points represent specimens from the shoulder in 2012 while the blue data points represent tests on the specimens in 2008 from the toe. Specimens from 2012 between depths 7.6 m and 9.8 m are in the range of 52 to 73 kPa. The values decrease with depth which agrees with the results from the 2008 tests

except for the result from a depth of 12 m. It was speculated that weathering processes closer to the surface, such as freezing-thawing or wetting-drying cycles, were responsible for the increased preconsolidation effective stress closer to the surface (Batenipour, 2012).

Plots of void ratio versus log-scale of normal effective stress for the 2012 tests of specimens at the shoulder are shown in Figure 3.14 and Figure 3.15. The recompression indices for the 2012 specimens at the shoulder range between 0.012 and 0.068. The values agree with the range of 0.021 to 0.068 reported in tests of 2008 specimens at the toe (Batenipour, 2012). The compression indices are relatively consistent with a range of 0.104 to 0.175 for three of the specimens with the exception of a higher value of 0.378 for specimen T5 at depth 8.2 m; however, this is close to the highest value of 0.336 reported for 2008 specimens at the toe (Batenipour, 2012). Higher compression indices are associated with higher plasticity indices, higher water contents, and higher liquidity indices. The higher compression index in specimen T5 could be a reflection that the soil was previously frozen and has weakened due to thawing.

Plots of void ratio versus log-scale of time for the 2012 tests of specimens at the shoulder are shown in Figure 3.16 and Figure 3.17. The values of the secondary compression index range between 0.0038 and 0.0078. These are lower than the values reported for the 2008 specimens at the shoulder which were in the range of 0.007 to 0.016. The ratio between the secondary compression index and the compression index ($C_{\alpha e}/C_c$) can frequently be considered constant in the normally consolidated range of a given soil (Mesri and Godlewski, 1997). The values of this ratio in the author's tests range between 0.021 and 0.052 which is below the range of 0.04 to 0.08 that has been previously reported for the compression behaviour of clays (Mesri et al., 1995). Batenipour (2012) suggested that the low values of $C_{\alpha e}/C_c$ may be due to the relatively large silt-size component in the clay. The author noticed unusual behaviour during the creep portion of the

48

oedometer test. The secondary compression index governed the change in displacement until about day 10 when the displacement suddenly dropped at higher rate. This behaviour could not be satisfactorily explained at this time and warrants further study.

3.3.4. Triaxial Tests

Shear strength and pore pressure parameters were determined using triaxial tests. Triaxial tests determine soil behaviour and properties by first loading a cylindrical soil specimen with a cell pressure and compressing it at a constant axial rate. Triaxial tests are preferred because the drainage conditions or the pore water pressures can be controlled separately and the stress system is determinate. The test provides data to calculate total and effective stresses, axial load, axial strain, and pore water pressure. After data have been collected, the strength and deformation properties of the soil can be determined.

All triaxial tests are carried out in two stages: 1) consolidation and 2) shear. Triaxial tests can be classified as undrained or drained. In a consolidated undrained triaxial test, drainage is permitted during the consolidation stage but not during the shear stage. Test procedures followed the standard test methods for consolidated undrained triaxial compression tests (CIŪ tests) for cohesive soils described in ASTM D4767 – 11.

Four-inch (101.6 mm) diameter samples T3, T4, and T8 each contributed two specimens for a total of six consolidated undrained triaxial tests as shown in Table 3.1. The weight, diameter, length, and water contents of each specimen were recorded before and after the tests. The specimens had an average length and diameter of 203 mm and 97 mm, respectively. The results were compared to previous tests on the smaller two-inch (50.8 mm) diameter specimens taken from the toe in 2008.

Test specimens have a height to diameter ratio of 2. A minimum two-inch (50.8 mm) diameter is required, and a three-inch (76.2 mm) diameter is more commonly used. The edge effects related to damage during sampling and trimming are less pronounced for larger specimens such as the four-inch (101.6 mm) diameter specimens tested by the author. In triaxial tests, a specimen was first placed on the pedestal in the test frame. Porous stones and filter paper were put on the top and bottom faces of the specimen to allow saturation and to ensure that no soil was lost. Strips of filter paper were placed lengthwise on the specimen to provide drainage paths along the edge of the specimen. The strips sped up the equalization of pore water pressure in the specimen and the transducer that measured pore water pressure. The top cap was placed on the top porous stone and the whole specimen was enveloped in an impermeable latex membrane as shown in Figure 3.18. The latex rubber membrane was secured by three O-rings at the top and bottom. To ensure that the specimen is saturated, a back pressure, u_b, is applied internally as well as a cell pressure, σ_3, applied externally. The purpose of the back pressure is explained in the next paragraph. The triaxial cell is secured on the test frame and filled with water. The lines that supplied the back pressure were flushed to remove as much of the air as possible. Air in the lines can become trapped in the specimens and hinder saturation during the consolidation stage.

In the consolidation stage, a cell pressure ('confining pressure') is applied to the specimen to simulate in situ conditions. A back pressure is applied to saturate the soil. A B-Test determines the pore water pressure parameter, B, to evaluate the saturation of the soil. The consolidation stage is complete when the specimen is showing no volume change. The equation for the pore water pressure parameter, B, is shown in Equation 3.6 (Skempton, 1954):

[Eq. 3.6] $B = \dfrac{\Delta u_b}{\Delta \sigma_3}$

A fully saturated specimen at normal working stresses will produce a change in pore water pressure inside the specimen equal an applied change in cell pressure when no drainage is allowed; that is, B equals or is very close to 1.0. A triaxial test may proceed to the shear stage once B is acceptable. B is usually required to be greater than or equal to 0.95 and 0.98 for industry and research, respectively. If the B-test does not produce a value close to 1.0, then the pore water pressures (and therefore effective stresses) will not be measured accurately during the second stage of the test when shear stresses are developed.

In the second stage, an axial load and the resulting deviatoric stress are applied until the specimen fails, which almost always occurs in shear. Cell pressure is kept constant during the test. Specimens in the author's test program were compressed at a constant rate of axial strain, ε_1, of 0.0052% per minute while measuring the axial load, axial compression, and changes in pore water pressure. The strain rate was kept low so that any changes in internal pore water pressure were captured by the pore water pressure transducer at the base of the triaxial cell. Consolidated undrained triaxial tests do not permit drainage so there were changes in pore water pressure but not in volume. The shear stage was stopped once at least 15% strain had been reached or a shear plane developed in the specimen.

Triaxial tests must be conducted with at least three different effective confining stresses to develop a strength envelope for the soil (the effective confining stress is the difference between the cell pressure and the back pressure, $\sigma'_3 = \sigma_3 - u_b$). Effective confining stresses of 50, 100, and 150 kPa were used. A back pressure of 200 kPa was used to help achieve saturation of the specimen and the test equipment, and therefore more reliable pore water pressure measurements; that is B $\geq$ 0.98.

Results of the consolidated undrained triaxial tests are summarized in Table 3.4. The results from one test from 2012 was left out of the plots but was included in the Appendix. It passed the B-Test, but the results in the shear stage did not conform to typical behaviour of clays during unconsolidated triaxial tests. Upon examination after the test, the O-rings that secured the latex membrane in place were found to have slipped. The membrane was filled with water which probably affected the behaviour during the shear stage.

Figure 3.19 and Figure 3.20 show of the combined results from the four-inch (101.6 mm) diameter specimens taken from the shoulder in 2012 tested by the author (shown as solid lines) and the two-inch (50.8 mm) diameter specimens from the toe in 2008 that were previously tested (shown as dashed lines). Results were plotted as the deviatoric stress, q, versus the axial strain, ε_1, in Figure 3.19 and as the deviatoric stress, q, versus mean principal effective stress, p' in Figure 3.20. The calculations for deviatoric stress and mean principal effective stress are shown in Equation 3.7 and Equation 3.8, respectively.

[Eq. 3.7] $q = \sigma_1 - \sigma_3$

[Eq. 3.8] $p' = \frac{\sigma'_1 + 2\sigma'_3}{3}$

Towards the end of shear testing, these specimens approached steady-state conditions as changes in pore water pressure gradually decrease, while mean principal effective stress sand deviatoric stress also approach constant values. The behaviour is more evident in normally consolidated clays than over-consolidated clays. Critical state represents the state of a soil when it approaches idealized steady-state conditions. The technical definition of critical state is expressed in Equation 3.9.

[Eq. 3.9] $\frac{\partial p'}{\partial \epsilon_s} = \frac{\partial q}{\partial \epsilon_s} = \frac{\partial \epsilon_v}{\partial \epsilon_s} = \frac{\partial u}{\partial \epsilon_s} = 0$

where ε_s and ε_v represent the axial and volumetric strains, respectively.

Critical state, represented by the Critical State Line, can only be achieved if all four of the conditions defined in Equation 3.9 occur simultaneously. The intersection of the Critical State Line (CSL) with the yield locus in p'–q space represents the critical state of the specimen where the soil has yielded and there is no more change in deviatoric stress and pore water pressure (Wood, 1990). The CSL, with slope M, is shown in Equation 3.10 and was used to characterize the strength behaviour of the soil.

[Eq. 3.10] $\quad \phi'_{cs} = \sin^{-1}\left(\frac{3M}{6+M}\right)$

where the cohesion, c, is assumed zero and ϕ'_{cs} is the critical state friction angle.

The CSL is represented by the red line drawn on Figure 3.20 and has an approximate value of 1.29. Based on Equation 3.10, the critical state friction angle is 32°. Critical state friction angle values are not affected by specimen size.

Failure occurs at $(\sigma'_1/\sigma'_3)_{max}$ according the Mohr-Coulomb failure criterion defined in Equation 3.11 (Budhu, 2007).

[Eq. 3.11] $\quad M = \left(\frac{p}{q'}\right)_{max} = \frac{6\sin\phi'}{3-\sin\phi'}$

Table 3.4 summarizes the results of the consolidated undrained triaxial tests of the four-inch (101.6 mm) diameter specimens taken from the shoulder in 2012. The table shows that the peak friction angles of the specimen using the Mohr-Coulomb failure criterion were in the range of 29° and 40°. The peak friction angle for clay is typically in the range 15° to 30° (Budhu, 2007). However, no large difference was found when compared to the peak friction angles of the smaller two-inch (50.8 mm) diameter samples taken beneath the toe of the embankment during drilling in 2008. The peak friction angles from the 2008 specimens ranged between 28° and 42°, and behaviour of the specimens during the triaxial tests have been previously described in Batenipour (2012).

The effects of sampling disturbance at the circumference of specimens should be reduced if larger specimens are used because of reduced edge effects. The test results should, therefore, better represent the properties of the field material. The author did not observe any improvement between the results of the tests performed on two different sized specimens; the range of peak friction angles was very similar. There was added difficulty in obtaining larger four-inch (101.6 mm) diameter samples due to the presence of frozen ground. All Shelby tubes pushed into the frozen ground were damaged and the field crew was unable to obtain a full length sample. These tests demonstrate that the use of a smaller diameter specimen at this test site was sufficient to characterize the strength behaviour of the soil.

3.4. Summary

This chapter covered the characterization of the project site and laboratory testing of samples from the site. Approximately 6 m of gravel fill is underlain by 14 m of silty clayey before reaching gneissic bedrock at 18 m depth. Drilling in 2008 showed no frozen soil at the toe of the embankment despite encountering some in 1991 and 2005. Drilling in 2012, however, revealed ice-rich soil between 6 m and 9 m depths at the shoulder and between 4.5 m and 11 m depth under the centreline. Regular maintenance has applied additional gravel each year for re-grading to compensate for settlements.

A geophysical investigation conducted at the site used Ground Penetrating Radar (GPR) and the OhmMapper electrical resistivity surveys. A large area of elevated resistivity was encountered under the embankment in the OhmMapper survey. The region was consistent with the locations where ice-rich soil was encountered during drilling. The results of the GPR were not conclusive in this particular instance. Quality equipment and experienced operators of the

ground penetrating radar are needed to interpret the results and obtain detailed and accurate profiles.

A series of laboratory tests was carried out to understand the soil properties under the embankment and supplement data from tests conducted during the initial research in 2008. Four-inch diameter (101.6 mm) diameter Shelby tube soil samples were taken at the shoulder in 2012 for laboratory tests that included water content, Atterberg limits, hydrometer analysis, one-dimensional consolidation oedometer tests, and consolidated undrained triaxial (CIŪ) tests.

The liquidity indices and water contents increased with depth. Lower water contents near the ground surface reflected the exposure to weathering like freezing-thawing or wetting-drying processes. At greater depths, in some cases, the water content exceeded the liquid limit. Higher liquidity indices and moisture contents usually are linked to lower shear strengths, and consequently the soil becomes softer and weaker at greater depths. The specimens from 2012 at the shoulder generally had a greater proportion of silt compared to the specimens from 2008 at the toe. Silts usually relate to lower liquid limits, and the specimens at the shoulder with more silt had liquid limits generally less compared to the toe.

Oedometer tests examined the compression and consolidation behaviour of the clay. The preconsolidation effective stress decreased with depth in both 2012 and 2008 specimens and was attributed to weathering processes close to the surface. The compression and recompression indices calculated at the shoulder were consistent with values calculated at the toe except the higher values of specimen T5 from the shoulder. Higher compression indices are associated with higher plasticity indices, higher water contents, and higher liquidity indices. It is possible specimen T5 was weakened because previously frozen soil had thawed. The secondary compression index was examined using an extended interval for the final load application. The

ratio between secondary compression indices, $C_{\alpha e}$, and compression indices, C_c, of the specimen from 2012 are lower than those from the specimens in 2008. Batenipour (2012) attributed lower values of the ratio to the relatively large silt component of the soil.

The author conducted consolidated undrained triaxial (CIŪ) tests on four-inch (101.6 mm) diameter specimens. These specimens were larger than the more conventionally sized two-inch (50.8 mm) diameter specimens that were tested in 2008. The critical state angle of the specimens tested in 2012 was 32°. The peak friction angles based on the Mohr-Coulomb failure criterion for specimens tested in 2012 were between 29° and 40°, consistent with the tests conducted in 2008. In theory, the precision and accuracy of the results should improve with larger diameters specimens because of the reduced edge effects. However, there was no discernable improvement with the larger diameter specimen, and results from 2012 were consistent with results from 2008.

Table 3.1: Summary of Specimens and Tests Performed on 2012 Samples taken from the Shoulder

Sample	Depth [m]	Length [mm]	Atterberg	Hydrometer	Moisture	Oedometer	Triaxial
T3	5.0 – 5.6	510	X	X	X		2
T4	5.6 – 6.1	480	X	X	X	X	2
T5	6.1 – 6.6	165	X	X	X	X	
T6	6.8 – 7.0	180	X	X	X		
T7	9.7 – 9.9	205	X	X	X	X	
T8	11.7 – 12.3	610	X	X	X	X	2

Table 3.2: Test Summary for Moisture Contents, Atterberg Limits, and Hydrometer Analysis on 2012 Samples taken from the Shoulder

Test	Depth	w_P	w	w_L	I_P	I_L	Clay [%]	Silt [%]
T3	5	20.6%	30.3%	40.4%	19.8%	0.5	57%	43%
T4	5.6	24.7%	35.2%	37.7%	13.0%	0.8	40%	60%
T5	6.2	16.9%	31.8%	34.6%	17.8%	0.8	48%	52%
T6	6.9	20.6%	40.6%	33.0%	12.4%	1.6	43%	57%
T7	9.8	18.5%	42.8%	36.4%	17.9%	1.4	39%	61%
T8	11.8	18.3%	42.8%	37.4%	19.1%	1.3	63%	37%

Table 3.3: One-dimensional Consolidation Results on 2012 Samples taken from the Shoulder

Test	Depth [m]	σ'_{zc} [kPa]	C_c	C_r	$C_{\alpha e}$	$C_{\alpha e}/C_c$
T4	7.6	73	0.104	0.037	0.0054	0.052
T5	8.2	66	0.378	0.022	0.0078	0.021
T7	9.8	52	0.175	0.068	0.0048	0.027
T8	12	94	0.131	0.012	0.0038	0.029

Table 3.4: Consolidated Undrained Triaxial Test Results of Four Inch Diameter Samples taken from the Shoulder in 2012

Test	Depth	σ_3 [kPa]	u_b [kPa]	σ'_3 [kPa]	M_{max}	ϕ'_{peak}
T4	5.6	250	200	50	1.47	36.2°
T3	5	250	200	50	1.61	39.3°
T3	5.3	300	200	100	1.63	39.9°
T8	12	350	200	150	1.25	31.2°
T4	5.9	350	200	150	1.14	28.6°
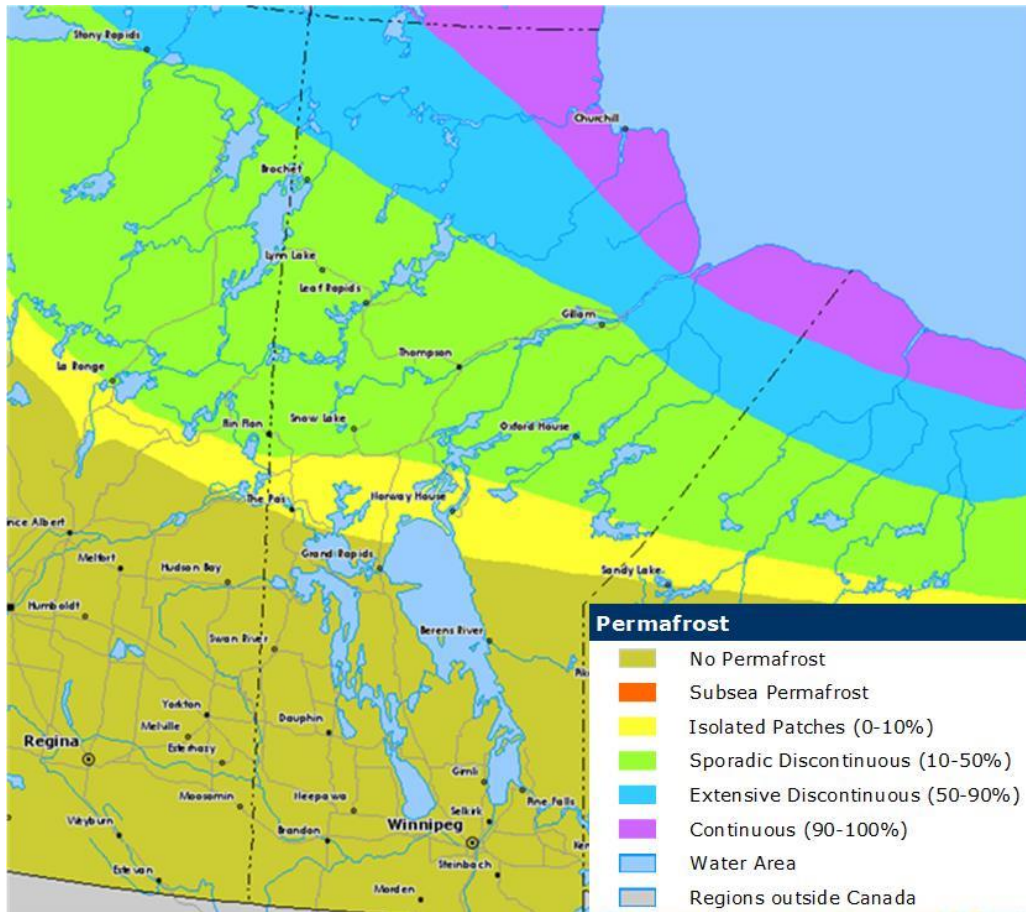
Figure 3.1: Permafrost in Manitoba (NRC, 2012)

Figure 3.2: Settlement due to Permafrost Conditions on the Hudson Bay Railway north of Thompson. October 21, 2012.
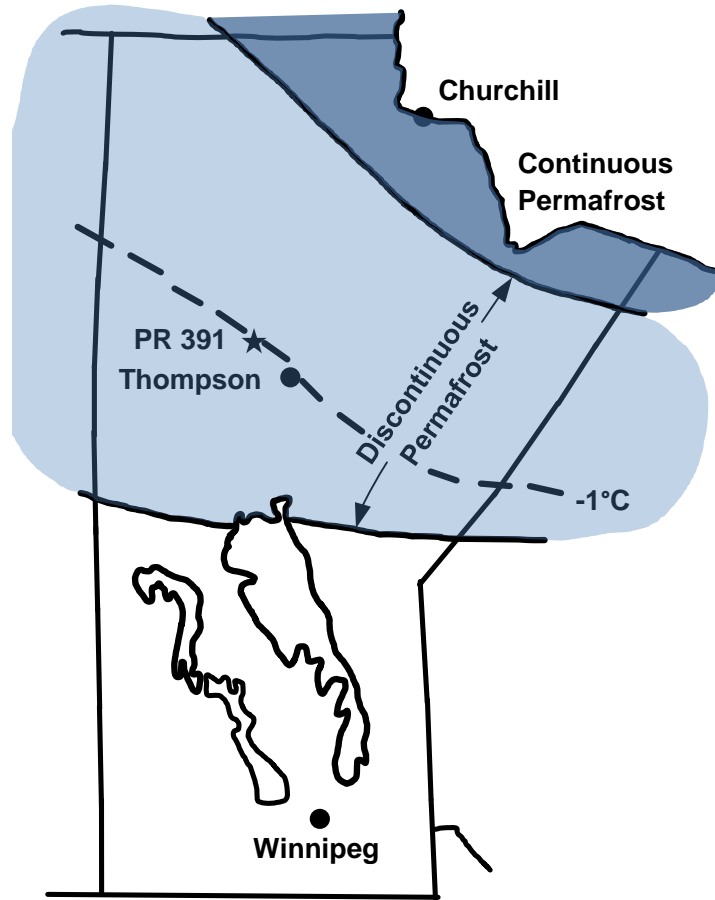
Figure 3.3: Location of PR 391 Research Site (Flynn, 2013)

Figure 3.4: PR 391 Project Site. September 10, 2012.

Figure 3.5: Frozen ground and ice encountered at the shoulder. September 11, 2012.
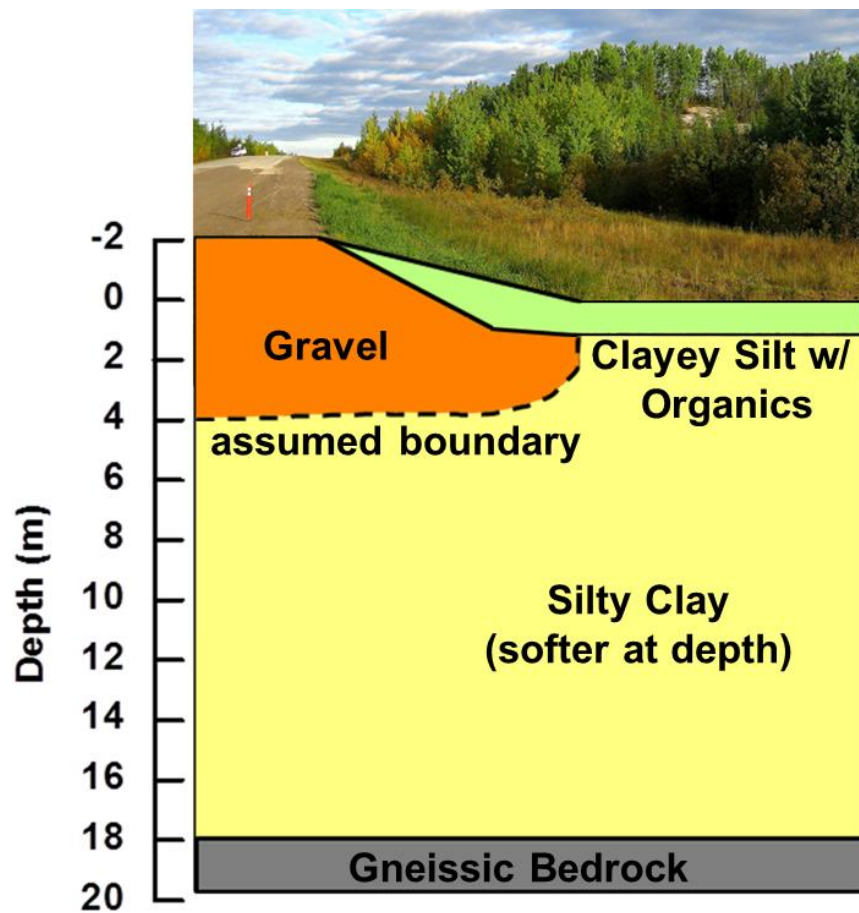
Figure 3.6: Approximate Cross Section of Project Site
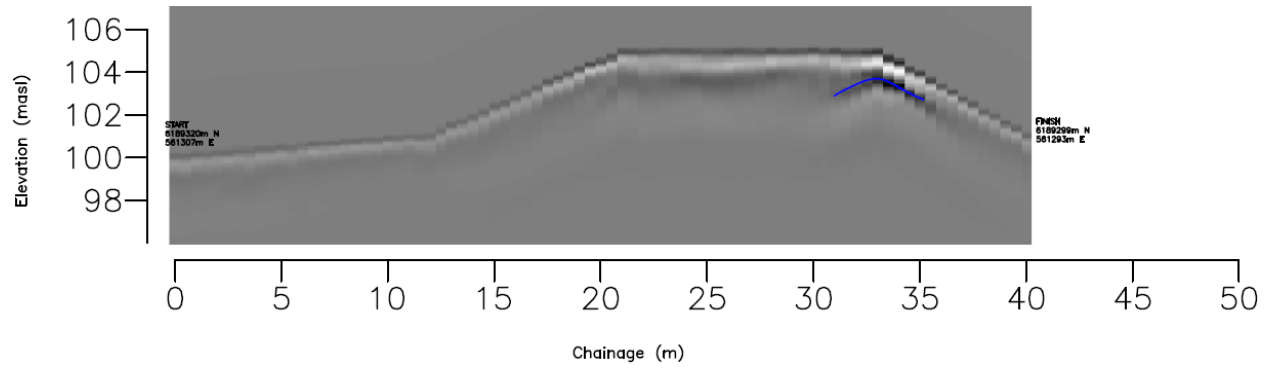
Figure 3.7: GPR Results with 50 MHz Antenna
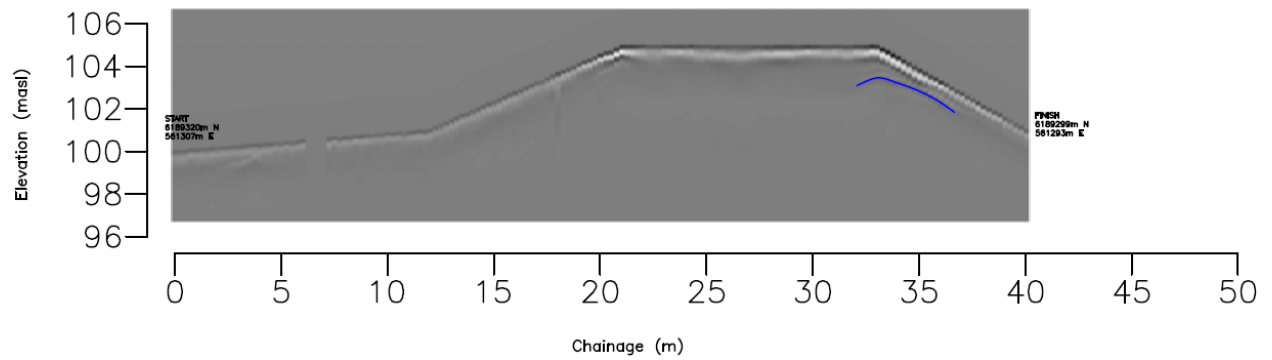
Figure 3.8: GPR Results with 100 MHz Antenna
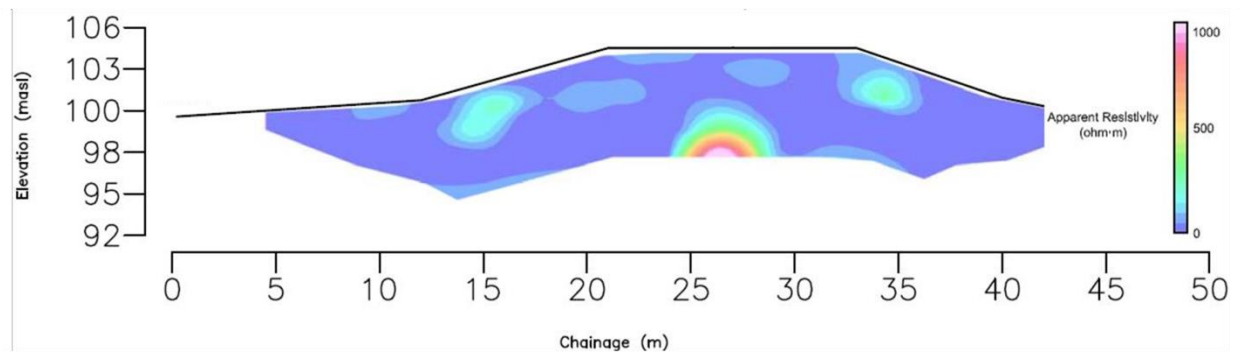
Figure 3.9: OhmMapper Results

Figure 3.10: Damaged four inch Shelby tube obtained from the shoulder. September 11, 2012.
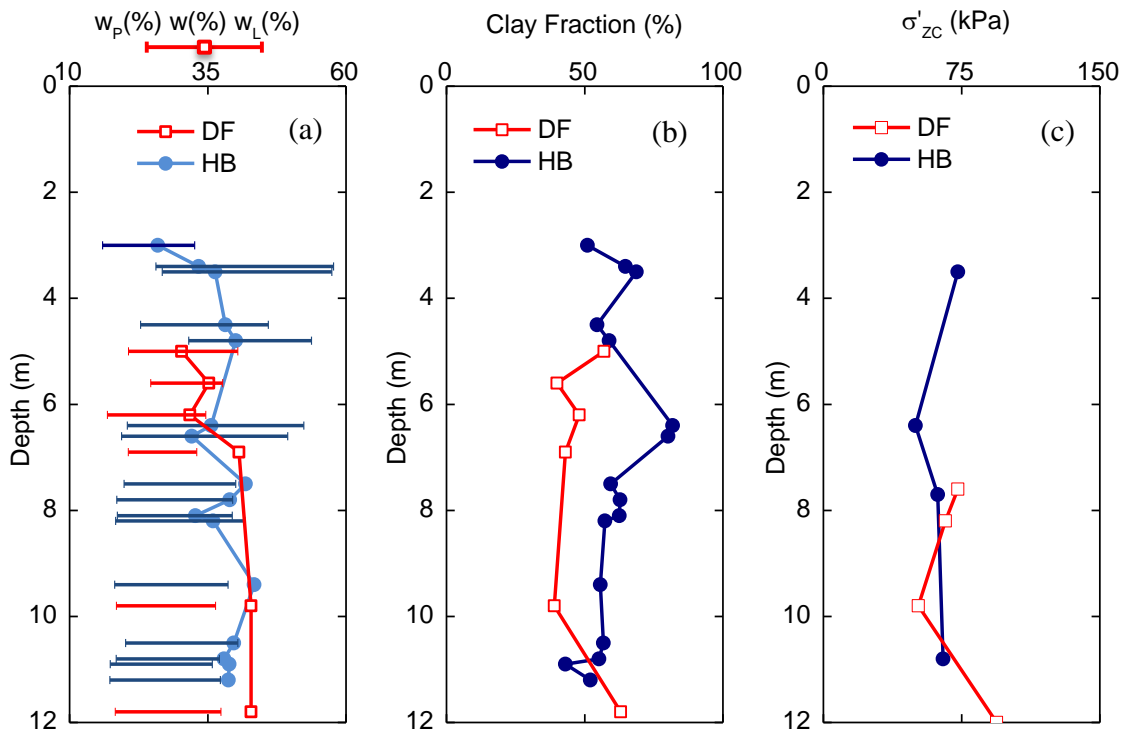
Figure 3.11: Laboratory test results from Batenipour 2008 (blue) and Flynn 2012 (red). (a) Moisture contents and Atterberg Limits (b) Clay fraction from Hydrometer Analysis (c) Preconsolidation Pressure from Oedometer.
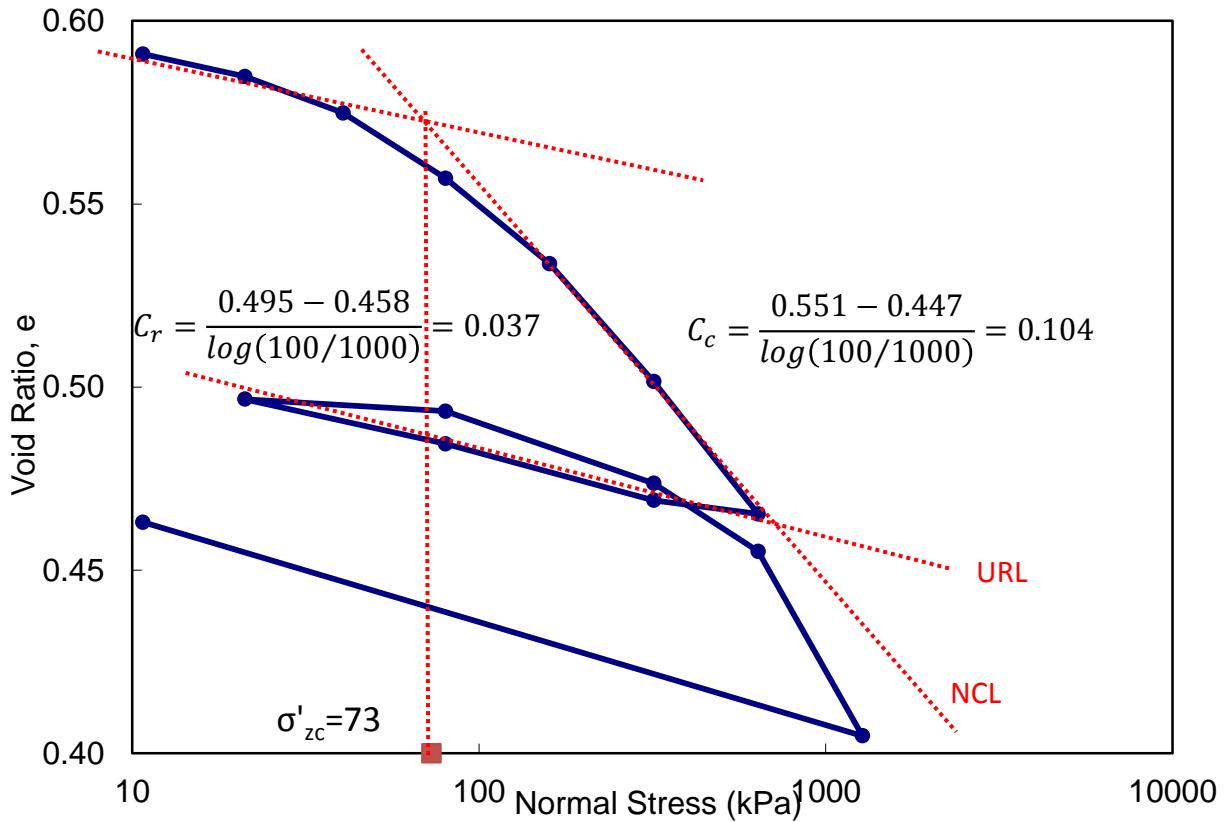
Figure 3.12: Example plot of void ratio (e) versus log normal stress (σ'_z) and sample calculations for C_c, C_r, and σ'_{zc} for sample T4
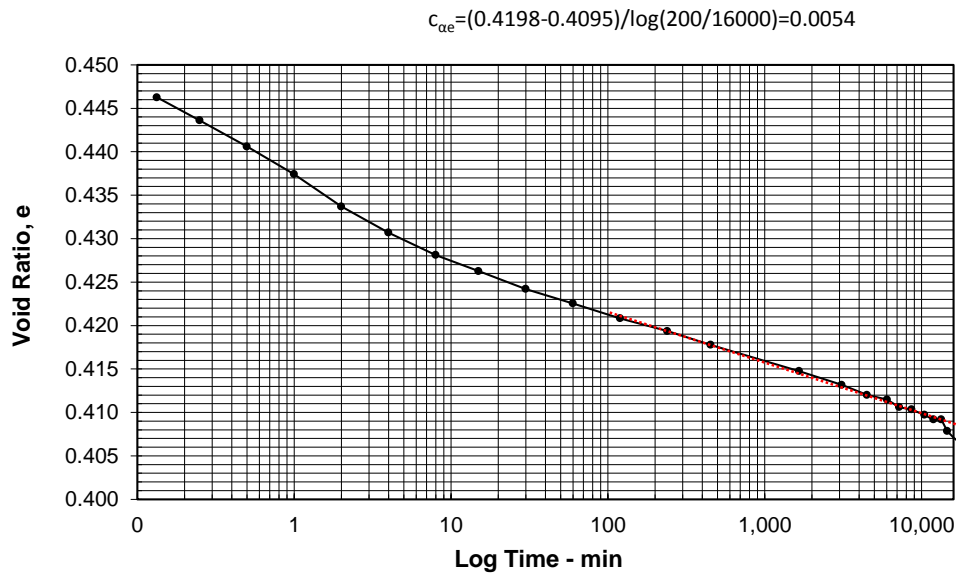
Figure 3.13: Example plot of void ratio, e, versus log of time for calculation of Cae for T4 under an applied vertical stress of 1280 kPa
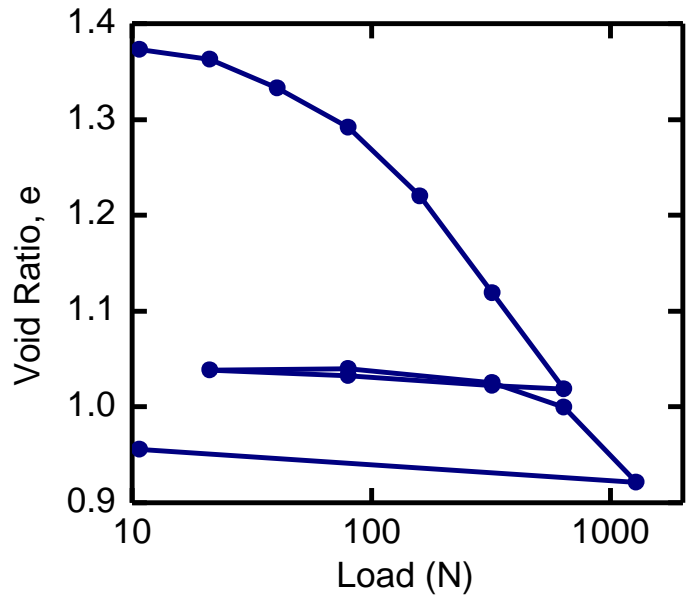
Figure 3.14: Void ratio versus log-scale of normal stress for the oedometer test of sample T5
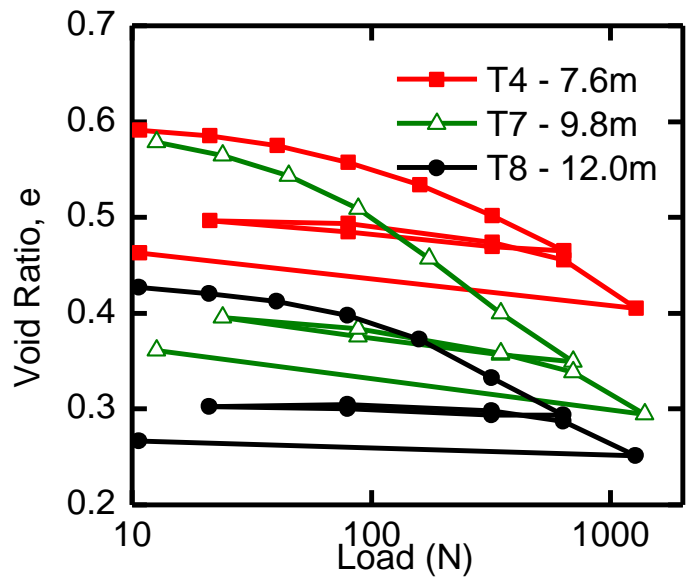
Figure 3.15: Void ratio versus log-scale of normal stress for the oedometer test of samples T4, T7, and T8
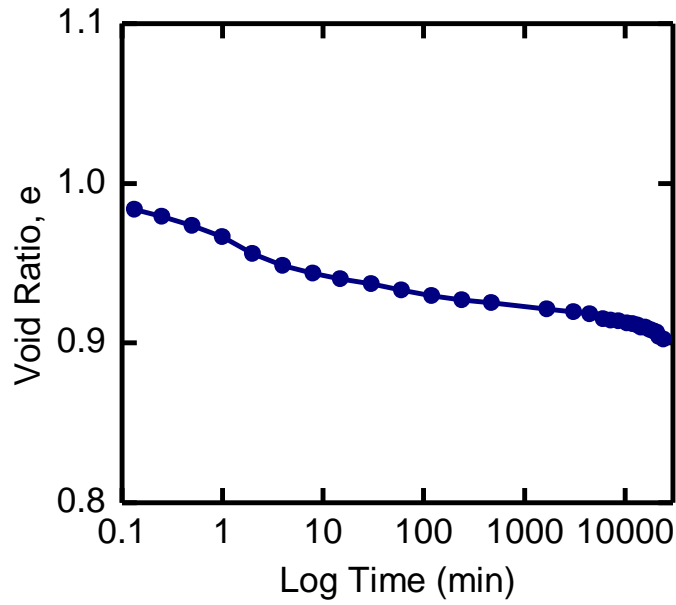
Figure 3.16: Void ratio versus log-scale of time for oedometer test of sample T5
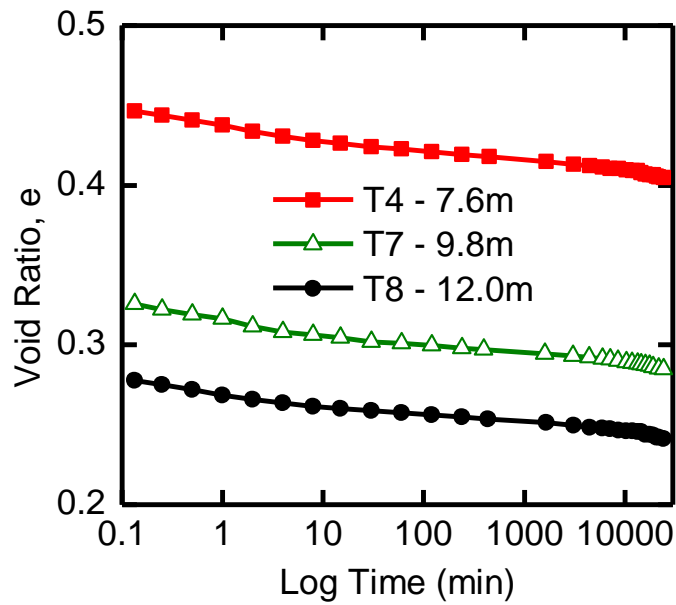
Figure 3.17: Void ratio versus log-scale of time for oedometer test of samples T4, T7, and T8
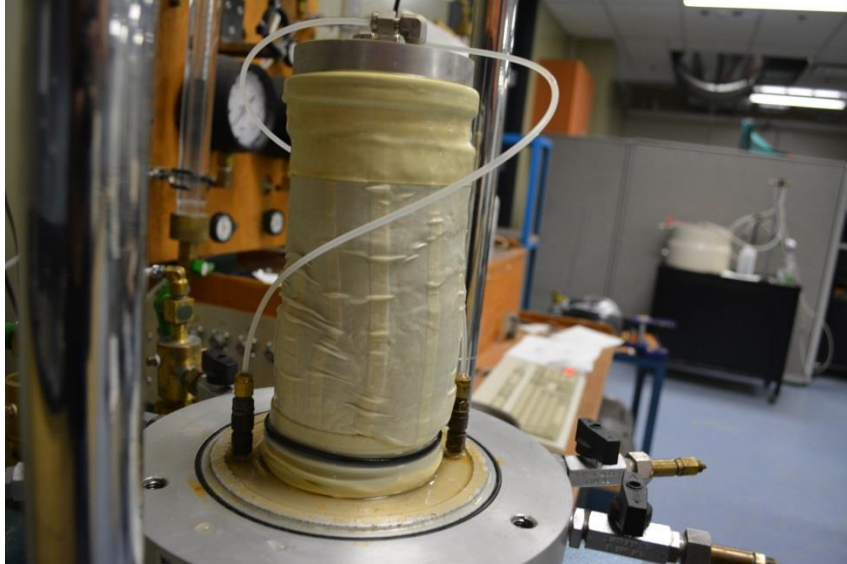
Figure 3.18: Consolidated Undrained Triaxial Test of 4-inch diameter Specimen T4. February 28, 2014.
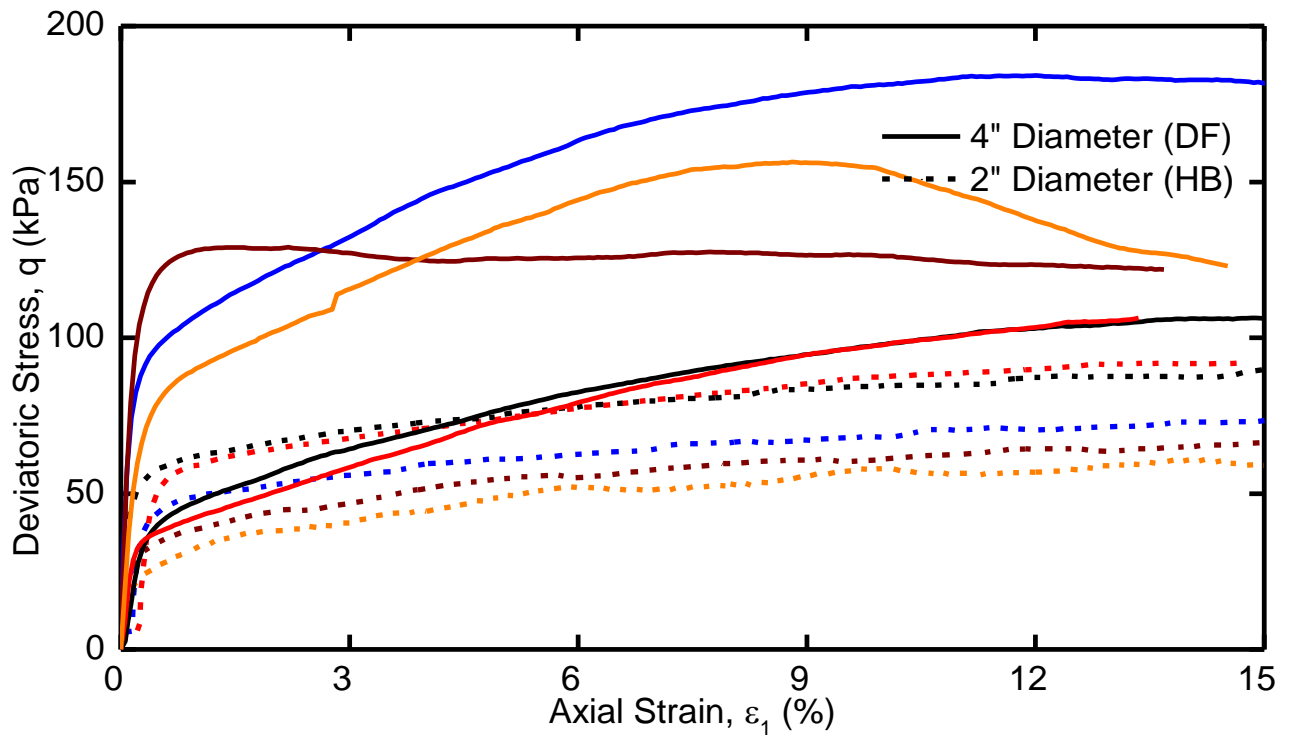
Figure 3.19: Triaxial Test Plot of Deviatoric Stress, q, versus Axial Strain, ε_1. Tests on four-inch diameter specimens from 2012 are solid lines. Tests on two-inch diameter specimens from 2008 are dash lines.
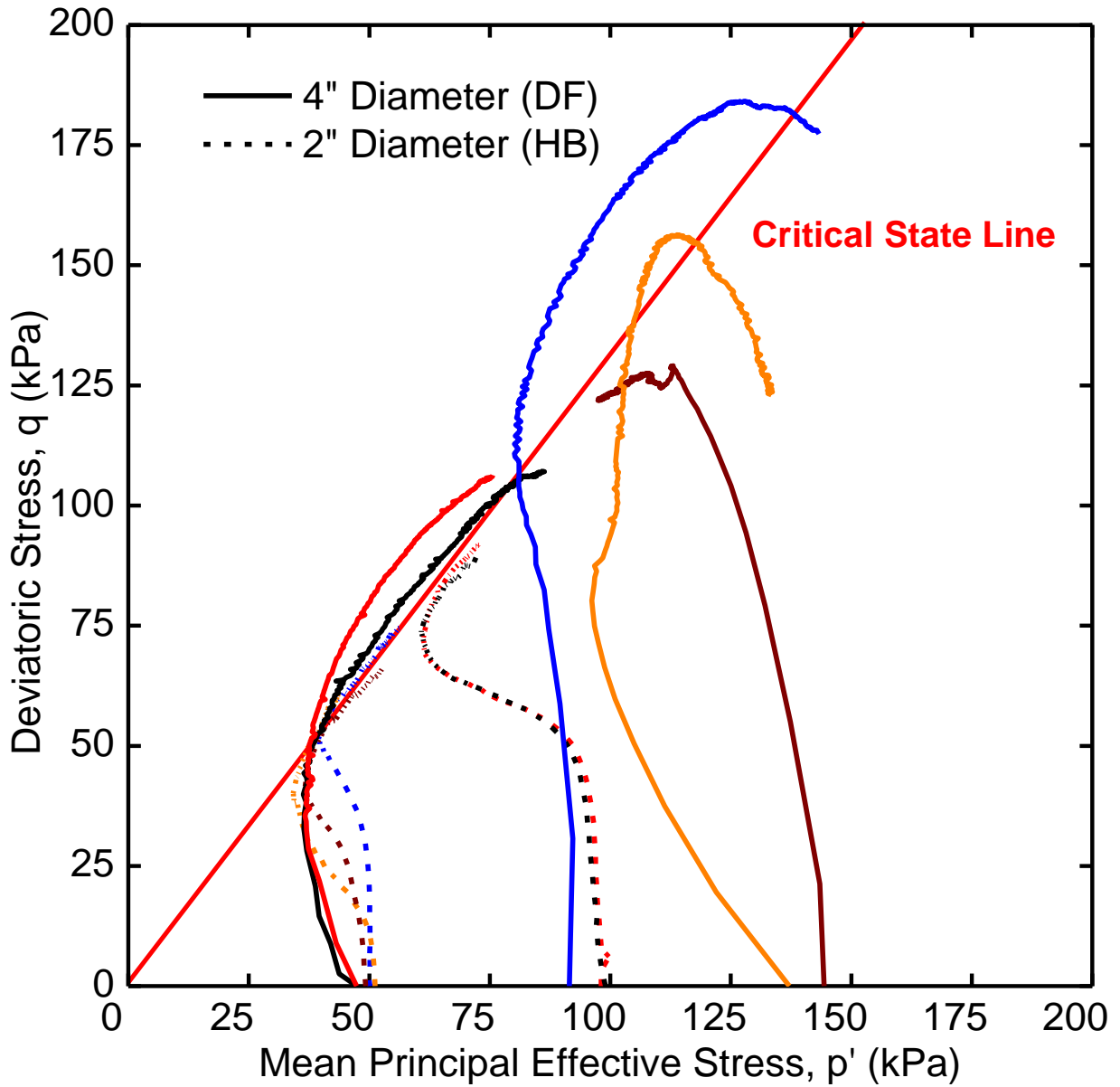
Figure 3.20: Triaxial Test Plot of Deviatoric Stress, q, versus Mean Principle Effective Stress, p'. Tests on four-inch diameter specimens from 2012 are solid lines. Tests on two-inch diameter specimens from 2008 are dash lines.

Chapter 4: Instrumentation, Monitoring, and Field Measurements

4.1 Introduction

Twelve (12) instruments were monitored for this research project at the PR 391 site shown in Figure 4.1. Instrumentation included of four (4) instruments installed during the initial research program in October 2008 and an additional eight (8) instruments installed by the author in September 2012. The initial research program only monitored data at the toe and mid slope of the embankment. The author expanded the research program to monitor data at the shoulder and centreline as well. Instruments included four (4) thermistor strings, six (6) vibrating wire piezometers, and two (2) ShapeAccelArrays (SAAs). Parameters that have been monitored include temperature, pore-water pressure, and both lateral and horizontal displacement. The instruments have a total of 137 sensors, as piezometers and SAAs each contain a primary sensor and a secondary sensor to measure temperature. Data from the instruments were collected remotely via satellite using an internet connection. Mechanically or weather induced communication disruption demanded several return visits to improve the data acquisition system.

4.2 Instrumentation

This section outlines instrumentation used at the site and its purpose. Instrumentation was first installed at the site in October 2008 during the initial research program. The instrumentation installed at that time included thermistor strings, vibrating wire piezometers, standpipes, surface settlement plates, slope inclinometers, and vibrating wire extensometers. Drilling on the road surface was not allowed during the initial monitoring program and the instrumentation was limited to the toe and mid slope of the embankment. For the second phase of research, Manitoba

Infrastructure and Transportation (MIT) gave the author permission to drill on the road surface and expand the monitoring program to the shoulder and centreline. In September 2012, the author installed two (2) thermistor strings (at the shoulder and centreline), four (4) vibrating wire piezometers (under the centreline), and two (2) ShapeAccelArrays (vertically at the shoulder and horizontally between the toe and the centreline). A new data acquisition system allowed data from the instrumentation to be collected remotely and is discussed in Section 4.4 Data Acquisition System. Data from four (4) of the instruments installed in October 2008 continued to be collected by the author as part of the new monitoring program because they were easily integrated into the remote data acquisition system. These included two (2) vibrating wire piezometers (under the toe), and two (2) thermistor strings (at the toe and mid slope). The author did not monitor the standpipes, surface settlement plates, and slope inclinometers from the initial monitoring program because those instruments required on-site data collection. A more detailed description of the initial monitoring program can be found in Batenipour et al. (2010). Figure 4.2 shows a cross section showing approximate locations of all instruments monitored by the author's research program. The different colours in the figure distinguish the instrumentation installed during the initial research program in October 2008 (shown as blue) from the additional instrumentation installed by the author in September 2012 (shown as green).

4.2.1 Temperature

Thermistor strings manufactured by RST Instruments were installed at the toe, mid slope, shoulder, and centreline of the embankment to monitor the ground temperature regime. They were selected because of their high accuracy, sensitivity, and compatibility with remote access data acquisition systems. Thermistors are thermally sensitive resistors composed of semiconductor materials that noticeably change their resistance in response to changes in temperature (Dunniclif and Green, 1988). Data acquisition systems apply a small current to the thermistors and the resulting resistance relates to the temperature of that thermistor.

The thermistor strings were custom-manufactured to provide the required length, and the desired quantity and location of nodes. The thermistor strings manufactured by RST Instrument used in this project can measure temperatures between -80°C and +75°C within a tolerance of ±0.1°C (RST Instruments, 2014). Nodes (points) along the thermistor string measure temperature and have the appearance of small, black beads. Each node contains an interchangeable, curve tracking, negative temperature coefficient (NTC) thermistor (RST Instruments, 2014). The signal cable used to transmit temperature data from each node to the data acquisition system is encased by a heavy duty burial cable to protect it from physical damage and water penetration.

In 2008, 9-point thermistor strings were installed at the toe and mid slope of the embankment. The nine nodes were spaced at 1 m intervals to a depth of 9 m below the elevation of the toe. In 2012, the author installed 13-point thermistors at the shoulder and the centreline so examination of the thermal regime under the embankment could be expanded. One of the thermistor strings is shown in Figure 4.3 just prior to installation. The nodes are obscured by the black electrical tape attaching the thermistor string to the PVC pipe which was used to guide the thermistor string to the proper depth. The diameters of the node and cable in the 13-point

70

thermistors were 19.05 mm and 10.41 mm, respectively. Thermistor strings with more than thirteen nodes require a wider diameter burial cable which was too large to fit in the PVC pipe used to guide the burial cables to the data acquisition system. The armouring of the thermistor strings will be discussed in greater detail in Section 4.3 Armouring and Installation. The upper nine nodes were spaced at 1 m intervals and matched the depths of the thermistor strings at the toe and mid slope. The lower four nodes were spaced at 2 m intervals to a depth of 17 m below the surface and just above the bedrock. The spacing for the lower nodes was larger because the temperatures at these depths were not expected to vary as much over the course of a year. Thermistor strings were not rigorously examined in the laboratory, and only measured temperature of the laboratory and a cold chamber set to -3°C. Temperature readings were deemed acceptable. Factory calibration sheets are included in the Appendix.

4.2.2 Pore Water Pressure

Multi-Level Vibrating Wire Piezometers manufactured by Slope Indicator measured pore water pressure at the site. The vibrating wire piezometers were selected because they accurately obtain readings remotely while connected to a data logger. Vibrating wire piezometers measure pore water pressure by relating calibration factors to the vibrating frequency of a tensioned steel wire (Dunnicliff and Green, 1988). A vibrating wire consists of a tensioned steel wire, a diaphragm, and an electromagnetic coil. The steel wire is held in tension by wire grips on one end and the diaphragm on the other. The flexible stainless steel diaphragm is exposed to the external environment and is sensitive to changes in pressure which in turn changes the tension in the steel wire. The tension of the steel wire is proportional to the square of the frequency of its vibration. The data acquisition system uses factory supplied calibration factors to convert the raw frequency readings into pore water pressures.

A multi-level vibrating piezometer is a variant of the standard borehole piezometer as it can monitor pore water pressures at different elevations in the same borehole (Slope Indicator, 2013). The piezometers shown in Figure 4.4 are hermetically sealed and encased in a special housing with fittings on either end that are attached to PVC pipes. The pipes are cut to customized lengths allowing the piezometers to be placed at pre-determined depths. Signal cables from the piezometers run through the PVC pipe to the data acquisition system The PVC pipes provide physical protection to the cables and limit opportunities for water leakage to infiltrate and damage the data acquisition system. The piezometers are secured by a bentonite-cement mixture of grout pumped through the pipe. The grout is responsive to changes in pore water pressure while isolating adjacent piezometers from one another.

Vibrating wire piezometers were installed at the centreline in 2012. They were installed at depths of 5.2 m, 9.2 m, 13.2 m, and 17.5 m below the elevation of the toe. They were the same model of the vibrating wire piezometers installed at the toe in 2008 at depths of 4.5 m and 8.7 m. All piezometers could measure up to 350 kPa. The housing was 12-inches (304.8 mm) in length and 2.8-inches (71.1 mm) in diameter. The signal cable was covered in a polyurethane coat and consisted of a grounding wire and two pairs of twisting 24 gauge wire which transmitted pore water pressure and temperature data. A PVC pipe with a 1.25-inch (31.8 mm) diameter connected to the fittings on the housing, and could accommodate up to six signal cables, although only four were required. All six vibrating wire piezometers were included in the monitoring program.

Calibration testing was done at the University of Manitoba and compared to factory supplied calibration values. The piezometers were lowered into a large storage tank in the hydraulics laboratory and also into a column of water in the geotechnical laboratory. The water

depth was known so the expected pore water pressures were compared to readings recorded by the piezometers. Calibration constants were calculated and differed only slightly from factory supplied values. Calibration data are found in the Appendix.

4.2.3 Displacement

ShapeAccelArrays (SAAs), as shown in Figure 4.5, manufactured by Measurand monitored displacements in the embankment. The first SAA was installed vertically at the shoulder of the embankment to measure lateral displacement. The second SAA measured vertical displacement and was installed horizontally between the toe and centreline of the embankment. Slope inclinometers were installed in the 2008 research but monitoring was discontinued because a person was required to collect the data on site. SAAs possessed a greater range of measureable displacements compared to slope inclinometers, and could also be accessed through the remote data acquisition system.

In 2012, ShapeAccelArrays were installed vertically at the shoulder to measure lateral displacement and horizontally between the toe and centreline to measure vertical displacement. Measurand offers field and research versions of the SAA. The SAA field option was chosen over the research option because of its longer lengths, lower power consumption, and fewer required signal cables. The vertical SAA was 16 m long while the horizontal SAA was 20 m long.

An SAA is comprised of a series of rigid 0.5 m long segments containing triaxial micro-electronic-mechanical system (MEMS) gravity sensors that measure tilt along three axes (Measurand Shape Advantage, 2012). Long term accuracy for 30 m long SAAs is 1.5 mm. SAAs use rotational transforms based on the tilt measurements to calculate 2D and 3D shapes for horizontal and vertical installations, respectively. The joints separating each segment can bend beyond 45° which allows for greater displacement measurements than slope inclinometers. SAAs

73

are divided into eight segment groupings called sub-arrays or octets. Temperature sensors are located in the centre of each octet. The last segment on each end of the SAA is called the anchor segments. Anchor segments do not contain sensors so that each end could be used to connect the signal cable to the data acquisition system to transmit the SAA data. The signal cable is protected from physical damage by an internal and external layer of stainless steel braid.

One anchor segment must be fixed in position for the entire monitoring period to serve as a reference point for tilt measurements. Nearly-vertical SAA installation typically use a far end reference point while horizontal installation usually anchors the near end. Installation of the SAA is discussed further in Section 4.3 Armouring and Installation.

4.3   Armouring and Installation

Suitable armouring to protect the instrumentation and proper installation enabled the instrumentation to function for the duration of the author's monitoring program with minimal maintenance. Armouring funnelled the instrumentation cables through PVC pipes to data acquisition and provided additional protection from physical damage. The installation methods were based on a combination of recommended practices, experience, and site specific considerations gained from the 2008 installation. Armouring and installation of the instrumentation began with an initial trip from September 9 to 16, 2012, but the drillers were unable to complete all the required boreholes. A second trip between September 23 and 26, 2012 was required to conclude the installation.

Installation of the thermistor strings and vibrating wire piezometers followed a similar procedure. PVC pipes cut to specific lengths were used to ensure the vibrating wire piezometers and thermistor strings reached their pre-determined depths. Thermistor strings were taped to

PVC pipes, as shown in Figure 4.3, and pushed down the borehole. PVC pipes attached to the piezometer fittings as shown in Figure 4.6. PVC pipes with the attached instruments were fed through the hollow stem drill bits that kept the boreholes unobstructed as shown for the installation of the thermistor string at the shoulder in Figure 4.7. The full lengths of the PVC pipes used for the thermistor strings and piezometers would have been extremely difficult and awkward to manipulate into the borehole as one cohesive unit. Shorter sections of PVC pipes, no more than 6 m long, were much easier to manoeuvre into the boreholes as shown in Figure 4.8. Additional sections were glued together when they reached the top of the borehole. The instruments were quickly grouted into place with a bentonite-cement mixture because the buoyant force of water in the borehole pushed the PVC pipe towards the surface. For the SAA installed vertically at the shoulder, a PVC pipe was pushed down the borehole and weighed down with a metal chain while it was grouted in place with the same bentonite cement mixture. The chain was removed and the SAA was then fed into the PVC pipe as shown in Figure 4.9. The far end of the SAA was grouted in the bedrock to serve as its anchor point.

The installation of the horizontal SAA required a different approach. A local contractor drilled horizontally through the embankment beginning at the toe using multi-directional drilling equipment as shown in Figure 4.10. The length of the SAA would only reach the centreline, but it was easier to install the SAA if the drilling penetrated the other side of the embankment. A PVC pipe was pushed through to the other side, and then a stiff steel wire was fed back through the PVC pipe. The wire was attached to the far end of the SAA and pulled through the PVC pipe as shown in Figure 4.11 until the near end of the SAA had entered the PVC pipe.

The near end of the SAA was to be fastened at the toe to serve as the reference point for tilt measurements. Initially surplus bentonite-cement grout was used to secure the SAA.

However it concerned the author that if the entire embankment slope moved from such events as freezing and thawing, the grout might not be sufficient to prevent movement at the near end of the SAA. The vertical displacement measurements are relative to the anchor point and if that anchor moves with the rest of the embankments, the results could be affected. The concerns were first addressed with an additional site visit. On December 1, 2012, a foot-long U-shaped piece of rebar was hammered into the ground and secured to the SAA as shown in Figure 4.12. On November 14, 2013, the rebar anchor was replaced with an 8-foot (2.4 m) long ground anchor, as shown in Figure 4.13. The effect the different anchors had on the displacement measurements will be addressed in Section 4.5.3 Ground Movements.

Signal cables were armoured in PVC pipes to provide physical protection between the embankment and the data acquisition system. Figure 4.14 shows the thermistor string signal cable being fed into PVC pipe at the shoulder of the embankment. PVC glue connected the joints of the PVC pipes (shown in Figure 4.15), and reduced opportunities for water to infiltrate and damage the data acquisition system. All signal cables from the 2012 installation went through a single PVC pipe as shown in Figure 4.16. The armouring was placed in a one-foot (0.3 m) deep trench, shown in Figure 4.17, which was deep enough not to be disturbed when the gravel road surface was re-graded. The trench continued down the embankment slope towards the data acquisition system as shown Figure 4.18. Final connections into the data acquisition were tricky because the signal cables tend to coil as they make multiple tight turns inside the 1.25-inch (31.8 mm) diameter PVC pipe. A combination of precision cutting of the PVC pipes and strength were needed to pull the cables through the tight corners as shown in Figure 4.19.

4.4   Data Acquisition System

The data acquisition (DA) system collected readings from the instrumentation and was accessed remotely using a satellite system. Remote access enabled the author to download data files and upload modifications to the code that controlled the monitoring schedule from any location with an internet connection. Solar energy powered the DA system as the site was unconnected to the electrical power grid. The DA system set up occurred in September 2012 in conjunction with the instrumentation installation. Several return site visits were required to address communication disruptions caused by weather and mechanical breakdowns that prevented data from being collected.

The DA system was accessed remotely with the satellite communication system that was installed at the project site. Remote access eliminated the need to have an operator visit the site to manually download the data. The initial 2008 monitoring program required an operator on site to collect data files directly from the DA system. The operator was an engineer from the MIT office in Thompson who visited the site once a month to collect data. The satellite communication system enabled any operator with LoggerNet software, internet access, and the IP address of the satellite system to access the DA system. Communication worked both ways so data could be downloaded from the DA system, and modification to the code to change the monitoring schedule could be uploaded into the DA system. The author was able to access the DA system regularly from Winnipeg and even connected from over 3000 km away in Fairbanks, Alaska. The satellite communication system was a Hughes 9502 Fixed Satellite Terminal produced by Ground Control Global Communication out of California. The system consists of the satellite terminal, the satellite dish, an Ethernet module, and an Ethernet cable. An Ethernet Module attached to the DA system relayed the raw data to the satellite terminal through the

Ethernet cable. The satellite terminal had a unique IP Address and transmitted data through the satellite dish that was fixed to the top of the pole above the solar panel as shown in Figure 4.20.

The DA system used a Campbell Scientific CR3000 Micrologger, shown in Figure 4.21, which was the same DA system used for the initial 2008 monitoring. There was inadequate wiring space on the CR3000, and multiplexers were used to provide the space required to connect all of the instrumentation signal cables to the DA system. Three AM16/32B multiplexers, shown in Figure 4.21 and Figure 4.22, were used to accommodate signal cables from the thermistors and piezometers. A vibrating wire piezometer interface, shown in Figure 4.21, was a necessary intermediary between the multiplexer and the CR3000 for the vibrating wire piezometers. Measurand provided their own multiplexer, shown in Figure 4.22, to connect the SAA signal cables to the DA system.

Solar energy provided power to the DA system as the project site was unconnected to the electrical power grid. The original set up consisted of a 30-Watt solar panel (shown in Figure 4.20), a battery, and a solar regulator. The solar regulator controlled the amount of power received by the generic 15-volt battery; both are shown in Figure 4.22.

Staff at RST Instruments provided the wiring schematic to appropriately connect the signal cables from the instrumentation to the DA system. Figure 4.20 shows the author connecting the signal cables to the DA system according to the wiring schematic included in the Appendix.

The code used by the DA system in the initial 2008 monitoring program was re-written by staff at RST Instruments to accommodate the additional instruments installed in 2012. The code programmed the DA system to first take readings from the thermistors and piezometers followed by a separate code prompting the DA system to take readings from the SAAs. The

author could modify the code to alter the monitoring schedule based on the desired frequency of data collection. Files containing the code can be found in the Appendix. The current monitoring schedule took readings for all instrumentation every five days at noon which were then downloaded by the author. Manitoba Infrastructure and Transportation (MIT) will continue to download the data from the site when the author's involvement in this research is finished.

The readings of the thermistors and piezometers were included in the same raw data file, and can be readily opened in an Excel spreadsheet. A separate raw data file contained the SAA readings because the SAA code was independent of the code used for the thermistors and piezometers. SAA Suite, a software package created by Measurand, converted the raw SAA data into useable data which could then be exported into an Excel spreadsheet. Modifications to the code, such as altering the monitoring schedule, created a new and separate data file. All subsequent readings were appended to the same data file. For example, if a monitoring schedule was changed from taking readings every five days to every ten days, and then back to every five days, there would be three separate data files. The author concatenated the separate data files from each code modification into a single data file containing all readings.

Communication problems first emerged during the 2012-13 winter. Concerns related to communication with the DA system during winter included: cold temperatures, snow covering the solar panels, fewer sunlight hours, and less direct sunlight. Heavy cloud cover and precipitation could also hinder access throughout the year as satellite coverage at the latitude of the project site is sparser than further south.

Communication was lost in November 2012 and the author twice returned to the project site before the end of the year. On the first visit from November 30 to December 1, 2012, the author determined that a thin layer of fluffy snow covering the solar panel had killed the battery.

The author replaced the battery, and attached a plastic awning to the pole as an attempt to shield the solar panel from snow, as shown in Figure 4.23.

The next communication breakdown occurred two days after the site visit. Unknown sources pinged the same IP address as the satellite system in the middle of the night and drained the battery. Though it was a unique IP address, it was not private. The solar panel was unable to recharge the battery because the pings draining its power occurred during the night. The author returned to the site from December 16 to 17, 2012 to replace the battery, upgrade the solar regulator to the more robust SunSaver Solar Controller model, and upload a new code to the DA system. The code was re-written so that the whole system was only operational during peak sunlight hours between 10 am and 2 pm. The system was offline outside those hours to prevent the battery from being drained in the middle of the night.

Communication was lost again two days after the second visit. On January 17, 2013, an engineer from the Thompson MIT office visited the site to manually download data. Despite of the addition of the plastic awning, there was still significant snow cover on the solar panel, as shown in Figure 4.24. The next visit occurred between from March 23 and 26, 2013. A second solar panel was added for redundancy as shown in Figure 4.25. Both solar panels were tilted to nearly vertical angles to reduce the chances of heavy snow accumulation. The battery was replaced for the final time with a larger 15-volt AGM battery that was more appropriate for extreme cold temperatures. A relay switch was also installed to physically disconnect the battery from the satellite terminal during offline hours. The housing box was re-arranged to accommodate the larger battery, the relay switch, and the new solar regulator as shown in Figure 4.26.

Communication continued unimpeded for the entire summer and fall of 2013 but was lost again during the winter of 2013-14 before resuming briefly in March 2014. The author surmised a faulty relay switch contributed to the latest communication disruption. An engineer from the Thompson MIT office replaced the relay switch at the site on May 16, 2014, and communication has resumed uninterrupted since that time.

In the future, other measures could be taken to improve the durability of the system during the winter months including insulating the housing boxes containing the DA system, and replacing the CR3000 Micrologger with a CR1000 Micrologger. The CR3000, though durable, is a portable unit while the CR1000 is intended for long term monitoring and has a larger range of temperature tolerance.

4.5   Data from Field Instrumentation

The following section discusses data collected since monitoring of the instrumentation resumed in September 2012. Ground temperatures, ground water conditions, and movements both vertically and laterally are presented. Data were collected every five days, but plots only present data in monthly intervals to reduce clutter. The Appendix contains all collected data.

4.5.1   Ground Temperatures

Thermistor strings at the toe, mid slope, shoulder, and centreline of the embankment provided ground temperature data since September 2012. Additional ground temperature data were available for the toe and mid slope from the original monitoring program between October 2008 and April 2011. The piezometers and SAAs measured temperatures less precisely than the thermistor strings. Therefore, this section only discusses data collected by the thermistor strings.

Figure 4.27 and Figure 4.28 show the annual maximum, minimum, and average temperature profiles for every 12-month interval since data collection began. The average temperature was calculated as a weighted average based on the interval of time between readings because communication interruptions discussed in Section 4.4 Data Acquisition System prevented a consistent time interval between readings. Temperature profiles of four freeze-thaw cycles are shown in in Figure 4.27 for the toe and mid slope, and two cycles are shown for the shoulder and centreline in Figure 4.28.

The difference between the annual maximum, minimum, and average temperatures shrinks with increasing depth from the ground surface. The difference in temperature converges to zero at the depth of mean zero annual amplitude, DMZAA. Ground temperatures below the DMZAA are not influenced by surface temperatures (Andersland and Ladanyi, 2004). The temperature at the DMZAA was 1.2°C warmer at the toe than at the mid slope even though the depth was 8 to 9 m below the ground surface at both locations. Sub-zero average temperatures have been observed at certain depths at the shoulder and centreline. Figure 4.28a indicates 3 to 4 m of sub-zero temperatures at the shoulder beginning at a depth of 6 m. Figure 4.28b indicates 6 to 7 m of sub-zero temperatures at the centreline beginning at a depth of 3 m. The average temperatures fluctuated very little in the sub-zero temperature region beneath the centreline and the shoulder. The term 'cryo' is used to describe often used to describe ground-ice or permafrost terms when sub-zero temperatures are observed but frozen ground is not (Harris, 1988). Water can remain unfrozen in fine grained soils in sub-zero temperatures because the soil particles have large surface areas in proportion to their size. A region of frozen ground that is more or less symmetrical under infrastructure is referred to as a frost bulb while it could be referred to as a cryo-bulb if only sub-zero temperatures are observed. Frozen ground was observed during

82

drilling so for the duration of this thesis, the region of sub-zero temperatures beneath the embankment is referred to as the frost bulb

Figure 4.29 shows a cross section comprising the temperature profiles of the instrumented half of the embankment. The frost bulb beneath the embankment is shown as the dashed blue region in the foreground while sub-surface materials are shown in the background. The frost bulb is vulnerable to thawing because of temperature changes at the ground surface and by the geothermal gradient from below. The positive average ground temperatures at the toe and mid slope indicated annual heat flux into the soil which is consistent with findings mentioned in Chapter 2 that stated permafrost thawing under embankments begins at the toe and spreads to the centreline (Alfaro et al, 2009) (Andersland and Ladanyi, 2004).

The existence of the frost bulb was predicted during the initial temperature monitoring at the toe and mid slope by Batenipour et al. (2010) and also by the numerical model developed by Kurz et al (2012b). The numerical model assumed constant temperature boundary conditions applied to specified points and lines under the embankment (Kurz et al., 2012b). The boundary conditions implied colder temperatures would be found under the centre of the embankment.

Figure 4.30 and Figure 4.31 show changes in ground temperatures plotted against time. Please note the different temperature scales used for each plot. Air temperatures exerted greater influence on the thermistor strings at the toe and mid slope, resulting in higher maximum temperatures because their shallowest nodes were much closer to the ground surface compared to the shoulder and centreline. Concurrently, the centreline and shoulder experienced lower minimum temperatures than the mid slope and toe. The contrasting temperatures reflect the difference in thermal conductivity between the gravel fill on the road surface and the silty clay along the embankment slope. Highway maintenance clears the road surface of snow in the

winter. Consequently, cold temperatures potentially penetrate deeper and more rapidly through the road surface. Snow is an excellent insulator and retains warm summer temperatures longer into the winter. The snow cleared from the road accumulates at the toe of the embankment and contributes to the initiation of permafrost degradation.

Ground temperatures experience a yearly freeze-thaw cycle. Air temperatures fluctuate with the seasons and directly impact the ground temperatures above the DMZAA even if the effect is not immediate. Ground temperature changes appear time-delayed compared to air temperature changes. The rate and magnitude of change depends on the depth and thermal conductivity of the material. Consequently, temperature changes are less pronounced and occur more slowly with increasing depth. The warmest ground temperatures were observed in late August to early October following a summer of warm air temperatures. The coldest temperatures were observed close to the end of April after the winter freeze. Ground warming resumed at the ground surface at the end of April to mark the beginning of another freeze-thaw cycle. The time-delayed ground temperature response to changes in air temperatures is clearly evident at the mid slope in Figure 4.30b. The maximum and minimum ground temperatures occur later in the year with increasing depth below the ground surface. The amplitude in temperature, of the freeze-thaw cycle, decreases with depth until the difference between the maximum and minimum temperature converges to zero at the DMZAA.

As previously stated in Chapter 2, permafrost is ground that remains at a temperature at or below 0°C for two or more consecutive years. Sub-zero temperatures were consistently observed at the same depths at the shoulder and centreline as the frost bulb region from September 2012 until the summer of 2014 as shown in Figure 4.31. The frost bulb experienced sub-zero temperatures long enough to be classified as permafrost. Despite the extremely cold

winter of 2013-14, thermistor strings at all depths, including the frost bulb region, recorded temperatures above 0°C at the end of the 2014 summer. The frost bulb should now be considered degrading permafrost because the warm temperatures may result in thawing. The frost bulb returned to sub-zero temperatures in the most recent temperatures readings from December 2014 and January 2014. Continued temperature monitoring through another freeze-thaw cycle are required to determine whether the sub-zero temperatures in the frost bulb region will remain.

4.5.2 Ground Water Conditions

Pore water pressure readings have been collected since September 2012 from vibrating wire piezometers installed at 4 m intervals at the toe and centreline of the embankment. The piezometers at the toe also included pore water pressure readings between October 2008 and April 2011 as part of the initial monitoring program. Total head calculations used the elevation at the toe of the embankment as the datum.

Figure 4.32 shows quarterly pore water measurements plotted against depth with the hydrostatic water pressure shown as a reference. The data demonstrates the seasonal variations of pore water pressures under the embankment. The variation is more evident in a plot of the total hydraulic head versus time (indicated by the date) shown in Figure 4.33. Observations about the seasonal changes in ground water conditions can be made with greater certainty at the toe than the centreline due the longer period of monitoring.

Figure 4.33a shows ground water conditions under the toe of the embankment. Ground water conditions appear to be largely hydrostatic in the summer while upward gradients develop in the winter. The freezing front moves downwards in the winter as ground temperatures decrease. The ensuing negative potential at the freezing front may create suction pressure that induces an upward gradient to draw up water from lower depths. The upward gradient can

decrease the effective stress and therefore decrease confining stress and shear resistance of the foundation soil.

Ground water conditions at the centreline are shown in Figure 4.33b. The piezometers at 13.2 m and 17.5 m depth are located below the frost bulb. Total heads decrease in the winter and increase in the summer, but the variability between seasons is slight. The total heads indicate a downward gradient leading to an underlying aquifer in a region of fractured rock or gravel just above intact bedrock. The downward gradient increases the effective stress in the clay under the embankment and may lead to consolidation. The piezometer at 9.2 m depth is located in the frost bulb while the piezometer 5.2 m depth is just above the frost bulb in gravel. Neither piezometer exhibits cyclic behaviour related to different parts of the year. The pore water pressure changes of the piezometer at 5.2 m depth are especially erratic. It is possible the pressure exerted on the diaphragms of the piezometers by the frozen ground could render the readings unreliable.

4.5.3 Ground Movements

The following two sections present the results and analysis of the vertical and lateral movements based on data collected since September 2012. ShapeAccelArrays (SAAs) were installed vertically at the shoulder to measure lateral deformations and horizontally between the toe and centreline to measure vertical deformations. The SAA must be anchored at one end to serve as a reference point for the displacement readings as explained in Section 4.2.3 Displacement. The first SAA displacement reading is zero and all subsequent displacements are relative to the first reading.

4.5.3.1 Lateral Movement

Figure 4.34 shows the quarterly cumulative measured lateral deformation of the SAA installed vertically at the shoulder and anchored in the bedrock at a depth of 20 m. The sub-surface layers are shown in the background in different colours; orange represents the gravel fill, yellow represents the silty clay, and the bedrock is grey. The frost bulb is approximated by the dashed blue region. Positive displacements indicate deformations away from the centreline of the embankment.

Inward lateral deformations towards the centre of the embankment occurred in the 6 m thick gravel layer with a maximum value of 80 mm. Outward lateral deformations away from the centreline develop between depths 3.5 and 4 m, the approximate boundary between the gravel fill and the silty clay. The SAA recorded the maximum outward deformation of 120 mm inside the frost bulb at a depth of 6.5 m. No significant lateral deformations were observed below the depth of 8.5 at the base of the frost bulb likely due to the less compressible mechanical properties of frozen ground mentioned in Chapter 2. The cumulative deformation increased steadily over the entire monitoring period, except for the sudden spike occurring each fall. The cumulative displacement increase between October and the very next reading in winter surpassed the largest displacement between any other two consecutive readings shown in Figure 4.34. The timing coincided with the warmest ground temperatures observed in Section 4.5.1 Ground Temperatures when the soils would be considered their weakest because of the loss of strength from thawing.

The lateral deformations at the shoulder were consistent with the lateral deformations observed at the toe by a slope inclinometer during the initial monitoring period shown in Figure 4.35 (Batenipour et al., 2011). The deformations at the shoulder were more pronounced than at the toe, but the general shape was similar. The slope inclinometer also observed inward lateral

movements to a depth of 4 m. The maximum outward deformation occurred at a depth of 8 m and no lateral deformation was observed below 11 m. Maintenance of the road would place fill loading at the shoulder and cause greater movements than at the toe. Thaw consolidation would have also occurred earlier at the toe than at the shoulder possibly explaining greater current changes in deformations (Alfaro et al, 2009) (Andersland and Ladanyi, 2004).

4.5.3.2 Vertical Movement

Figure 4.36 shows the vertical deformation recorded by the second SAA anchored at the toe and installed horizontally 16 m into the embankment. The plot shows the approximate locations of the toe, mid slope, shoulder, and centreline under the embankment. The general trend shows increasing downward deformation since installation in September 2012. As stated in Section 4.3 Armouring and Installation, the anchored end of the SAA was modified twice to ensure it was fixed in position. There was no noticeable discrepancy in the deformation caused by modifications to the anchored end of the SAA.

A maximum deformation of 304 mm was observed just beyond the centreline translating to approximately 150 mm for each year of observation. The magnitude of the displacement is large, and maintenance does apply and re-grade fresh gravel on the road surface each year. However the author was unable to compare the displacements with the amount of fill applied to the road as exact records of gravel application at this location were not kept. The deformation increased in the fall months when the ground temperatures reached their warmest values. The lateral movements behaved similarly.

Figure 4.37 shows the deformations over time at different locations under the embankment. Typically, frost heaves develop in the fall when the freezing front advances to lower depths and often form ice lenses. The subsequent spring thaw can melt the ice lenses

leading to reductions in shear strength and higher compressibility. However, this is not the behaviour that the SAA has observed. The plot shows downward deformation throughout the fall and winter at all four locations followed by a sudden upward spike over several weeks in the spring. In the summer, there was negligible movement at toe and mid slope. Concurrently, downward movement resumed at the shoulder and centreline at the same rate as in the fall and winter. The annual net movement at the toe is essentially zero since the upward spike in the spring nearly recovers all cumulative downward movement from the fall and winter. The largest deformations occur in the SAA segments closest to the centreline. Similarly, surface settlement plates positioned closer to the centreline observed the largest deformations during the initial monitoring period (Batenipour et al., 2010).

There was concern that the upward spike during the first spring was related to an improperly secured anchor point. This led to the installation of the 8-foot (2.4 m) ground anchor in November 2013. There were no sudden changes in displacement readings before or after installation, so the author determined the anchor point had been adequately secured. Even so, the upward spike occurred again in the spring of 2014. Between April 15, 2013 and June 14, 2013, 53 to 56 mm of upward movement was observed while 38 to 42 mm of upward movement was observed between April 15, 2014 and May 15, 2014. Figure 4.37 shows the upward spike in movement coincided with the stretch of time that groundwater conditions at the toe changed from an upward gradient in the winter to hydrostatic conditions in the summer. Pore water pressures at the toe increased at the same time each year as well. There was essentially no movement at the toe or mid slope during the hydrostatic summer groundwater conditions. Downward movement at the toe and mid slope resumed at the same time the upward gradients developed at the toe. Movement resumed in the fall because the upward gradient reduced the

effective stress of the soil. Consequently the reduced effective stressed resulted in decreased confining stress and shear resistance.

The author proposes that the upward spike was related to expansion of the clay layer under the embankment. In the spring, thawing could have caused meltwater from the frost bulb region to accumulate in the clay region. Water cannot easily escape through the impervious still-frozen soil (Konrad and Roy, 2000). Consequently, Konrad and Roy (2000) observed that the increased water content during thawing caused the soil under the still-frozen soil to swell. The swelling depended on the quantity of meltwater, the swelling index of the subgrade, and the volume of the subgrade (Konrad and Roy, 2000). Clay is commonly used in dikes because its low hydraulic conductivity greatly reduces the amount of water that seeps through the dike. The low hydraulic conductivity of clay suggests the accumulated water under the embankment dissipates very slowly. The clay would begin to expand because the combination of meltwater and the upward gradient would exceed the lateral drainage capacity of the clay. Impeded drainage and subgrade swelling in Quebec lasted between 3 and 6 weeks (Konrad and Roy, 2000). The expanding clay pushed the PR 391 embankment up for 4 to 8 weeks until hydrostatic groundwater conditions were achieved. Lateral drainage was now sufficient since there was no longer an upward gradient.

The winter of 2013-14 was colder than normal (Environment Canada, 2014) and could explain the shorter time period and smaller upward movement compared to the previous year. Further work could be done to determine if drainage in the embankment could alleviate, at least partially, the settlement issues. Work could also be done to examine the groundwater flow from one side of the embankment to the other side.

4.6 Summary

The author established a new monitoring program to remotely collect data at the PR 391 highway embankment project site. The zone of monitoring was expanded after Manitoba Infrastructure and Transportation gave permission to install instruments under the road surface which was not previously permitted. Instrumentation included eight (8) new instruments installed in September 2012 and four (4) instruments installed in October 2008 during the initial monitoring program. The author installed thermistor strings at the centreline and shoulder in addition to existing thermistor strings at the mid slope and toe to monitor ground temperature. Four (4) vibrating wire (VW) piezometers were installed in 4 m intervals centreline to complement the two (2) existing VW piezometers at the toe to measure pore water pressure. ShapeAccelArrays were installed vertically at the shoulder and horizontally between the toe and the centreline to measure lateral and vertical displacement respectively.

Data were collected remotely every 5 days after September 2012 using a satellite system. The data acquisition (DA) system was powered by solar energy as it was located off the electrical grid. The DA system continues to operate after addressing communication issues caused by the extreme weather conditions at the site.

The existence of a frost bulb under the embankment was confirmed after sub-zero ground temperatures were recorded every month since September 2012 under the shoulder and centreline of the embankment at the same depths encountered during the drilling. The frost bulb was found between depths 7 to 9 m under the shoulder and between depths 3 to 10 m under the centreline. The warmest temperatures under the embankment were observed at the toe which is consistent with previous research stating permafrost degradation of embankments began at the

toe (Alfaro et al, 2009) (Andersland and Ladanyi, 2004). All thermistors recorded above-zero temperatures for the first time in the fall of 2014 which indicates degrading permafrost.

There was a small downward hydraulic gradient observed at the centreline possibly leading to an underlying aquifer in a region of fractured rock or gravel just above the intact bedrock. An upward gradient developed at the toe in the fall, likely due to suction pressure caused by the downward migration of the freezing front.

At the shoulder, inward lateral movements have been recorded in the gravel layer, and outward in the underlying clay before it was restricted by the frost bulb. The shape of lateral deformations was consistent with the slope inclinometer data at the toe from the initial monitoring program. The magnitude of movement was greater at the shoulder than the toe, suggesting permafrost degradation was progressing from the toe.

Continuous downward movements have been recorded under the embankment. Thawed soils are more compressible than frozen ground and the greatest vertical deformation was observed in the fall when ground temperatures are the warmest. An upward spike of vertical movement has been observed in two consecutive springs. At the same time of year, the upward ground water flow during the winter transitioned to hydrostatic conditions in the summer. The author proposed that the upward gradient and meltwater from the bottom of the frost bulb caused water to accumulate in the underlying clay layer similar to observations made in Quebec (Konrad and Roy, 2000). Consequently, the clay expanded because of the increased water content and pushed the embankment up for several weeks.

The accumulation of snow at the toe of the embankment can encourage permafrost degradation because of its effectiveness as an insulator. Snow should be cleared along the embankment slope as far back as possible to prevent too much heat from being trapped at the toe

in order to slow the permafrost degradation. Controlling the drainage of water away from the embankment during the spring melt can prevent water from pooling along the embankment slope and contributing to the reduction in effective stresses, confining stresses, and shear resistance. Further work at the project site could involve monitoring instrumentation across the entire cross section.

Figure 4.1: Provincial Road 391 Project Site located 18km north of Thompson, Manitoba. Instrumented section marked by pylons along shoulder of the road in the centre of the photograph. September 25, 2012.
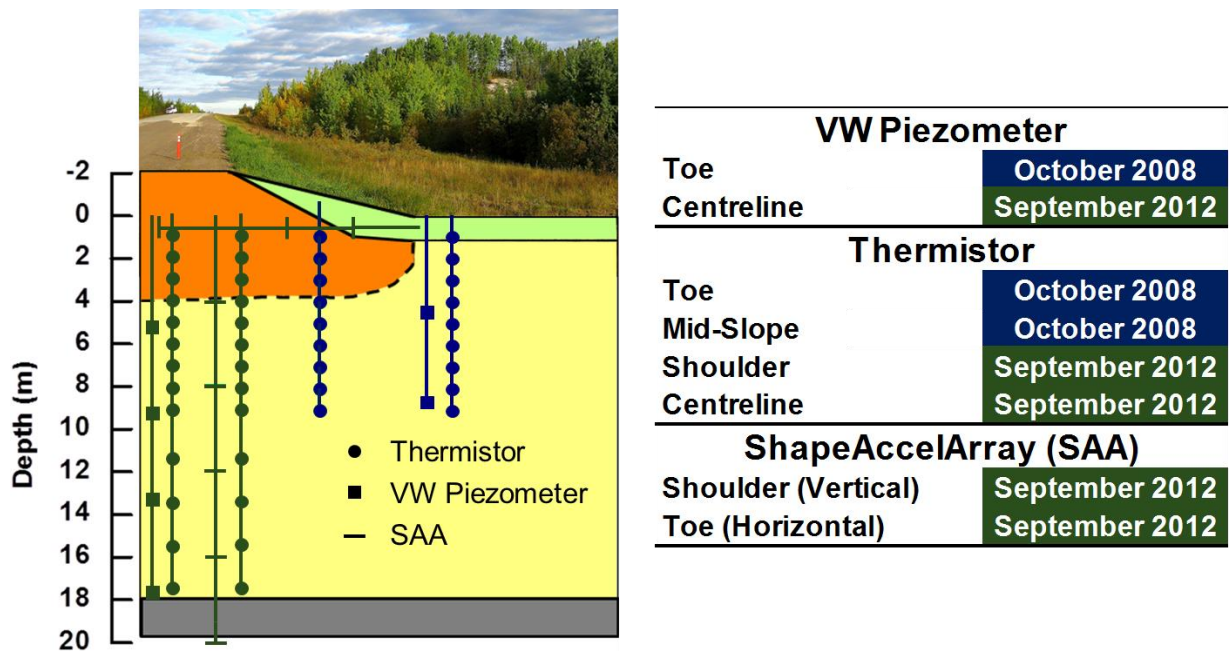
Figure 4.2: New instrumentation installed in 2012 (Green) and instrumentation installed in 2008 (Blue).

94

Figure 4.3: RST Thermistor ready for installation into the shoulder. Electrical tape was used to secure the thermistor nodes to the PVC pipe. September 12, 2012.

Figure 4.4: Multilevel Vibrating Wire Piezometer installed in the shoulder. September 24, 2012.

Figure 4.5: ShapeAccelArrays on their factory issued bundles. The white tape with the black dots indicates the direction of the x-axis. September 10, 2012.

Figure 4.6: Multilevel Vibrating Wire Piezometer prior to gluing the connections and installing vertically at the centreline. September, 14, 2012.

Figure 4.7: Installation of the 13-Point Thermistor 18m in length at the Shoulder on September 12, 2012.

Figure 4.8: Installation of the Multilevel Vibrating Wire Piezometer at the Centreline on September 24, 2012.

Figure 4.9: Installation of the vertical SAA at the shoulder into PVC pipe on September 15, 2012.

Figure 4.10: Horizontal drilling on September 13, 2012 at the toe of the embankment for the horizontal SAA installation.

Figure 4.11: Installation of the horizontal SAA at the toe into PVC pipe on September 13, 2012.

Figure 4.12: Installation of foot-long U-shaped piece of rebar as an anchor for the horizontal SAA installed at the toe. December 1, 2012.

Figure 4.13: (a) Installation of 8-foot (2.4 m) long ground anchor to (b) complement the existing anchor for the horizontal SAA installed at the toe on November 14, 2013.

Figure 4.14: Pulling the thermistor cable through PVC pipe for extra protection as it runs from the centreline to the DA box. September 13, 2012.

Figure 4.15: Gluing a connection for the PVC pipe protection of instrumentation cables at the shoulder. September 13, 2012.

Figure 4.16: Instrumentation cable protection at the shoulder. September 15, 2012.

Figure 4.17: Additional armouring of horizontal SAA at the toe and view of the trench dug for the cables in the PVC pipes from the shoulder of the embankment. September 15, 2012.

Figure 4.18: Trench dug to protect cables in the PVC pipe armouring to the DA Boxes. September 15, 2012.

Figure 4.19: Fitting final connections of PVC pipe that contain the instrumentation cables to the DA boxes. September 14, 2012.

Figure 4.20: Wiring the instrumentation into the data acquisition system. Top: Satellite. Middle: Solar Panel. Bottom: Housing for Data Acquisition System. September 16, 2012.

Figure 4.21: Housing containing (Clockwise from top left) multiplexers for the thermistors and VW piezometers (AM16/32B), vibrating wire Interface, CR3000 Micrologger, and Ethernet Module (middle on CR3000). September 16, 2012.

Figure 4.22: Original set up for left housing including (clockwise top left) communication array, original solar regulator, original battery, and multiplexers (SAA multiplexer on top and AM16/32B Multiplexer on bottom). September 16, 2012.

Figure 4.23: Plastic awning added to shield solar panel from snow. December 1, 2012.

Figure 4.24: Snow cover issues persisted after plastic awning added contributed to loss of batteries. January 17, 2013.

Figure 4.25: Second solar panel added and both solar panels tilted to a nearly vertical angle. March 27, 2013

Figure 4.26: Housing contained (clockwise from top left) the relay switch, communication array, new solar regulator, new 15-volt AGM battery, and multiplexers. March 27, 2013
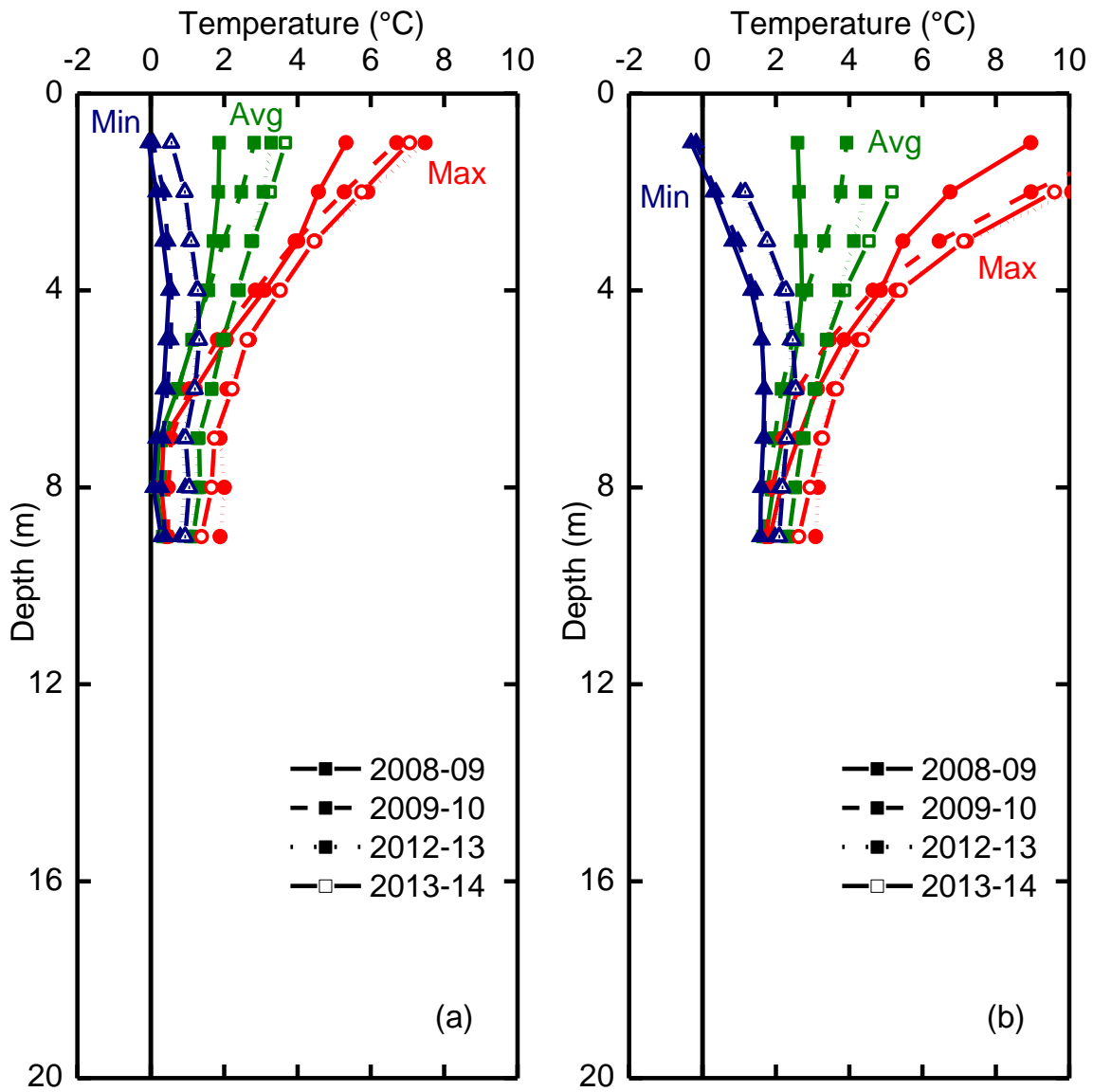
Figure 4.27. Temperature Profiles from October 2008 to September 2010, and from September 2012 to August 2014 for (a) the toe and (b) the mid slope
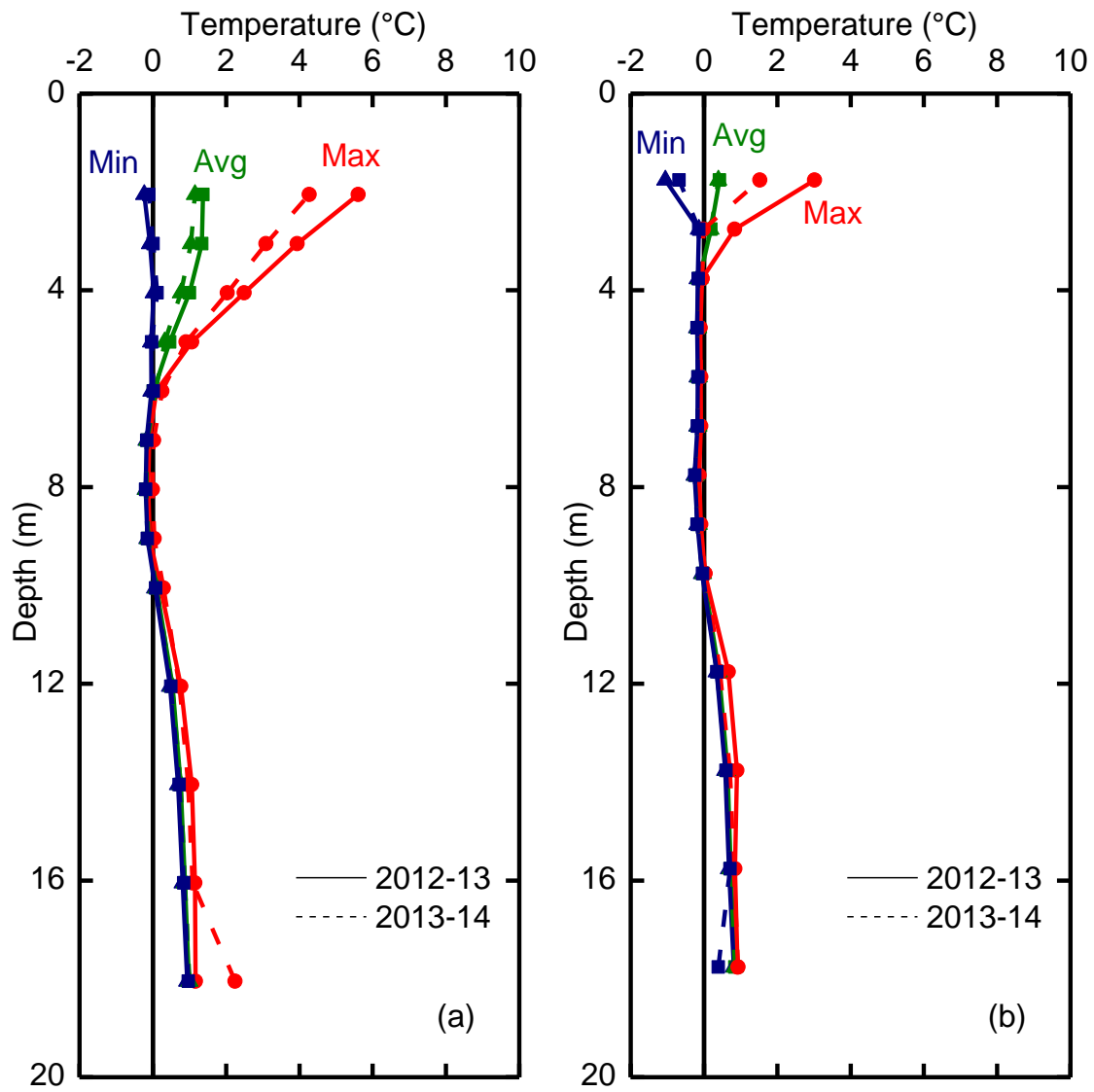
Figure 4.28. Temperature Profiles between September 2012 and August 2014 for (a) the Shoulder and (b) the Centreline
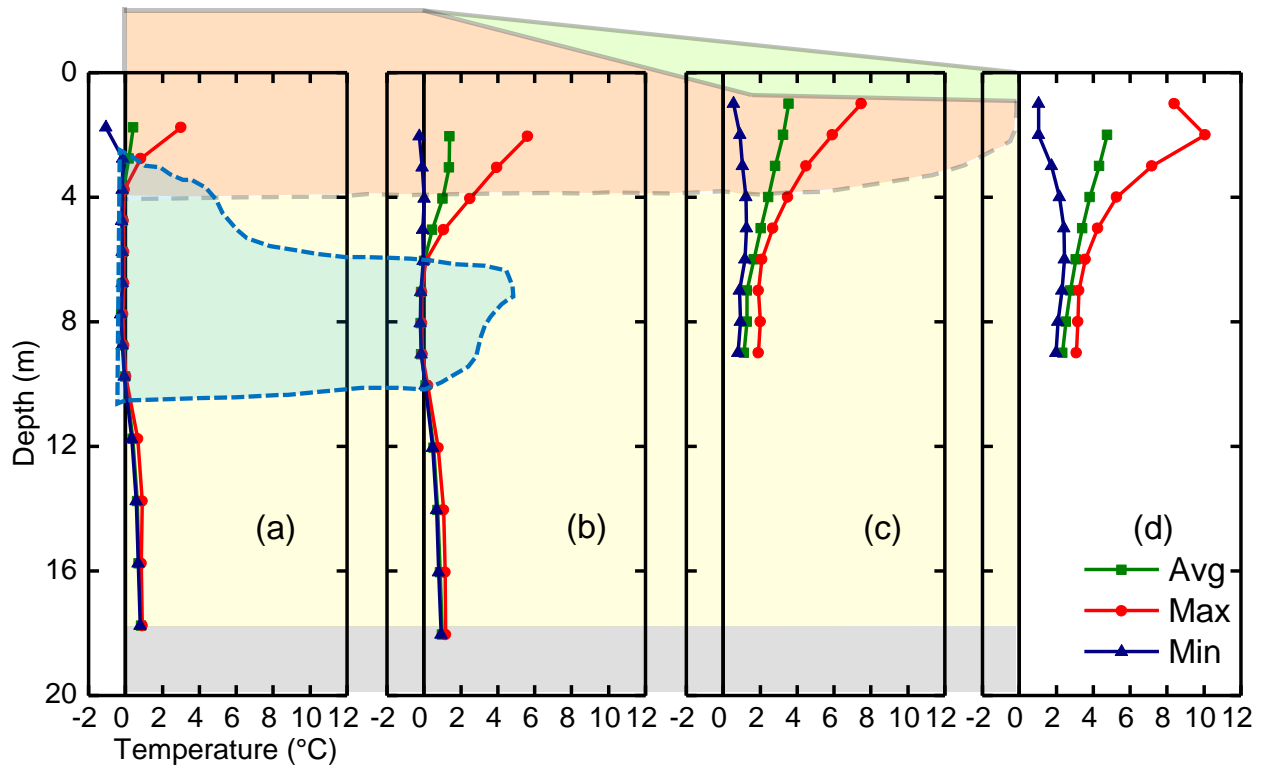
Figure 4.29: Approximate representation of frost bulb under the embankment based on weighted average, minimum, and maximum temperatures from 2012-2014.
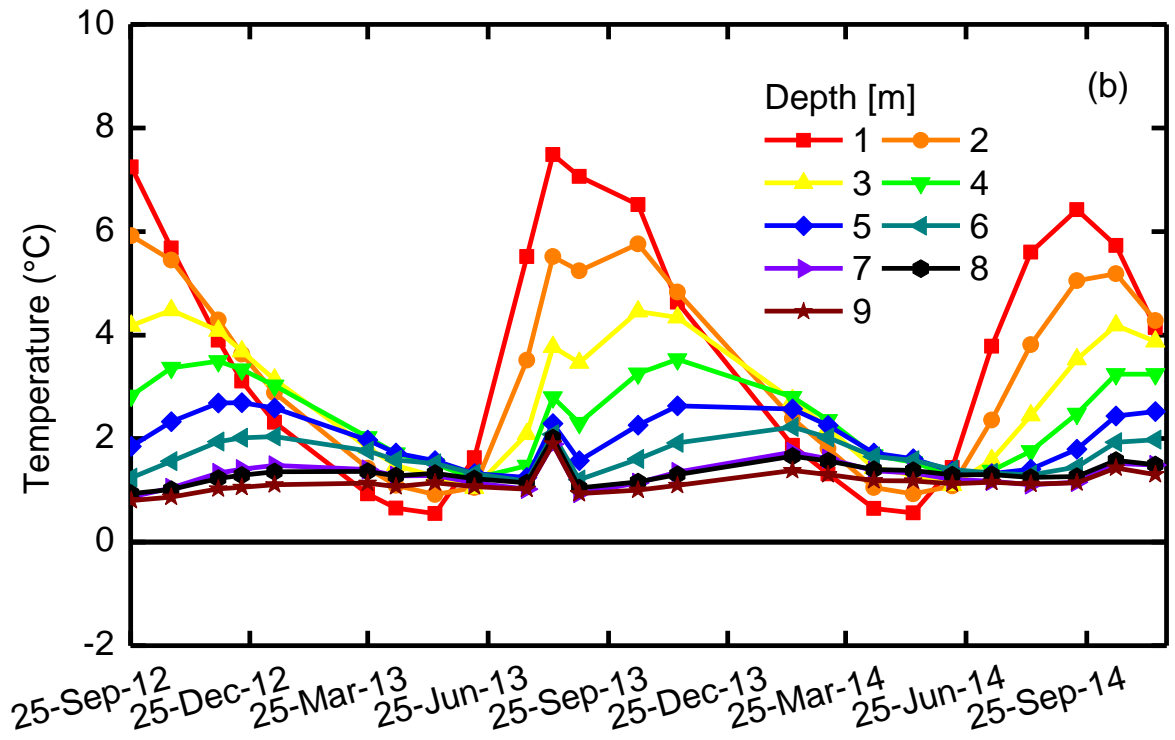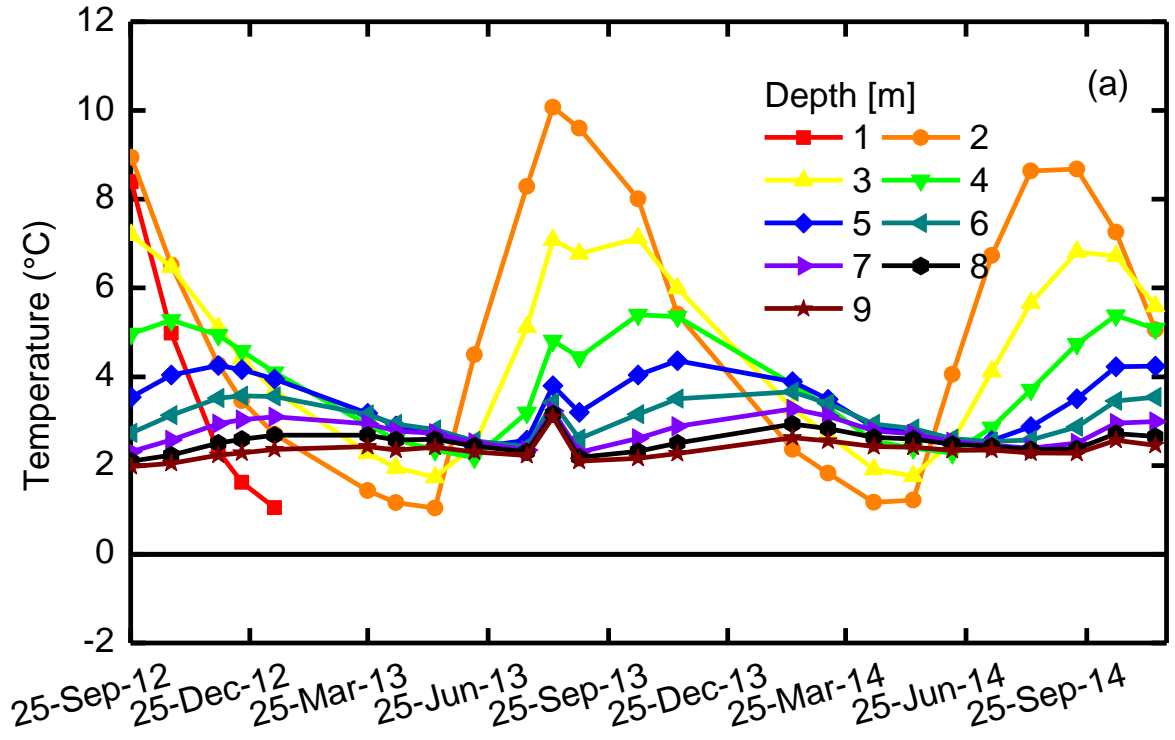
Figure 4.30: Temperature changes over time at different depths at (a) the toe and (b) the mid slope
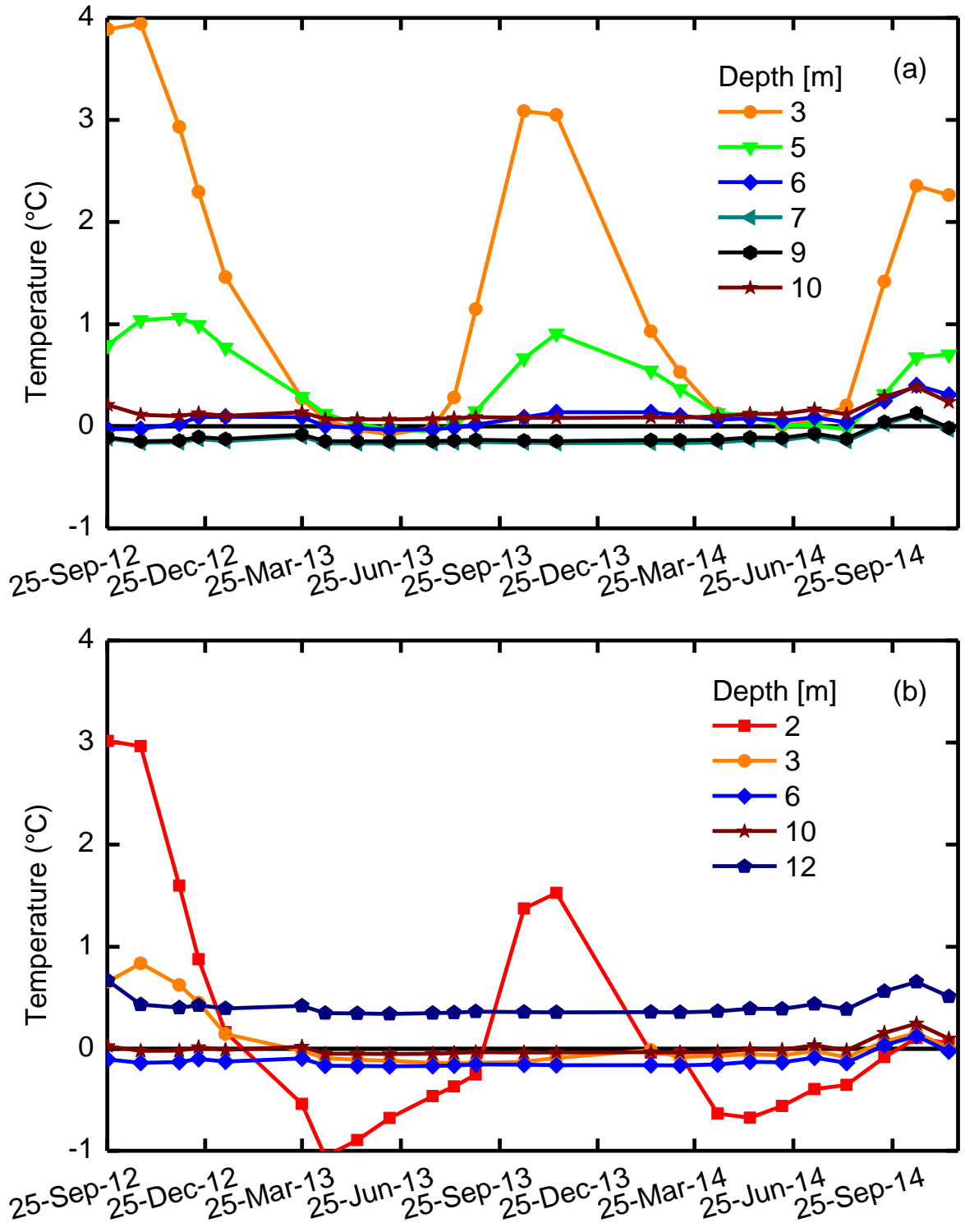
Figure 4.31: Temperature changes over time at different depths at (a) the shoulder and (b) the centreline
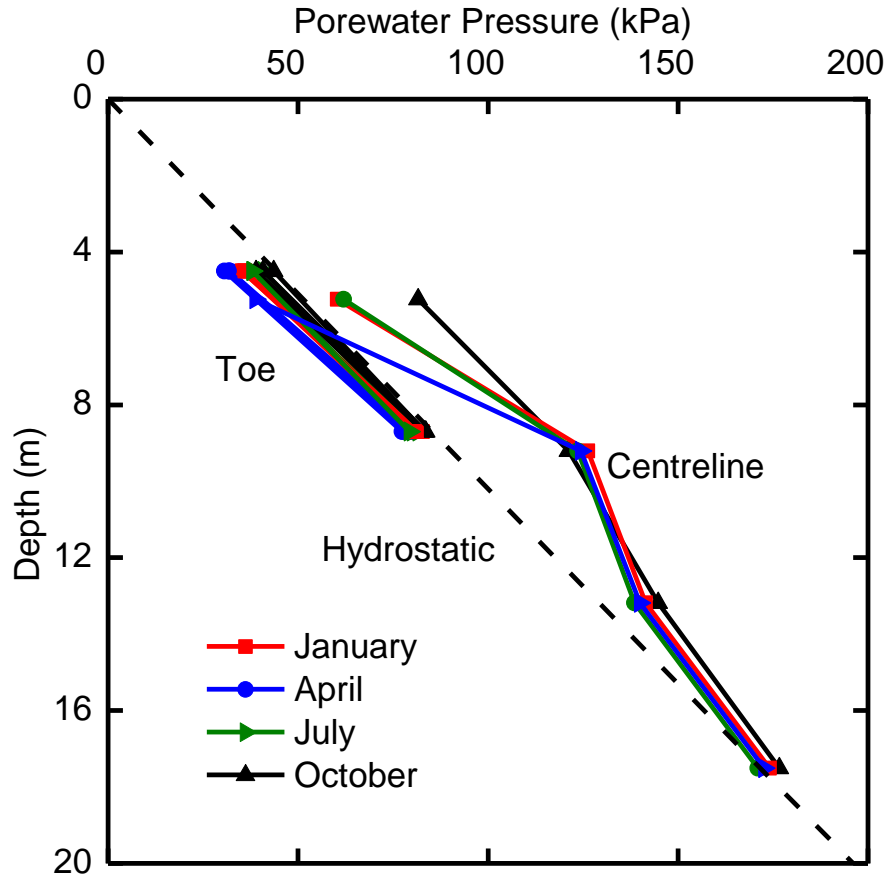
Figure 4.32. Quarterly Pore Water Pressure Readings at the Toe and Centreline
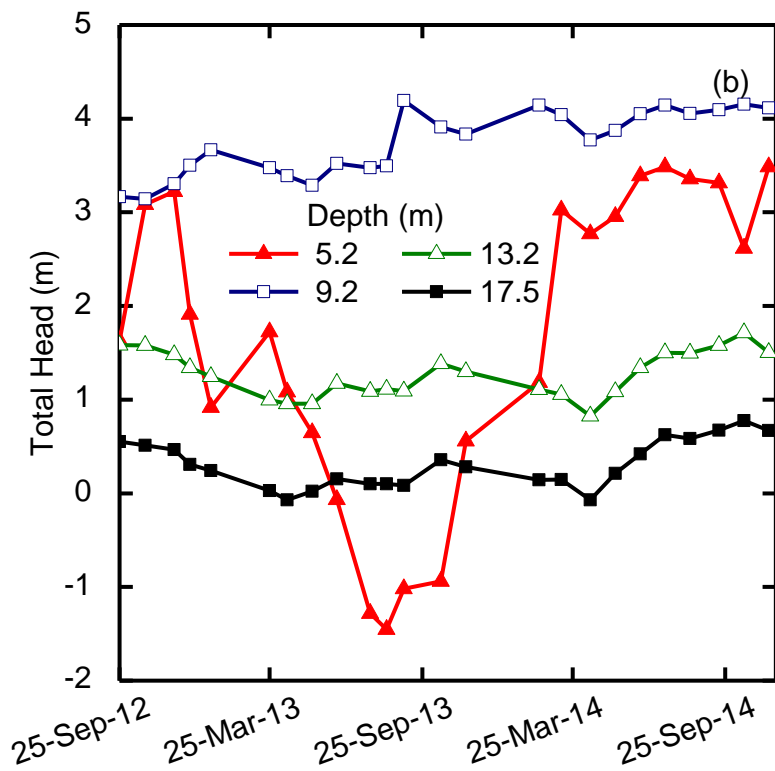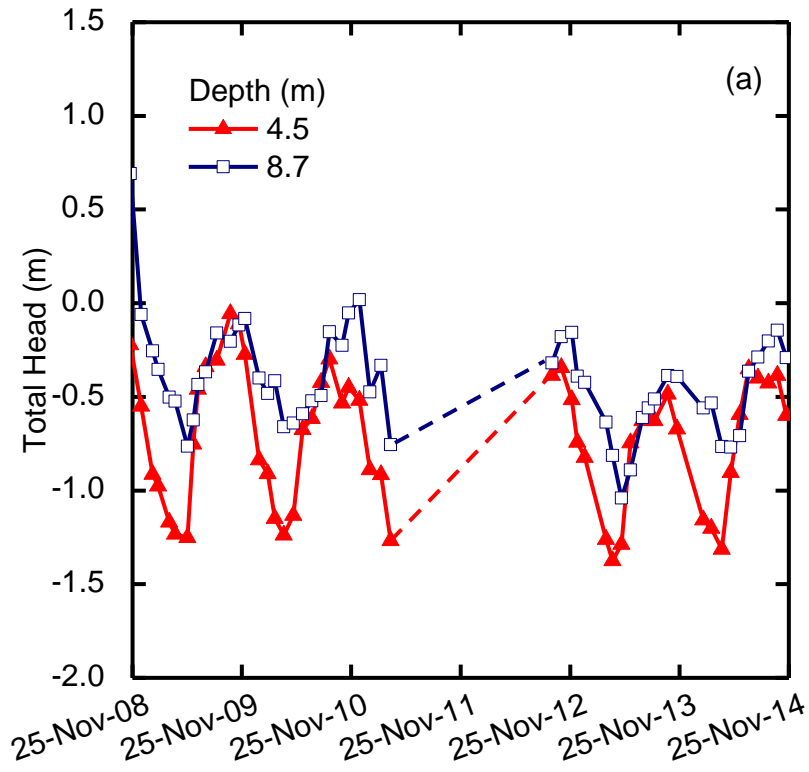
Figure 4.33. Total Head Measured at (a) the Toe and (b) the Centreline
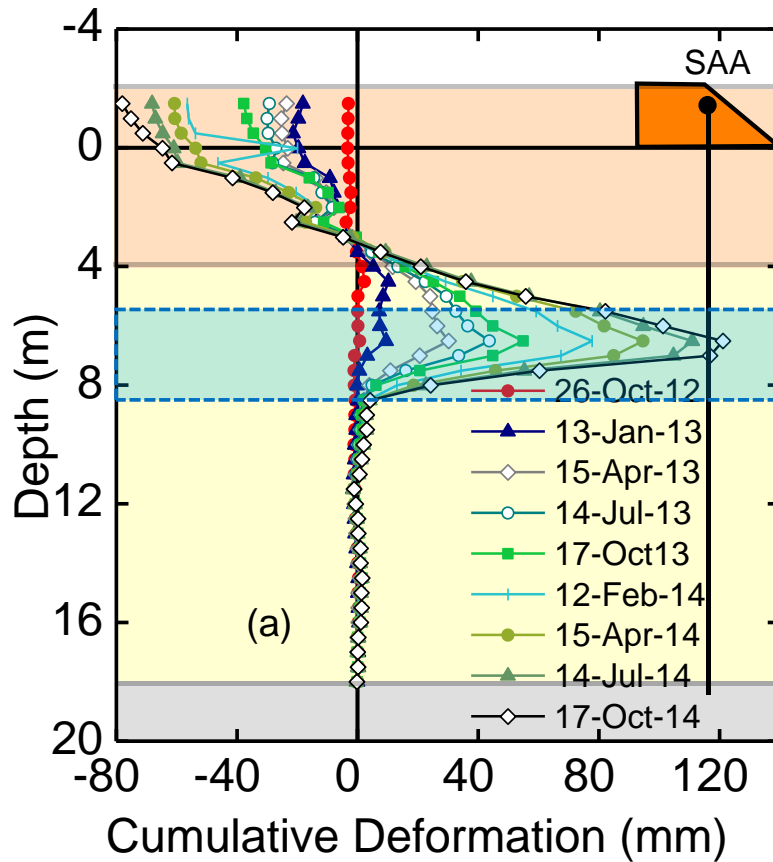
Figure 4.34. Lateral Movement at the Shoulder measured by the SAA. September 2012 to October 2014. Orange indicates gravel fill, yellow indicates silty clay, and grey indicates bedrocks. Sub-zero temperatures indicated by the blue region.
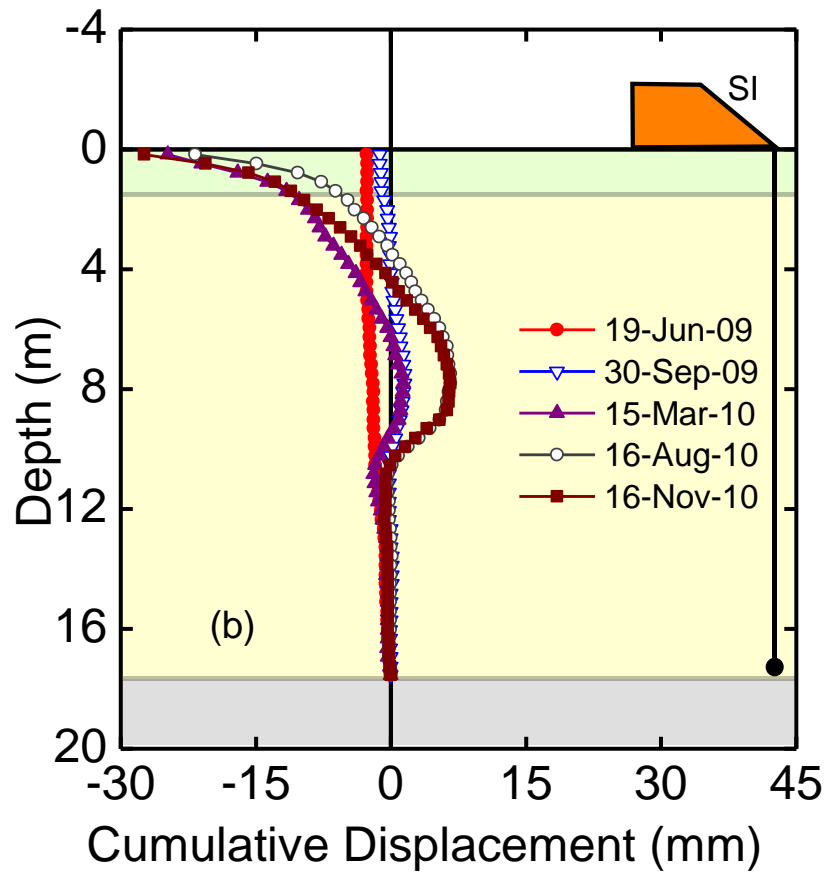
Figure 4.35: Lateral measurements at the toe measured between June 2009 and November 2010 by a slope inclinometer as part of the initial monitoring program. Sub-surface materials are shown in the background: the clayey silty berm with organics is green, the silty clay is yellow, and the bedrock is grey.
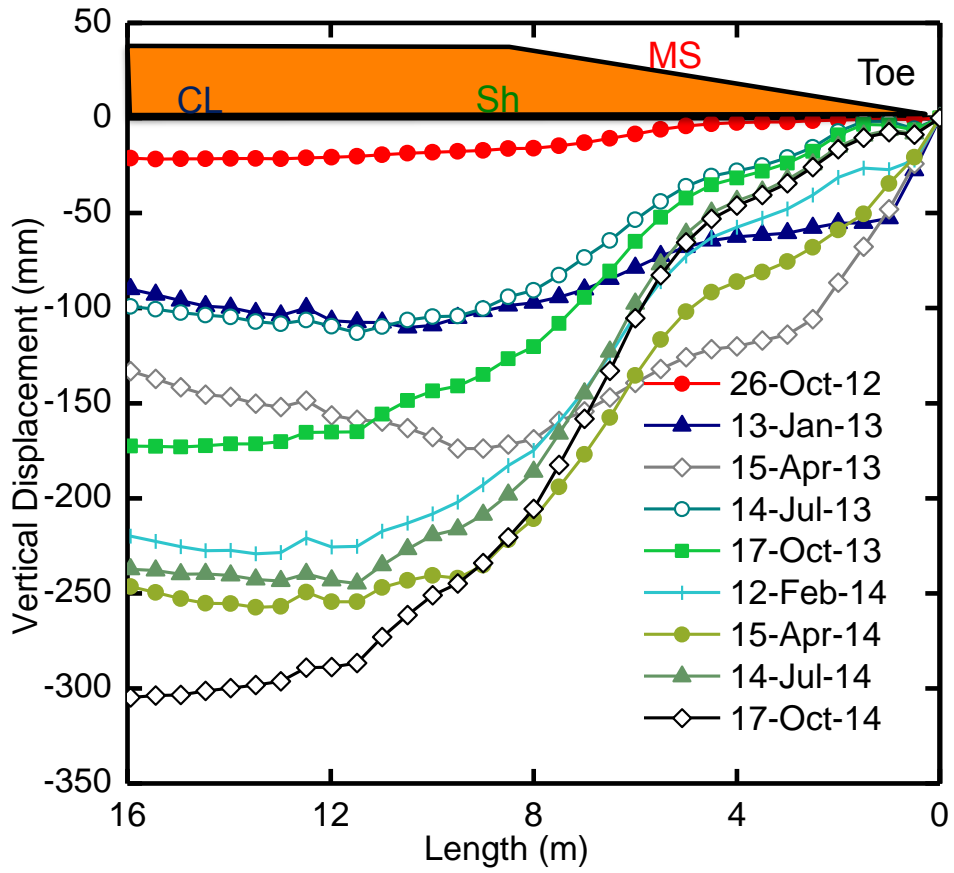
Figure 4.36: Vertical Displacement measured by the horizontal SAA. Labels refer to approximate locations of toe, mid slope, shoulder, and centreline of the embankment.
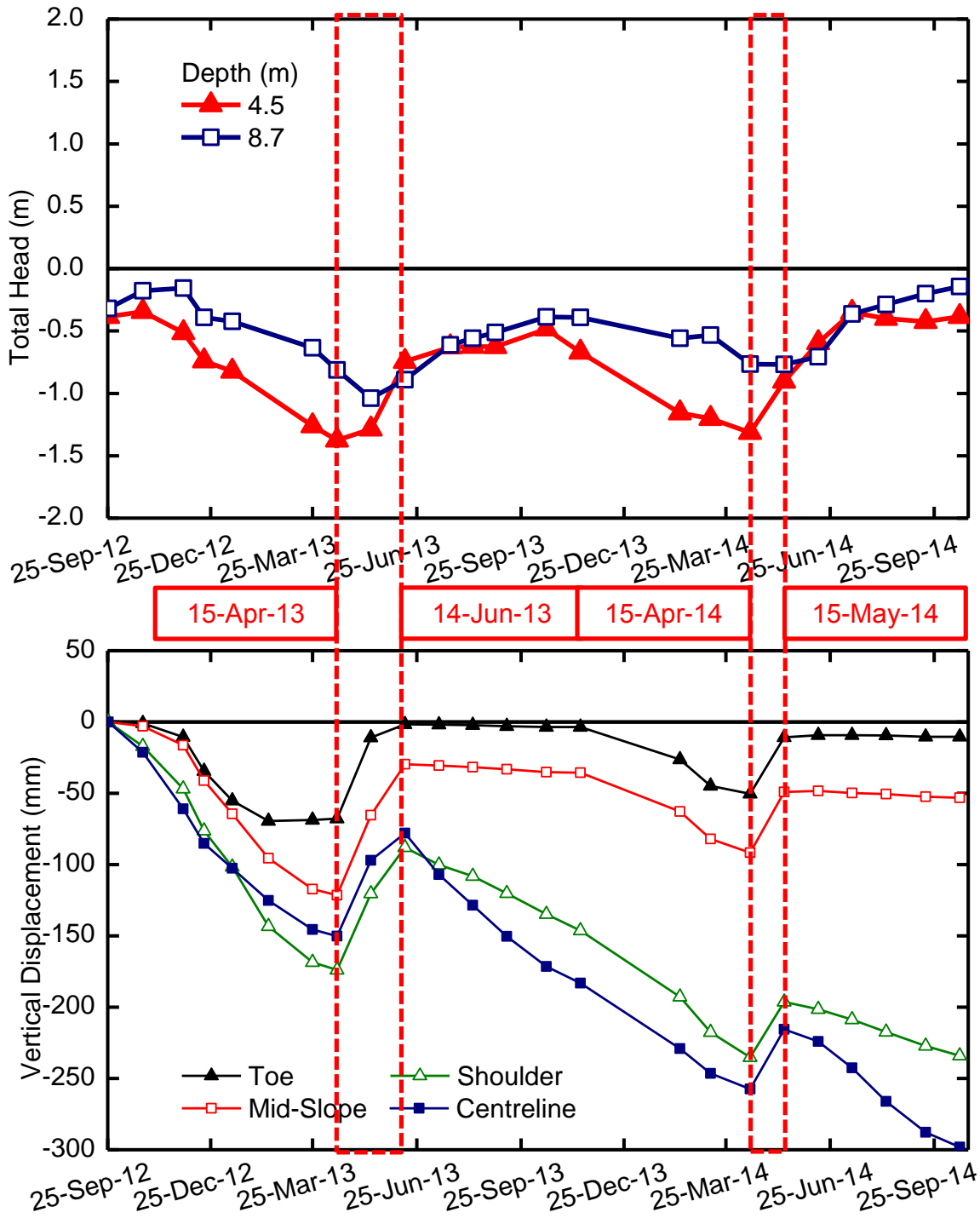
Figure 4.37: Total heads measured by the VW piezometer at the toe plotted on the same time scale as the vertical displacement measured by the the horizontal SAA at the toe. Dates are noted when upward movement occurs in the spring.

117

Chapter 5: Numerical Modelling

5.1 Introduction

The purpose of the numerical modelling was to replicate the conditions of the PR 391 embankment, enhance understanding of its current performance, and to make predictions about its future behaviour. A model in reasonable agreement with observed behaviour can lead to improved design and maintenance practices for road embankments subjected to degrading permafrost.

The modelling was done in two stages: thermal modelling and deformation modelling. A 2D plane strain model symmetrical around the centreline of the embankment was used for all models. The project site was along a straight 5 km long segment of highway so a 2D plane strain analysis was considered representative of the embankment. Variations in geometry and heterogeneity in the physical properties did exist along the highway, but the differences were not significant enough to warrant the additional input parameters, uncertainties, and computational power necessary to support the complexity of a 3D model compared to a 2D model. The increased uncertainty associated with an increased quantity of assumed values would be reflected in the 3D model results.

The author's thermal numerical models built upon previous model developed by Batenipour (2012) and Kurz (2013) to further understand the performance of the embankment at this location. Previous models only calibrated and validated the model with temperature data from the mid slope and the toe of the embankment. The author developed the thermal model with data from the toe, mid slope, shoulder, and centreline to provide an expanded view of the thermal regime under the embankment.

In a new contribution, the author also created a deformation numerical model to understand the movements in the embankment with changing thermal conditions. Previous numerical models at the project site only simulated the thermal regime; none had simulated the deformation behaviour. Displacement data recorded by the ShapeAccelArrays (SAAs) was used to calibrate and validate the deformation numerical model. To be clear, Ciro (2006) developed a deformation model for a road embankment as mentioned in Chapter 2. However, the simulated values in the Ciro (2006) model did not have measured displacement data for comparison. The following sections discuss the development of the numerical models and the ensuing results.

5.2   Thermal Model

The author developed the thermal model to simulate the ground thermal regime under the highway embankment at the PR 391 project site. The thermal model used the TEMP/W software package from Geo-Slope International Ltd. The following section includes the development of the thermal model, an analysis of results, comparisons to actual ground temperature data, and predictions about long term behaviour of the ground thermal regime.

5.2.1   Theory

TEMP/W is a finite element software used to simulate changes to the ground thermal regime in response to environmental changes or human activities, such as construction. The software simulates heat transfer through fully or partially saturated and fully or partially thawed material. TEMP/W analyzes a wide variety of inputs such as ground types under various water contents, thermal material properties, and thermal boundary conditions using an iterative numerical process until a solution is calculated (Geo-Slope, 2010b). There are three main parts to constructing a model: discretization, material properties, and boundary conditions.

Discretization, or meshing, is the process of dividing the user-created domain into smaller pieces called finite elements. A series of user-defined geometric objects shaped by spatial points, such as soil regions, circular openings, line objects, surface regions, and point objects, create the domain of the model. Default discretization creates a mesh that divides the geometric objects into finite elements that share nodes and edges with adjacent finite elements. Mesh properties can be specified so certain geometric objects have a finer mesh (a greater density of finite elements) or a different pattern of mesh elements (triangular or quadrilateral). The domain development of the author's thermal model is discussed in Section 5.2.2 Geometry.

It is crucial that material properties represent the site conditions to achieve a solution that accurately reflects the ground thermal regime. Five thermal material models are available in TEMP/W: no-thermal, interface, coupled convective thermal, simplified, and full thermal model. The no-thermal models are appropriate for regions not yet constructed like in staged construction. An interface model is useful for specifying thin insulating or no heat flow barriers. Though not performed by the author, it is possible to couple thermal models in TEMP/W with the SEEP/W module of the Geo-Slope software to account for the convective heat transfer contributed by moving water. In a coupled analysis, the material properties are further dependent on changes in temperature and water content. Material properties are only dependent on temperature in a simplified thermal model. A full thermal model requires temperature dependent functions for material properties using a fixed water content. The author's process for material model and property selection is described in Section 5.2.3 Material Properties.

Results from a numerical model are a direct response to the boundary conditions applied in the numerical model. At least one boundary condition must be specified at a node, line, or region in the model. In a thermal model, boundary conditions can be specified as either a

temperature or a heat flow (heat flux). The TEMP/W heat flux governing equation states that heat flow at a node is the product of the temperature and material properties as shown in Equation 5.1.

[Eq. 5.1] $q = -k\dfrac{\partial T}{\partial x}$

The heat flux, q, directly depends on the thermal conductivity, k, and the change of temperature, T, over a distance, x. The negative sign denotes that the direction of heat flow is from high energy (high temperature) to low energy (low temperature). TEMP/W assumes conduction is the primary means of soil heat flux (Harlan and Nixon, 1978) in the absence of seepage in a coupled model with SEEP/W. Equation 5.2 shows the differential equation that governs the formulation of 2D numerical solutions in TEMP/W.

[Eq. 5.2] $\dfrac{\partial}{\partial x}\left(k_x \dfrac{\partial T}{\partial x}\right) + \dfrac{\partial}{\partial y}\left(k_y \dfrac{\partial T}{\partial y}\right) + Q = \lambda \dfrac{\partial T}{\partial t} = \left(c + L\theta \dfrac{\partial \theta_u}{\partial T}\right)\dfrac{\partial T}{\partial t}$

Equation 5.2 considers the applied boundary heat flux, Q, and the different thermal conductivities, k_x and k_y, with respect to the capacity for heat storage, λ, as it changes over a time-dependent, t, temperature gradient. The capacity for heat storage is composed of two parts: the volumetric heat capacity, c, that depends on whether the material is frozen or unfrozen, and L, the latent heat of fusion of water. The latent heat calculation requires the volumetric water content, θ, and the unfrozen volumetric water content, θ_u.

The governing equation must always balance with the boundary conditions specified at each element in the model. A temperature boundary condition can be specified as a constant value or as a time-dependent function. The heat flux defaults to zero under steady state conditions or when no boundary condition is specified. In other words, the heat flow that enters a node equals heat flow that exits a node. Section 5.2.4 Boundary Conditions describes the boundary conditions used in the author's model.

5.2.2 Geometry

The geometry chosen for the model assumed a symmetrical embankment, and therefore only represented the instrumented half as shown in Figure 5.1. In reality, each side of the embankment has differences in solar radiation, slope, snow accumulation, and vegetation. A full embankment model was not pursued because only one side of the embankment was instrumented. The half embankment modelled also reduced the quantity of nodes and computing time compared to modelling a full embankment. The development of the model geometry was based on previous models (Kurz, 2013), and observations during drilling in 2008 and 2012. The model geometry extended 30 m laterally from the centreline, and to a depth of 12 m below the natural ground surface. The author tried models that increased the lateral extent to 40 m, but the isotherms (temperature contours) beyond 30 m were the same. The model was cut off at a depth of 12 m even though thermistor strings were installed to bedrock at a depth of 18 m because the temperatures below 12 m varied very little over a full year. The initial finite element mesh remained coarse (1 m by 1 m) until the thermistor and simulated data were in close agreement. Subsequent models used a mesh element size of 0.5 m by 0.5 m to calculate the isotherms of the ground thermal regime.

5.2.3 Material Properties

Material properties used in the thermal modelling are summarized in Table 5.1. Calculations for the material properties are included in the Appendix. All materials were modelled using a full thermal model, which requires intrinsic properties in frozen and unfrozen states including: volumetric heat capacities (c_u and c_f), thermal conductivities (k_u and k_f), the in-situ volumetric water content (VWC), and the unfrozen volumetric water content.

Chapter 2 explained that the amount of heat that flows through a unit area of a substance in a unit of time under a unit temperature gradient is called the thermal conductivity (Farouki, 1986). Thermal conductivity reflects of the ability of the soil to transmit heat between the matrix of soil particles and pore fluids (both water and ice) through direct contact or indirectly through the soil pore fluids. Thermal conductivity is a function of the water content, degree of saturation, soil type, soil density, and temperature. The thermal conductivities of the silty clay used in the thermal model were based on laboratory tests conducted by Kurz (2013) on specimens from the PR 391 site. The unfrozen thermal conductivities of the clay specimens were between 1.18 and 1.51 W/m/°C while the frozen thermal conductivities ranged from 1.21 to 2.42 W/m/°C.

Unfrozen volumetric water content is the percentage of water that remains unfrozen and is absorbed on the surface of the particle at temperatures below 0°C. Some water remains unfrozen in fine-grained soils at temperatures below 0°C because the soil particles have large surface areas relative to their small size.

Temperature dependent functions in TEMP/W calculated thermal conductivities and unfrozen volumetric water contents. The functions required the soil type, and frozen and unfrozen material properties. TEMP/W assumed the material properties changed as temperature passed through the freezing point of 0°C in the full thermal model. The unfrozen volumetric water content function assumed 5% similar to relationships found in Andersland and Ladanyi (2004) and Farouki (1986) as used in thermal modelling by Kurz (2014).

The volumetric heat capacity and in-situ volumetric water contents calculations used the relationship between dry densities and measured water contents. Heat capacity is the quantity of heat required to raise the temperature in a substance by 1°C (Andersland and Ladanyi, 2004) as explained in Chapter 2. The heat capacity of soil, c, in a unit mass, m, depends on the heat

123

capacities of the solid, water, ice, and air components of soil (c_s, c_w, c_i, and c_{air}) proportional to their mass (m_s, m_w, m_i, and m_{air}) as shown in Equation 5.3.

[Eq. 5.3] $c \left[\frac{kJ}{kg \cdot °C}\right] = \frac{1}{m} (c_s m_s + c_w m_w + c_i m_i + c_{air} m_{air})$

Specific heat is the ratio between the heat capacity of a substance and the heat capacity of water. Commonly used specific heats for solids, water, and ice are 0.17, 1.0, and 0.5 respectively. The volumetric heat capacity is equivalent to heat capacity but is expressed in terms of unit volume rather than mass while also incorporating specific heat, the density of dry soil (ρ_d) and water (ρ_w equals 1000 kg/m^3), the heat capacity of water (4.187 MJ/m$^3 \cdot °$C), and water content. Both the natural gravimetric water content, w_n, and unfrozen water content, w_u, are required. The calculations for unfrozen heat capacity, c_{vu}, and frozen volumetric heat capacities, c_{vf}, are shown in Equation 5.4 and Equation 5.5 (Andersland and Ladanyi, 2004).

[Eq. 5.4] $c_{vu} \left[\frac{MJ}{m^3 \cdot °C}\right] = \left(\frac{\rho_d}{\rho_w}\right) \left[0.17 + 1.0 \left(\frac{w_n}{100}\right)\right] c_{vw}$

[Eq. 5.5] $c_{vf} \left[\frac{MJ}{m^3 \cdot °C}\right] = \left(\frac{\rho_d}{\rho_w}\right) \left[0.17 + 1.0 \left(\frac{w_u}{100}\right) + \left(\frac{w_n - w_u}{100}\right)\right] c_{vw}$

Thermal property tests for the gravel were not performed and values were selected from Harlan and Nixon (1978). Each year, highway maintenance places 'dry' gravel on the highway over the existing gravel that was assumed to have become fully saturated. The author assumed a dry density of the gravel of 1900 kg/m^3 with a gravimetric moisture content of 3% for the 'dry' gravel. The gravel would have been compacted at a higher moisture content, but the value was chosen to distinguish it from the saturated gravel already in the embankment.

5.2.4 Boundary Conditions

Boundary conditions applied in the model included the initial conditions of the ground thermal regime, the air temperatures at the ground surface, and heat flow along the bottom boundary of

the model geometry. The thermal modelling developed by the author featured three transient analyses. Each used a different surface boundary condition as shown in Figure 5.2. The 'Climate' analysis was based on locally observed climate data. The 'Sine Function' analysis was based on a sine function that smoothed daily average air temperatures taken from the climate data. The third model used air temperature data from a climate prediction model developed by the Canadian Centre for Climate Modelling and Analysis (CCCma) to create an increasing sine function. This model was called the 'CCCma' analysis. The differences between the models are discussed further in the next three sub-sections.

A constant unit heat flux representing the geothermal gradient was applied to the bottom extent of the model (depth of 12 m) as shown in Figure 5.3. Geothermal gradients vary by location but generally range between 0.9 and 3.3°C per 100 m (Brown, 1963). A constant unit flux of 3 kJ/m^2·day was used based on the unfrozen thermal conductivity of the silty clay and a geothermal gradient of 3°C per 100 m.

Transient analyses are in a constant state of change and require a start time to establish the initial conditions. To allow the initial conditions to equilibrate, the author selected September 25, 2010 as the model start date; two years prior to the start of data collection from the field instrumentation. A spatial function established the initial temperatures on the start date as shown in Figure 5.4. A krigged surface interpolates isotherms based on temperatures applied to specified points in the two-dimensional domain to create a ground thermal regime. The specified temperatures took thermistor string data from September 2010 for the toe and mid slope and from September 2012 for the shoulder and centreline. The thermistor string data from the toe were also used on the right extent of the model so the initial isotherms were horizontal to the ground surface. The values for the initial conditions are included in the Appendix.

5.2.4.1   Climate Boundary Condition

The Thompson Airport weather monitoring station is located less than 10 km away from the project site and climate data was obtained from the Environment Canada website. Climate data was downloaded for every day since the model start date of September 25, 2010.

The climate boundary condition developed by TEMP/W required several input parameters which included: maximum and minimum daily temperatures, maximum and minimum daily relative humidity, daily average wind speed, and daily total precipitation The latitude was set at 55.8° north to incorporate the effects of solar radiation. The climate data needed to match the one-day time step used by the analysis. A constant average distribution for the climate data was recommended by Geo-Slope (2010b) for models with a one-day time step. A thin layer of finite elements called a surface layer must be constructed at the top surface to apply a climate boundary condition in a TEMP/W model.

5.2.4.2   Sine Function Boundary Condition and Modifying Factors

The natural variability of the daily average temperatures in Thompson, Manitoba is shown in green on Figure 5.5. Numerical instabilities may develop due to the large day-to-day changes in average temperature. A sine function provides an approximate representation of the yearly cycle of daily average temperature based on Equation 5.6 previously used by Kurz et al. (2012b).

[Eq. 5.6] $T = A + B \times \sin\left[2\pi\left(\frac{t+C}{365}\right)\right]$

where A = Mean Annual Average Temperature (a temperature shift calculated as -2.8°C), B = a constant (amplitude calculated as 20.9°C), t = time in days, and C = constant (a time shift calculated as 155.2 days).

The smooth red line in Figure 5.5 shows the fitted sine function based on the last four years of daily average temperatures. The sine function 'smoothed out' the erratic nature of the

actual climate data and captured the essence of temperature changes measured by Environment Canada.

Thawing and freezing indices of the air are the annual summation of the difference between the mean daily average air temperatures and the freezing point over the thawing and freezing seasons. The average air thawing and freezing indices between September 2010 and 2014 were 2014°C·days and -3015°C·days respectively based on Environment Canada data from the Thompson Airport. The sine function calculated air thawing and freezing indices as 1939°C·days and -2950°C·days respectively for the same time period. The percent difference between thawing and freezing indices of the daily mean temperatures and the sine function was acceptable at 4%. The sine function generates a slightly cooler summer and warmer winter.

The mean annual air temperature differs from the mean annual ground temperature even at a depth of 1 cm due a variety of factors including vegetation, thermal properties of the soil, and net radiation. Empirically based modifying factors (n-factors) are used to estimate ground surface temperatures based on air temperatures. TEMP/W analyses require n-factors when a temperature based function is applied to the ground surface (Geo-Slope, 2010b). The n-factor is the ratio between thawing and freezing indices of the ground surface and the air (Johnston, 1981). The magnitude of the thawing and freezing n-factors, n_t and n_f, depends on geographic location and surface conditions.

The analysis initially used recommended n-factors based on values available from literature, but later back-calculated n-factors to fit site specific conditions. The road surface started with an n_t of 2.0 and 0.6 for n_f as recommended for a gravel surface. The mid slope and toe initially used 0.73 for n_t and 0.25 for n_f based on the 'trees and brush cleared moss over peat soil' condition (Andersland and Ladanyi, 2004). A series of models were run solely to back-

calculate n-factors to uniquely fit the site. The author notes that the n-factors are lower than the typical values found in literature. N-factors are empirically based and differences between the values may be related differences in vegetation, snow accumulation, solar radiation, and other factors. Separate n-factors were chosen for the toe and mid slope because of the impact of the embankment slope. Table 5.2 summarizes the n-factors selected for the locations shown in Figure 5.6.

5.2.4.3   Forward Projection

The forward projection model used the same process as the sine function in order to examine possible long term behaviour of the embankment at this site using air temperature data from a publicly accessible climate model. The Canadian Centre for Climate Modelling and Analysis (CCCma) has developed several models to predict climate changes and variability in Canada. The CCCma Third Generation Coupled Global Climate Model (CGCM33.1/T47) provided projected air temperature data from January 1, 2001 until December 31, 2100. Figure 5.7 shows a sinusoidal representation of the CCCma air temperature data for the PR 391 project site between September 2012 and September 2022. An average air temperature of 1.76°C was predicted for the project site during the first 25 years of data collection (September 2012 to September 2037). The average temperature for the next 25 year interval (September 2037 to September 2062) increased to 2.89°C. The linear trend line in Figure 5.7 reflects the rise in average temperature from the first twenty five years after data collection began (2012 to 2037) and the next twenty five year interval (2037 to 2062). The slope of the linear trend line equated to an increase of 0.0001°C per day. The author created a rising sine function based on the linear trend line and the air temperatures in the 'Sine' model to represent projections of air temperature used in the 'CCCma' TEMP/W model. For example, the air temperature on day 500 of the

'CCCma' model added 0.05°C to the air temperature on day 500 of the 'Sine' model. The 'CCCma' model used the same n-factors described in the previous section for the 'Sine' model. The temperature projections in the 'CCCma' model are limited because the model does not account for changes in precipitation, vegetation, or hydrology. The temperature data also does not represent extreme events such as prolonged cold spells in the winter or heat waves in the summer.

5.2.5 Results and Discussion

Numerical convergence can be an important issue because computations in TEMP/W thermal models are highly non-linear. Several versions of the thermal model were developed and improved through modifications of the boundary conditions, material properties, and geometry. The modelled data were compared to the thermistor string data from the toe, mid slope, shoulder, and centreline of the embankment.

Figure 5.8 through Figure 5.15 show measured thermistor data plotted with simulated data at the toe, mid slope, shoulder, and centreline of the embankment. Measured data from the thermistor strings (shown as a symbol) were compared with the simulated values from the 'Climate' model (shown as a dotted line), the 'Sine' model (shown as a solid line), and the 'CCCma' model (shown as a dashed line).

Figure 5.8 and Figure 5.9 show the results of the models and the thermistors below the toe of the embankment. Figure 5.8 plots temperature against depth for January 2013, July 2013, February 2014, and July 2014. No thermistor data was available in January 2014 due the faulty relay switch discussed in Chapter 3. There is generally good agreement between the measured data and all three of the TEMP/W models. Similarly, Figure 5.9a and Figure 5.9b show the relationship between temperature over time at depths of 4 m and 8 m below the toe of the

embankment. Again, the model demonstrates reasonable agreement with the measured data. The 'Sine' model is generally better at reflecting the transient behaviour than the 'Climate' model. The 'CCCma' model follows the 'Sine' model very closely because even after two years (1460 days) the difference in the air temperature boundary condition applied is only 0.146°C. The plots of measured temperature data versus modelled data at the mid slope, shown in Figure 5.10 and Figure 5.11, are comparable to the observations made for the toe and again the 'Sine' model produces better simulations than the 'Climate' model.

Figure 5.12 and Figure 5.13 show results of simulated and measured temperatures below the shoulder of the embankment. Thermistor data showed 2 to 3 m of sub-zero temperatures below the shoulder beginning at a depth of 6 m. The simulated and measured results are less in agreement below the shoulder and centreline compared to the mid slope and toe shown earlier. Figure 5.13a shows the temperatures over time below the shoulder for a depth of 3 m, just above the frost bulb. At 3 m depth, the 'Sine' and 'CCCma' models agree well with the cyclic temperature trends, but the simulated temperatures are warmer. Similarly, Figure 5.13b shows temperature changes over time below the shoulder for a depth of 9 m, which is inside the frost bulb. At 9 m depth, the measured ground temperatures fluctuate very little and are more-or-less constant. The TEMP/W models, especially the 'Sine' and 'CCCma' models, capture the small fluctuations in temperature, but show a slight increasing temperature trend. The same observations are accentuated at the centreline because of the thicker layer of sub-zero temperatures. Thermistor data indicated 6 to 7 m of sub-zero temperatures below the centreline beginning at a depth of 3 m. The centreline results are shown for specific days in Figure 5.14 and specific depths in Figure 5.15.

Figure 5.16 through Figure 5.19 represent the results of the 'CCCma' model projected for twenty five years after the start of data collection start on September 2012. The 'CCCma' ran for 9870 days which meant the general warming trend resulted in an average air temperature increase of 0.987°C by the last day of the model. Figure 5.16 and Figure 5.17 show that warm temperatures at the toe and mid slope, respectively, will continue to contribute to permafrost degradation under the embankment. The author noted that the measured temperatures under the shoulder and centreline above the frost bulb had increased during the winter and spring of the second monitoring season (2013-14) compared to the same time period in the first monitoring season (2012-13). The average temperature at 3 m depth at the shoulder between March and August 2014 increased by 0.06°C compared to March and August 2013, and the increase can be observed in Figure 5.18. An increase of 0.34°C was observed at a depth of 2 m at the centreline shown in Figure 5.19 between the two same time periods. The 'CCCma' predicts that the temperatures at all locations under the embankment will increase above 0°C within the next twenty five years. As explained in Chapter 2, compared unfrozen ground, frozen ground requires more energy to increase the temperature due to the latent heat of fusion of water. Warmer temperatures simulated in the region just above the frost bulb would allow more energy to reach the frost bulb and possibly initiate thawing in the future. Two years is a small sample to evaluate long term trends, but the general warming trends predicted by the 'CCCma' model do not make it unreasonable to suggest that the frost bulb under the embankment may disappear entirely.

Further work is required to achieve closer agreement between modelled and measured values, particularly below the shoulder and centreline of the embankment. The TEMP/W models experienced trouble simulating the constant marginally sub-zero temperatures observed in the frost bulb. The difficulties are accentuated under the centreline because the frost bulb is thicker

at that location. The frost bulb appears less vulnerable to seasonal cyclic changes than the regions closer to the ground surface. The measured temperatures in the frost bulb remain relatively stable year round and fluctuate less than 0.1°C.

Assumptions about the divisions of sub-surface materials and their properties were mostly based on judgement from drilling and available literature. Only thermal conductivity tests on the silty clay had been performed in research at the PR 391 site (Kurz, 2013). Testing the thermal properties of all relevant materials, such as the gravel fill, would be useful to understanding its role in heat transfer in winter and summer.

 Enhanced understanding of the behaviour of the soils at this site at near freezing temperature would improve the modelled simulations of the frost bulb. The discrepancy can be related to the unfrozen water content function which controls how quickly water in a material is frozen at temperatures below 0°C. Unfrozen water can still be present in fine-grained soils at temperatures between -2°C and -4°C, and therefore they have an unfrozen water content function with a shallow slope (Geo-Slope, 2010b). The same slope is steeper for coarse-grained soils.

Modifications to thermal conductivity or volumetric water content can also impact the thermal behaviour in a model. Increases to thermal conductivity would increase the rate that temperatures drop below freezing as well as after the phase change (Geo-Slope, 2010b). The amount of water in a material affects how it freezes due to energy requirements at a phase change from the latent heat of fusion of water. The frost bulb can be warmed from by the geothermal gradient below and air temperatures at the surface.

The author would recommend creating a model that divides sub-surface layers into thinner layers that gradually modify thermal properties in each layer. On a similar note, the finite element mesh should be made finer under the embankment in the frost bulb region where even

small temperature changes in the frost bulb can have a large influence. Other finite element software, such as SVHeat, could be considered for 3D modelling of the ground thermal regime if more input information becomes available.

5.3   Deformation Model

The following section outlines the new deformation model developed by the author to simulate the displacements under the PR 391 highway embankment. Previous numerical models at this project site only examined the behaviour of the embankment in regards to ground temperatures (Batenipour, 2012) (Kurz, 2013). The author created a new numerical model that examines the deformation behaviour at the PR 391 project site which, to the author's knowledge, had not been previously developed for an embankment in degrading permafrost. The deformation model used the SIGMA/W software package from Geo-Slope International Ltd. The installation of the ShapeAccelArrays (SAAs) with the author's monitoring program made it possible to validate and calibrate the deformation model. The lateral and vertical displacements measured by the SAAs were compared to displacements simulated by the model. The deformation experienced by the embankment reflected the general changes in the size of the frost bulb over a single freeze-thaw cycle. Consequently, the deformation modelling depended on the results of the thermal modelling but the two models are not coupled. Geo-Slope software is not capable of simulating thermal induced displacements in a thermal-mechanical model. The frost bulb developed for the deformation model was based on general trends of its growth and regression during the freezing and thawing parts of the year as indicated by the thermistors. The following sections discuss the development of the deformation model and compares simulated displacements with SAA data taken from the site.

5.3.1 Theory

SIGMA/W is a finite element software capable of modelling stress and deformation analyses of earthworks, staged construction, soil structure interactions, consolidation analyses, and also can include the effect of excess pore water pore pressures using coupled analysis with SEEP/W. Problems are classified as either axisymmetric or two-dimensional plane strain. Solutions are formulated using small displacement and strain theory (Geo-Slope, 2010a).

SIGMA/W formulates displacements based on incremental analysis. For each time step, an incremental displacement is calculated based on the incremental load and cumulatively added to the displacement from the previous time step. SIGMA/W can only calculate the end conditions of a stress-strain problem if the in situ conditions were defined prior to loading. The governing equation of SIGMA/W for two-dimensional plane strain analysis is shown in Equation 5.7 and requires three main inputs: geometry, material properties, and boundary conditions.

[Eq. 5.7] $t \int_A [B]^T [C][B] dA \{a\} = bt \int_A \langle N \rangle^T dA + pt \int_L \langle N \rangle^T dL$

where:

t = constant unit element thickness

A = area along the boundary of an element

[B] = strain-displacement matrix

[C] = constitutive matrix

{a} = column vector of nodal increments x- and y- displacements

b = unit body force intensity

<N> = row vector of interpolating functions

p = incremental surface pressure

L = length along the boundary of an element

A model is defined as a domain of geometric objects divided into small finite elements that are each governed by material properties and boundary conditions. The concept of geometry and mesh properties was previously explained in Section 5.2.1 Theory for the thermal modelling. They remain the same for the deformation modelling. The geometry and mesh properties for the deformation model are discussed in Section 5.3.2 Geometry.

Selection of appropriate material properties is crucial for a SIGMA/W model because the self-weight of the soil is included in the analysis. Several constitutive soil models are available including: linear elastic, anisotropic elastic, nonlinear elastic (hyperbolic), elastic plastic, and Modified Cam Clay. It is good practice to first use simpler constitutive models like linear elastic where stress is directly proportional to strain before progressing to more complex models such as Modified Cam Clay to account for critical state soil behaviour. SIGMA/W does not require Atterberg limits, but it useful to realize large strains are possible for soils between the plastic and liquid limits. Solutions cannot converge for such conditions because SIGMA/W was intended for small strains, reiterating the importance of establishing models in their serviceable range of conditions. The material properties are discussed further in Section 5.3.3 Material Properties.

Boundary conditions are applied to the model to replicate loading conditions in the real world and are applied directly to geometric objects such as surfaces, regions, or points. In SIGMA/W, boundary conditions are used to represent hydraulic and stress-strain conditions for the in situ conditions prior to loading and when the load is applied. The initial water table and consequent hydraulic gradients are defined using hydraulic boundary conditions. Stress-strain boundary conditions can be applied as a displacement, a force, or a stress. The boundary conditions used are discussed in Section 5.3.4 Boundary Conditions.

5.3.2 Geometry

The cross-section of the deformation model is shown in Figure 5.20. The geometry of the deformation model was identical to the thermal model with one difference, the bottom extended to a depth of 18 m to reach bedrock instead of 12 m. As stated earlier, the deformation model is not coupled with the TEMP/W analysis, so strengths were not a function of temperature. Instead, the frost bulb was defined as a region in the model domain and given different strength properties. The size and shape of the frost bulb region used in the deformation model was approximated using the results from a separate TEMP/W analysis called the 'Snapshot' model. The 'Snapshot' model used a spatial function, as described in Section 5.3.4 Boundary Conditions, to create thermal regimes for a single day in each month since data collection began in September 2012. Krigged surface interpolation of thermistor string data created the ground thermal regimes. The thermal regimes created by the 'Snapshot' model showed the size of the frost bulb on each day of the model. For example, a spatial function used September 25, 2012 thermistor string data to create a thermal regime for September 25, 2012 followed by a spatial function to create a thermal regime for October 25, 2012 using thermistor string data from October 25, 2012, and so on. A short video clip of each day of the 'Snapshot' model is included in the Appendix. A series of layered regions around the frost bulb represented its general change in size with the seasons for the deformation model based on the 'Snapshot' model shown in Figure 5.21. The frost bulb was considered the smallest in the fall season when the ground temperatures are the warmest and the largest in late spring when ground temperatures are coldest as discussed in Chapter 4. Results of the 'Snapshot' model are included in the Appendix. The model ran for two years and was divided into 90 day seasonal segments beginning with the fall season. Each subsequent season declared the previous season as a parent analysis. The mesh element size used in the analysis was set at 0.5 m by 0.5 m.

136

5.3.3 Material Properties

The properties of the seven different materials specified in the deformation model are shown in Table 5.3. The regions of the materials were differentiated based on drilling, interpretation of instrumentation collected data, and early versions of the model. The model used linear elastic models with effective parameters for all materials using typical mechanical properties found in literature (Budhu, 2007). The silty clay and clayey silt were each given a Young's modulus of 3 MPa, but the silty clay was given a much smaller hydraulic conductivity. The material properties of the frost bulb in the model reflected its seasonal changes. Frozen material is stronger than unfrozen material and it was evident from Figure 4.34 that the frost bulb restricts the lateral movement at the shoulder. The frozen clay was given a Young's Modulus of 100 MPa to make it stronger than the regular silty clay. Section 4.5.3 Ground Movements explains that thawed material significantly loses effective shear strength due to the increase in pore water pressure. Therefore, the thawed clay around the frost bulb was given a Young's modulus of 1 MPa to make it noticeably weaker than the regular silty clay. The lower silty clay was given a stiffer Young's Modulus of 50 MPa to reflect the reduced lateral movement recorded by the SAA. The gravel was split into two regions; gravel applied during recent road maintenance was assumed to have different stiffness than the existing gravel. In Figure 4.34, there was a change in the rate of deformation at a depth of 0.5 m possibly reflecting a change in strength. The gravel below that depth deformed much more rapidly than the gravel above which is stiffer and possesses a larger Young's Modulus.

137

5.3.4 Boundary Conditions

Two hydraulic and three different stress-strain boundary conditions were applied in the deformation model. General soil conditions at the site were extremely wet as was noted in Chapter 3: Site Characterization and Laboratory Testing. A water table was applied to the ground surface for the initial conditions, while subsequent stages of the model applied a potential seepage face to the ground surface beyond the toe of the embankment. The stress-strain boundary conditions were applied to the outer extents along the sides and bottom, and to the road surface. A Fixed X/Y boundary condition was applied at all stages of the model to the bottom boundary at a depth of 18m. A Fixed X/Y boundary condition allows no movement laterally or vertically and was appropriate for the depth of bedrock. A Fixed X boundary condition was applied at all stages of the model to the left and right extents of the model assuming that movement at these locations could only happen in the vertical direction.

Thermally induced displacement could not be modelled in SIGMA/W. Consequently, SIGMA/W requires a change in stress after its initial steady-state conditions in order for a deformation to be modelled. Vehicular traffic and gravel applied during maintenance are the only new loads to the existing embankment on PR 391. A deformation model on PR 290 was briefly explained in Chapter 2. Ciro (2006) applied stress to his model by removing the embankment fill in the freezing season and returning it during the thawing season. The author chose to apply a constant normal load to the road surface to induce deformation. A load of 60 kPa was selected after some sensitivity analysis with different loads. Even though the load was much higher than the amount expected with yearly maintenance (possibly 5 kPa for 0.25 m of gravel), it corresponded well with SAA readings. For example, a road load of 5 kPa only simulated a maximum cumulative displacement of 25 mm compared to a measured maximum in the same time period of 288 mm.

5.3.5 Results and Discussion

Numerical modelling in SIGMA/W uses incremental analysis to calculate the cumulative displacement that results from the applied loads. The results of the deformation model in SIGMA/W were compared with the actual measurements recorded by the SAAs installed vertically at the shoulder and horizontally between the toe and centreline.

Figure 5.22 shows the results of the deformation model in the summer of 2014 after two years. At this point, the frost bulb had experienced two full cycles of seasonal variations in size as discussed in Section 5.3.2 Geometry. The contour lines represent the deviatoric stresses in 500 kPa intervals starting at 0 kPa. The colours blue and red represent the smallest and highest deviatoric stresses, respectively. The greatest deviatoric stresses are located at the base of the gravel fill close to the centreline above the frost bulb between 3 and 5 m depth. It is apparent that as the deviatoric stress increases, shear strains develop along the top edge of the frost bulb. The magnitude and direction of displacement is denoted by the red displacement vector arrows. There are large downward displacement (settlements) observed in the embankment closest to the centreline. The displacements dissipate in the frost bulb region and lower silty clay. The increased downward displacement in the gravel fill encounters resistance with the stronger frozen, silty clay in the frost bulb and reduces the amount of displacement to a negligible amount by comparison. The shear strains in the thawed silty clay, along the top edge of the frost bulb, drive movement outward laterally away from the centreline as seen more easily in the magnified view of Figure 5.23.

A comparison of the lateral displacement at the shoulder measured by the SAA and the results of the deformation model are shown in Figure 5.24. The modelled values share generally the same shape as the SAA data with inward movement in the gravel near the top of the embankment and outward movement below the gravel before the frost bulb. The extent and

magnitude of inward movement is less pronounced in the model than the SAA data indicates. In both cases, the defined area of the frost bulb (indicated as the blue region in Figure 5.24) restricts movement. In the model, small outward deformation continues beneath the frost bulb while very little deformation is measured below the frost bulb by the SAAs. The depth of peak outward deformation measured by the SAA was recorded at the top edge of the frost bulb, below the depth simulated in the model.

Figure 5.25 shows a comparison between the vertical displacements measured by the SAA and the results of the deformation model. The overall downward trend of the embankment was replicated well in the model. Both the measured SAA data and the deformation demonstrate that displacement is larger beneath the centreline of the embankment than the toe. It is clear in the model that during the summer-to-fall period, the rate of deformation increases as the weaker thawed part of the frost bulb contributes to increased deformations. For example, the SAA measured 58 mm of downward displacement between October 17, 2013 and February 12, 2014 and 28 mm between February 12, 2014 and April 15, 2014 compared 48 mm and 19 mm downward displacement expected by the deformation model during the same respective time periods.

Figure 5.26 plots the cumulative vertical displacement versus time at the toe, mid slope, shoulder, or centreline. The solid and dashed lines represent data recorded by the SAAs and the deformation numerical model respectively. The black, red, green, and blue lines represent the toe, mid slope, shoulder, and centreline of the embankment respectively. The SAA data indicate a small increase in the rate of deformation during the fall-to-summer period, and an upward spike during the spring. The model was unable to capture the upward spike. Chapter 4 attributed the

upward movement to the seasonal changes in ground water conditions measured by the piezometers at the toe (refer to Figure 4.36).

The implications of ground water flow require further attention. The piezometers at the toe indicated upward gradients during the winter caused by suction pressure (negative potential) as the freezing front migrated deeper with cooling ground temperatures. In the spring, the upward spike in deformations coincides with the transition from an upward hydraulic gradient to hydrostatic conditions. Meanwhile, a downward hydraulic gradient was observed at the centreline. Only two hydraulic boundary conditions were used in the deformation model, the initial water table and the potential seepage face at the natural ground surface. The meltwater from the degradation of the frost bulb and an upward gradient would both contribute to a reduction in effective stresses. The corresponding loss of shear strength would then lead to greater lateral and vertical displacement.

The 'CCCma' thermal model predicted ground temperatures under the embankment would increase enough over the next twenty five years to eliminate the frost bulb. Frozen ground is less compressible than unfrozen ground, and combined with the additional meltwater from the frost bulb thawing, embankment instability is possible. The author recommends that potentially problematic highway sections are identified and that necessary maintenance and rehabilitation occurs. Section 2.7 mentioned some, but not all, of the currently available permafrost construction techniques and considerations including drainage.

The effect of the material strength properties around the frost bulb on the deformations could be explored further in future work. Ideally, the mechanical strength properties would be a function of the temperature. As stated in Section 5.2.3 Material Properties, unfrozen water may still exist in fine-grained soils at temperatures below 0°C. The higher road surface load of 60 kPa

was subsequently selected based on the assumption that the frost bulb was significantly stiffer than the surrounding soil because it was frozen. The deformations in a thermal-mechanical model would be based only on changes in temperature and this would preclude the need to apply a non-existent load.

Geo-Slope intends to include thermal-mechanical coupled models to simulate frost heave and thaw consolidation in future versions of their software, but this feature is not available in the most current version. The author recommends that future numerical modelling consider attempts with other software to overcome the limitations of SIGMA/W in order to achieve greater agreement in the deformation models. As mentioned with regards to the thermal models, reducing the mesh size under the embankment where the most dramatic deformations occur may provide useful insights. The finite difference software FLAC developed by the ITASCA Consulting Group Inc. can simulate deformation behaviour in soils. FLAC has the ability to simulate the development of thermally induced displacement (FLAC). The user can create an add-in constitutive model to change the soil strength as a function of temperature. Groundwater can also be incorporated into the numerical models. ABAQUS is a finite element software often used in mechanical engineering applications such as the automotive industry. The software is capable of thermal-mechanical coupling and incorporating pore water pressures.

5.4   Summary

This section outlined the numerical models developed for the PR 391 project site by the author. The purpose of the numerical modelling was to develop models calibrated with actual data in order to replicate observed behaviour through simulation, enhance the understanding of the current performance of the embankment, and make an assessment on its future behaviour.

The numerical models included three thermal models using TEMP/W and a deformation model using SIGMA/W. Thermal models enhanced previous models (Batenipour, 2012) (Kurz, 2013) to simulate the current thermal regime under the embankment and to understand potential future behaviour as the result of environmental changes. Additional thermistors at the shoulder and centreline supplemented existing thermistors at the toe and mid slope for a more thorough examination of the thermal regime across the entire embankment. The thermal models included a 'Climate' model based on the climate function in TEMP/W, a 'Sine' model using a sine function fitted to the daily average air temperatures, and a 'CCCma' model featuring sine function fitted daily average air temperatures developed for a forward projection model. Calibration was performed on the modifying factors to account for the difference between the air temperature and the ground temperature for the 'Sine' and 'CCCma' models.

There was generally good agreement that improved with depth between the simulated model values and the measured thermistor data at the toe and mid slope of the embankment. The simulated modelled temperatures were still close to the thermistor data at shallower depths at the centreline and shoulder of the embankment. Discrepancy between the simulated and measured ground temperatures data increased at the frost bulb depths under shoulder and centreline. The 'Sine' and 'CCCma' models agreed with measured ground temperatures better than the 'Climate' model, but all three models simulated warmer temperatures than the observed values. There are indications the cold winter temperatures are not penetrating the soil as thoroughly as in the past since the temperatures just above the frost bulb depths have increased over the two years. Warming trends projected by the 'CCCma' model may lead to the degradation and possible disappearance of the frost bulb in the next twenty five years.

The deformation model was the first developed for the PR 391 project site. Ciro (2006) developed a deformation model for PR 290 but was unable to compare the simulated data to actual measured movements. As explained in Chapter 3, the author installed SAAs to measure lateral and vertical displacement in the embankment. The author developed a SIGMA/W model to simulate the deformation behaviour of the embankment and compared the results to measured displacements. The seasonal growth and regression trends of frozen ground were incorporated into the model. Thermistor data was used to create regions of frozen and unfrozen ground in the SIGMA/W model. After sensitivity analysis of the road surface load and material properties, the model replicated deformation. The simulated deformations in the model generally agreed with the shape of lateral movements observed by the SAA, but the accuracy of magnitude was limited. The frost bulb restricted the outward, lateral displacement of the embankment since frozen ground is less compressible than the unfrozen ground. The cumulative downward displacement observed at the centreline of the model and the SAA was close to the observed 300 mm, but the model was unable to capture the upward spike observed each spring. The upward spike was related to the seasonal change in the hydraulic gradient observed at the toe as discussed in Chapter 4. The results of the numerical models suggest possible excessive deformations in the near future of the PR 391 embankment. The author recommends coupling SEEP/W with the TEMP/W and SIGMA/W to examine the effect of seepage. The author also recommends exploring the capabilities of other numerical modelling software capable of 3D thermal modelling and thermal-mechanical modelling in future work involving permafrost.

Table 5.1: TEMP/W Model. Thermal Material Properties

Material	Vol. Heat Capacity [kJ/m^3/°C]		Thermal Conductivity [kJ/d/m^3/°C]		Thermal Conductivity [W/m/°C]		In-Situ VWC [m^3/m^3]
	c_u	c_f	k_u	k_f	k_u	k_f	
Silty Clay	2760	1960	107	161	1.24	1.86	0.41
Clayey Silt w/ Organics	2850	2050	123	209	1.42	2.42	0.41
Gravel Sat.	2505	1958	233	328	2.70	3.80	0.28
Gravel Dry	1591	1472	130	86	1.50	1.00	0.06

Table 5.2: TEMP/W Model. Surface Modifying Factors

Material	Thawing n_t	Freezing n_f
Road Surface	0.3	0.3
Mid Slope	0.1	0.6
Toe	0.01	0.73

Table 5.3: SIGMA/W Model. Mechanical Properties.

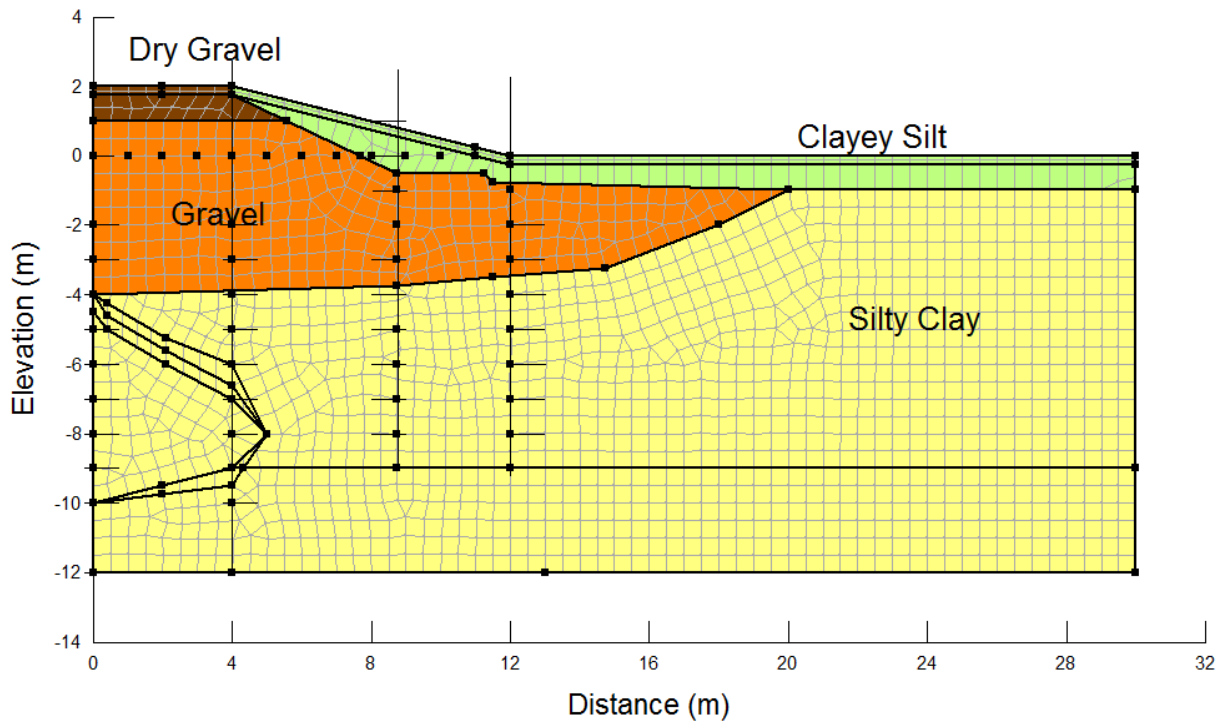| Material	Drained vs. PWP Changes	Unit Weight [kN/m^3]	E [MPa]	k [m/day]
Clayey Silt	PWP Changes	15	3	8×10^{-4}
Silty Clay	PWP Changes	15	3	1×10^{-5}
Lower Silty Clay	PWP Changes	15	50	1×10^{-5}
Frozen Clay	PWP Changes	15	100	1×10^{-7}
Thawed Clay	PWP Changes	15	1	1×10^{-7}
Upper Gravel	Drained	19	200	–
Lower Gravel	Drained	19	70	–

Figure 5.1: TEMP/W Model Cross Section of the PR 391 Embankment Project Site
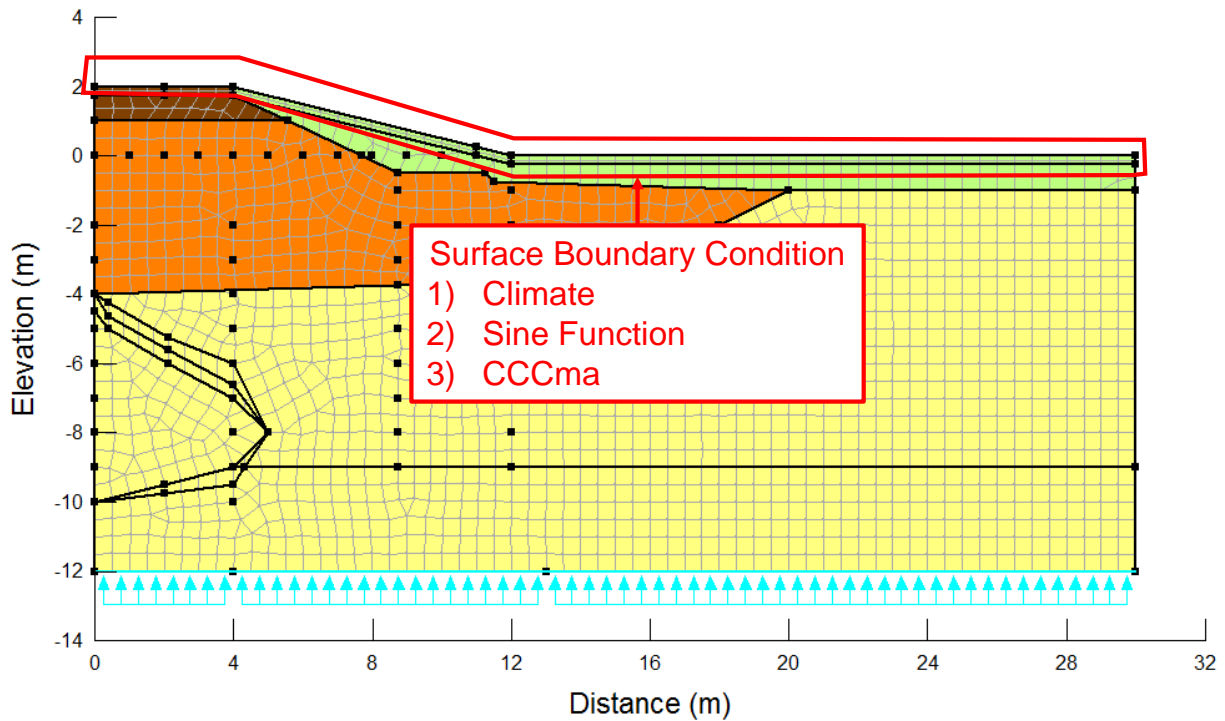

Figure 5.2: TEMP/W Model. Different surface boundary conditions applied to each version of the model: 1) Climate, 2) Sine Function, and 3) CCCma
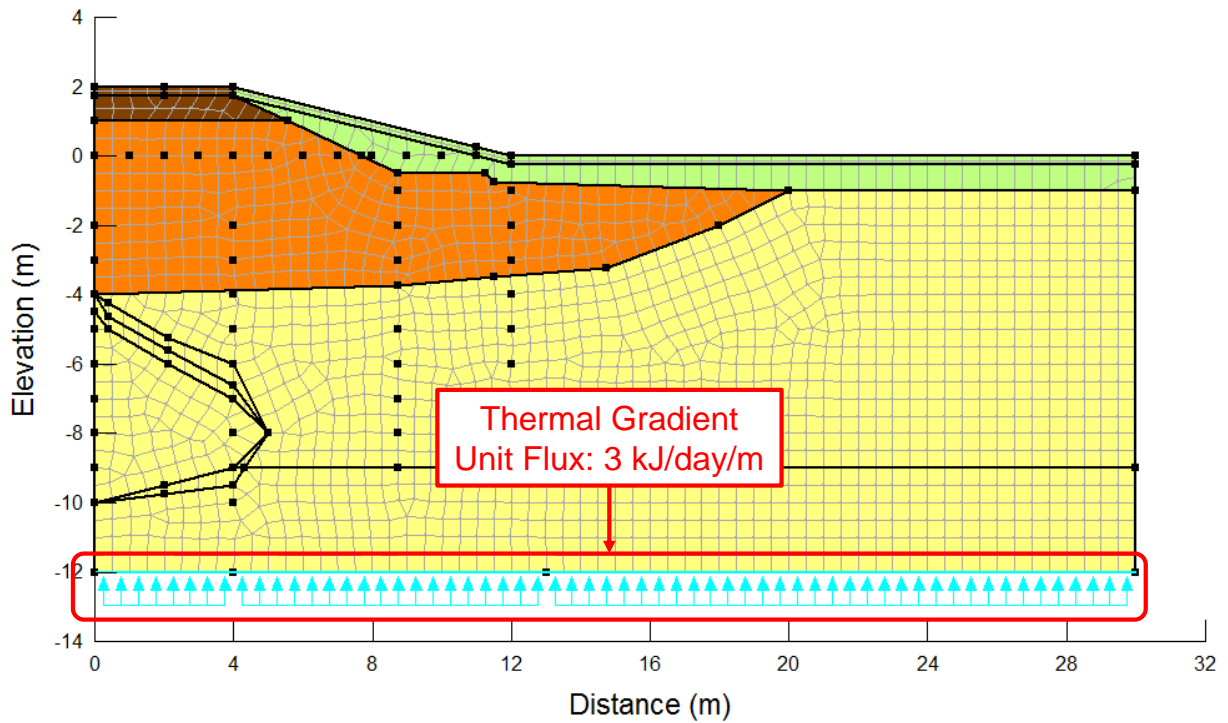
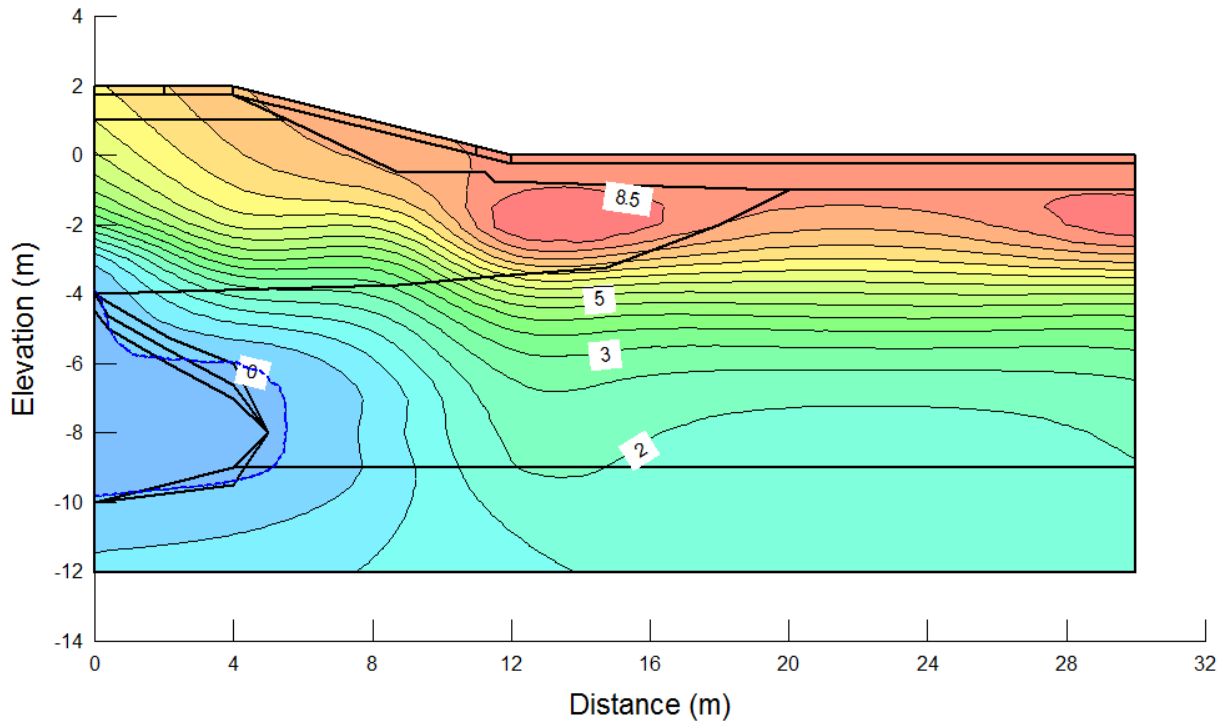Figure 5.3: TEMP/W Bottom Boundary Condition. Constant Unit Flux for Thermal Gradient.

Figure 5.4: TEMP/W Model for Initial Conditions for September 25, 2010 using a Spatial Function with Krigged Surface Interpolation. Temperature increase in 0.5°C isotherms from coldest (blue) to warmest (red).

147
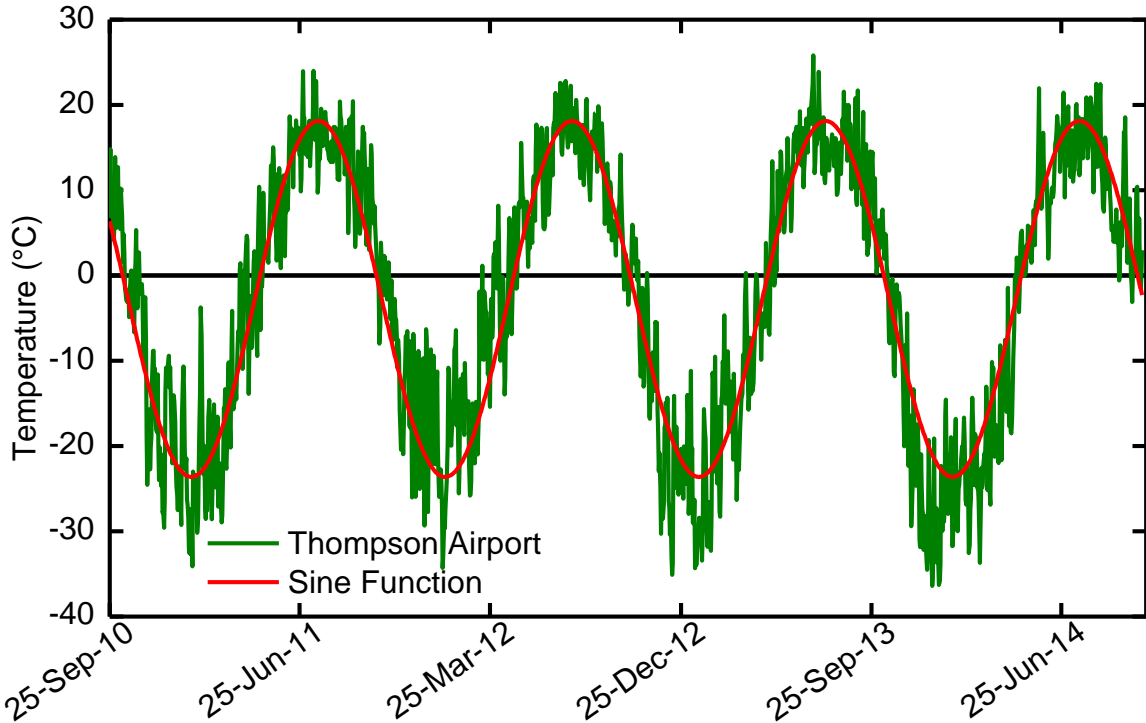
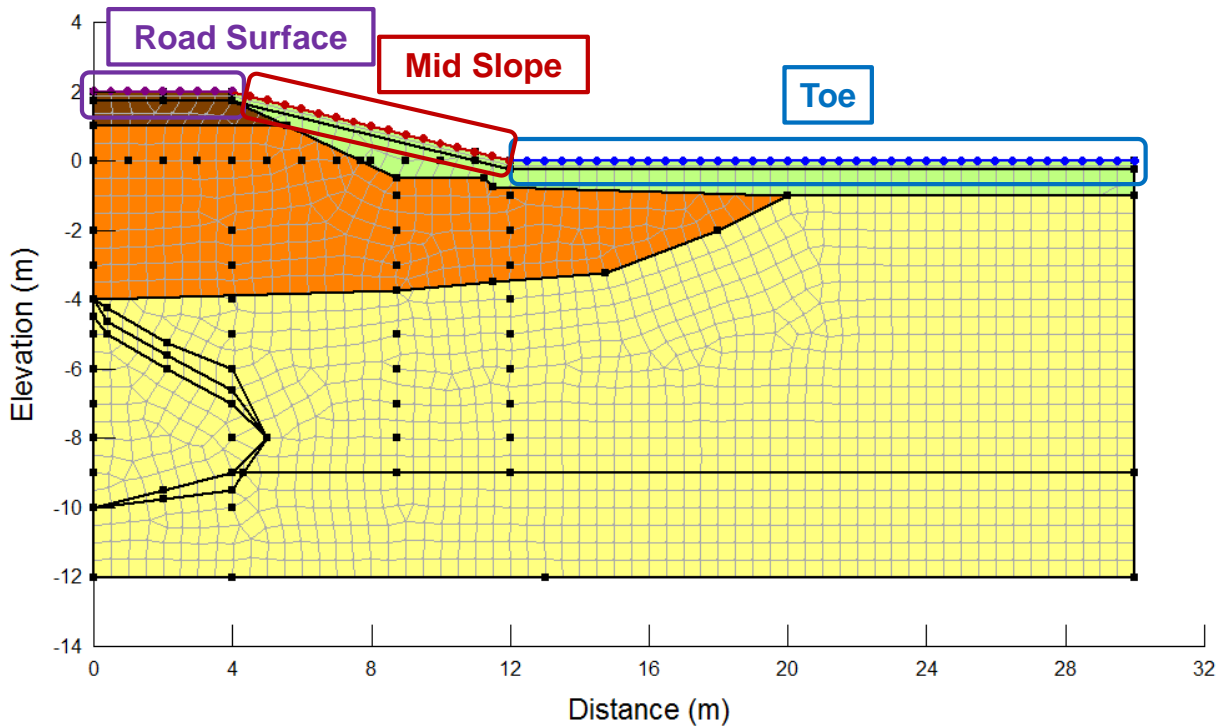Figure 5.5: Mean Daily Temperature; Environment Canada Data and Fitted Sine Function

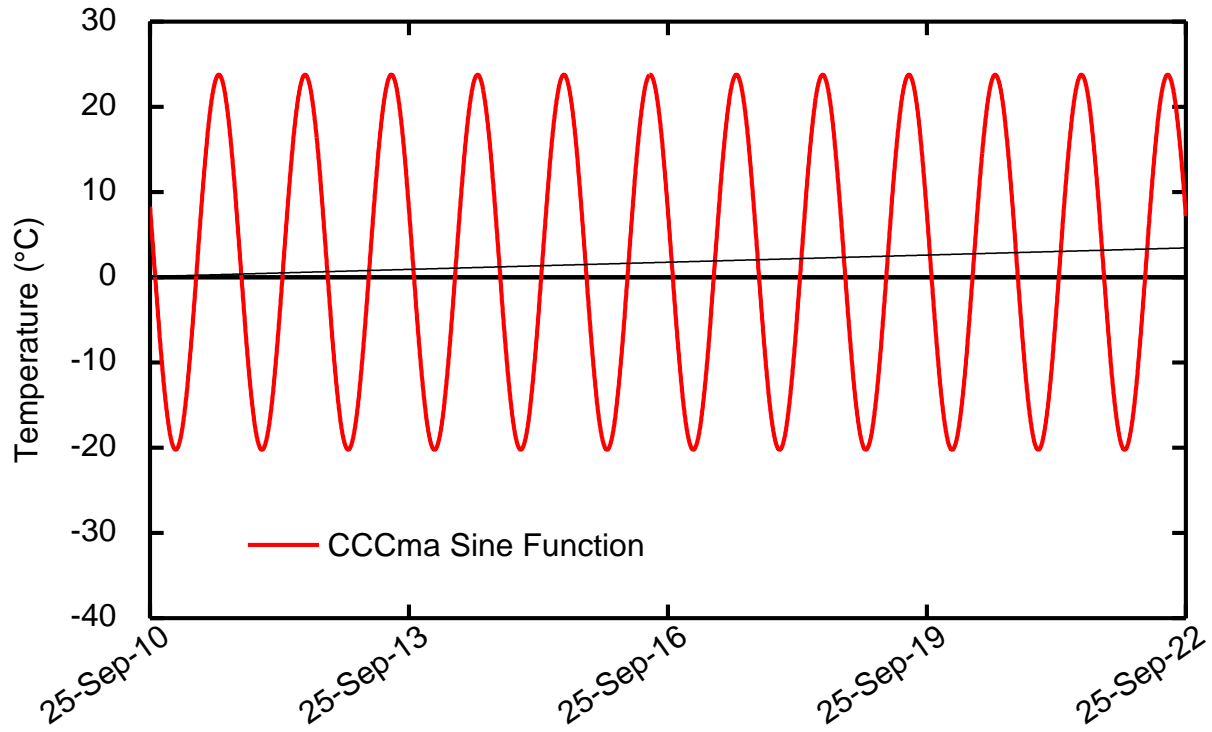Figure 5.6: TEMP/W Model. Locations where the modifying factors (n-factors) were applied at the surface.

Figure 5.7: Mean Daily Temperature; CCCma Data and Fitted Increasing Sine Function from September 25, 2010 until September 25, 2022 with 0.0001°C/day trend line.
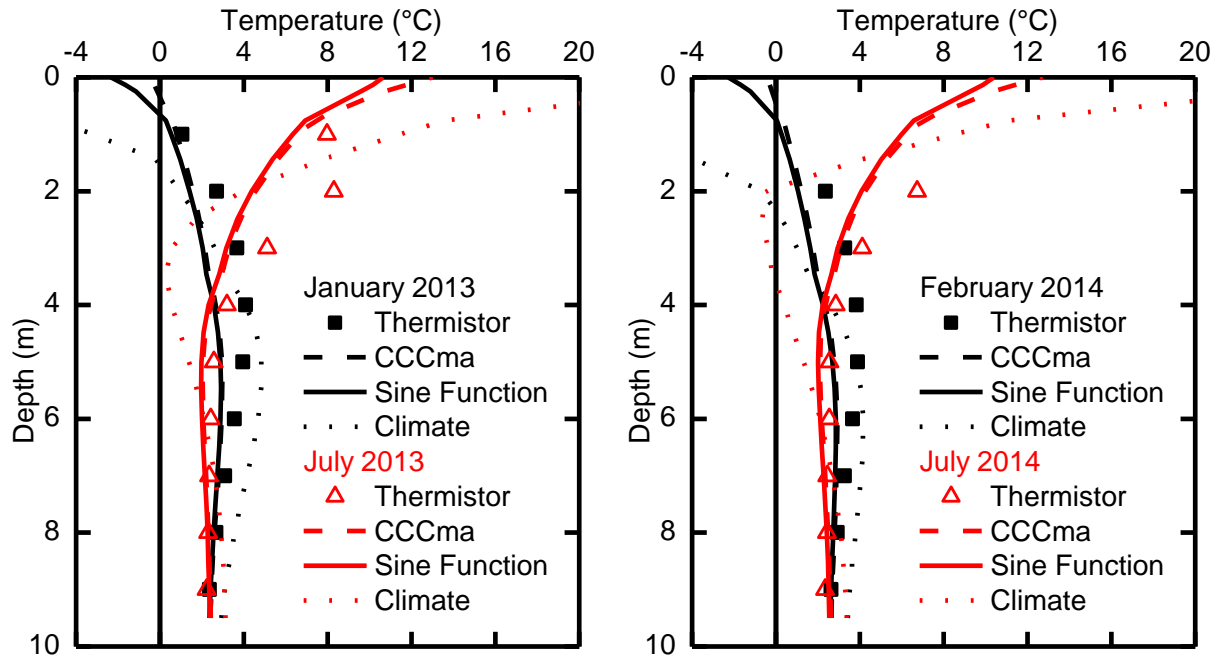
Figure 5.8: Comparison of measured, Climate, and Sine Function results at toe of embankment.
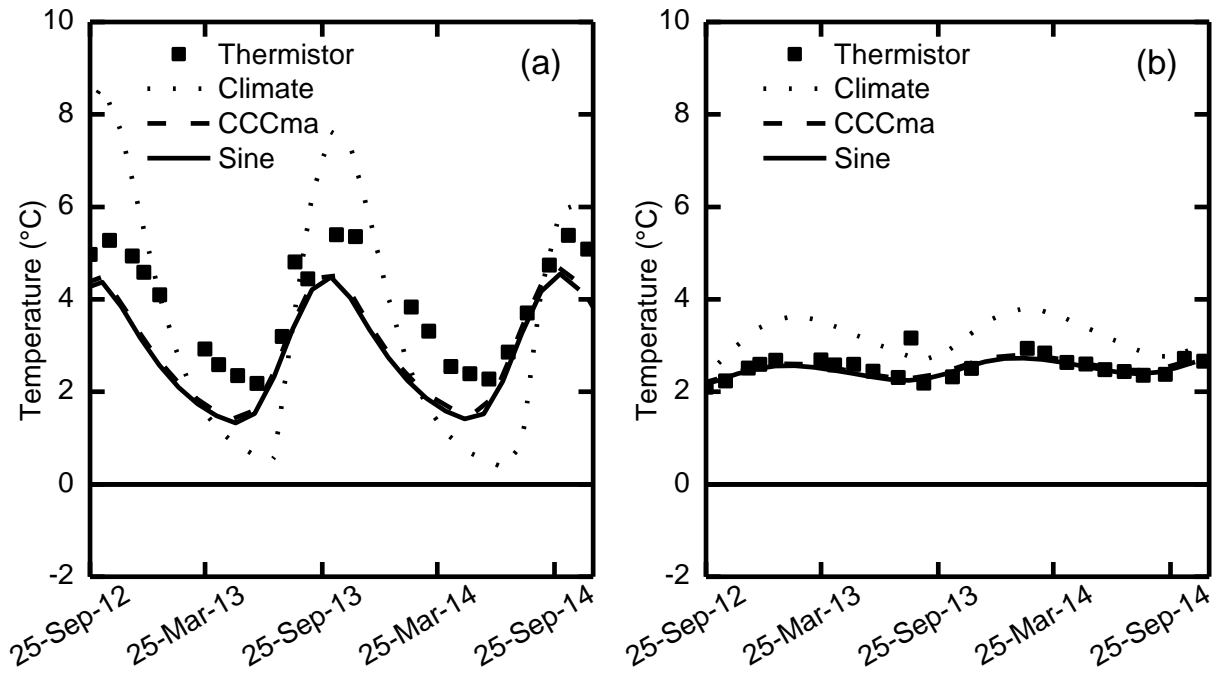

Figure 5.9: Comparison of measured, Climate, and Sine Function at a depth of (a) 4 m and (b) 8 m at the toe of the embankment
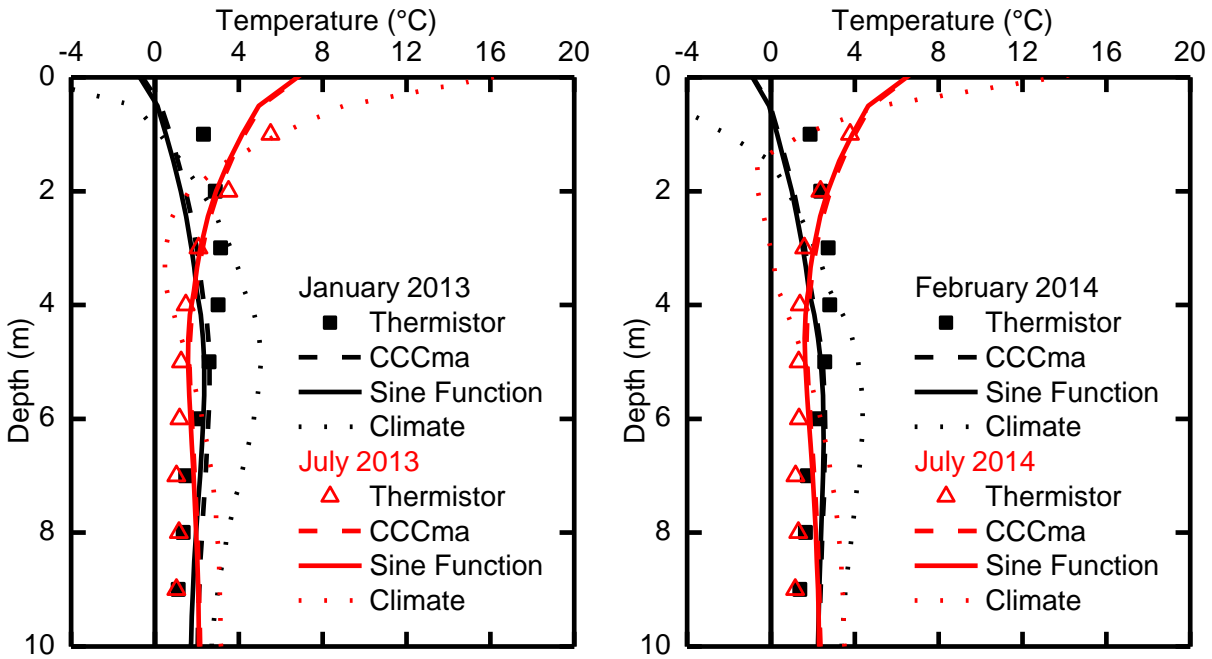
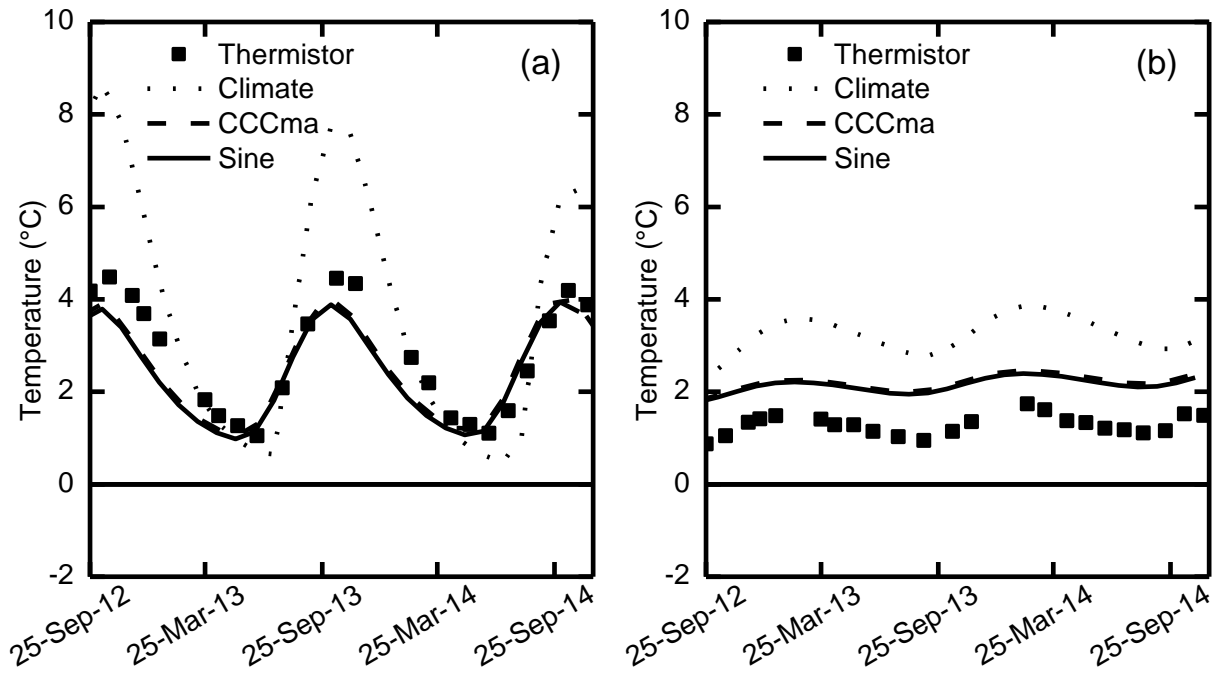Figure 5.10: Comparison of measured, Climate, and Sine Function results at mid-slope of embankment.

Figure 5.11: Comparison of measured, Climate, and Sine Function at a depth of (a) 4 m and (b) 8 m at the mid-slope of the embankment
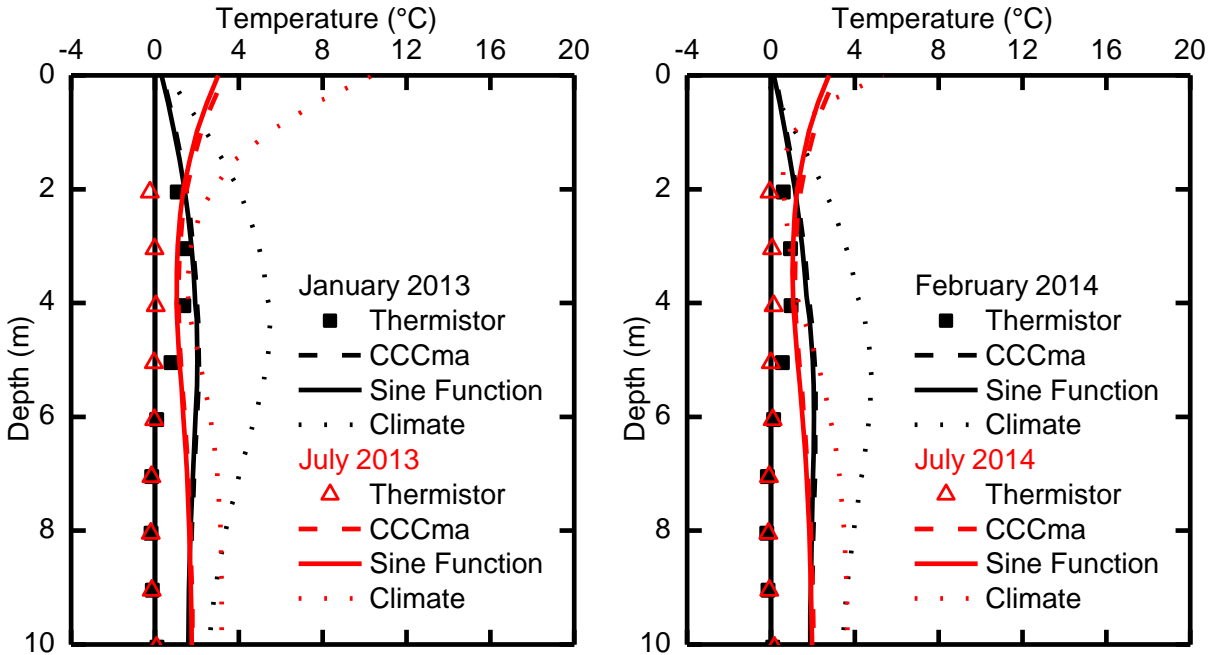
Figure 5.12: Comparison of measured, Climate, and Sine Function results at the shoulder of embankment.

Figure 5.13: Comparison of measured, Climate, and Sine Function at a depth of (a) 3 m and (b) 9 m at the shoulder of the embankment.

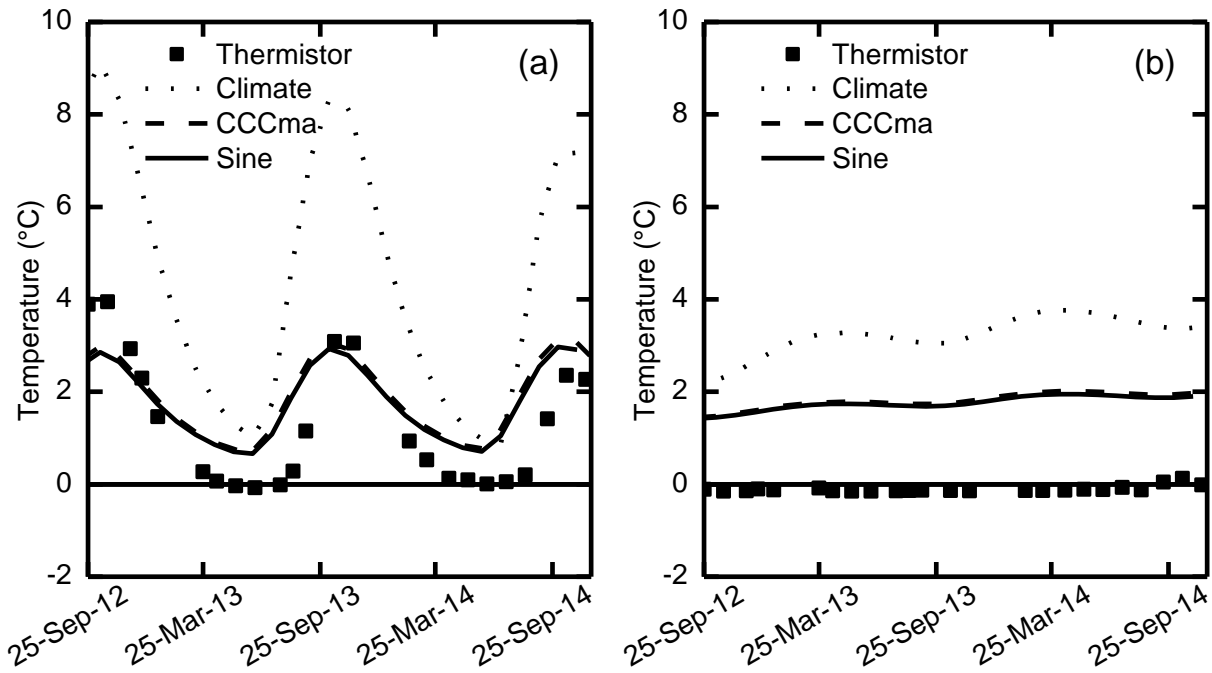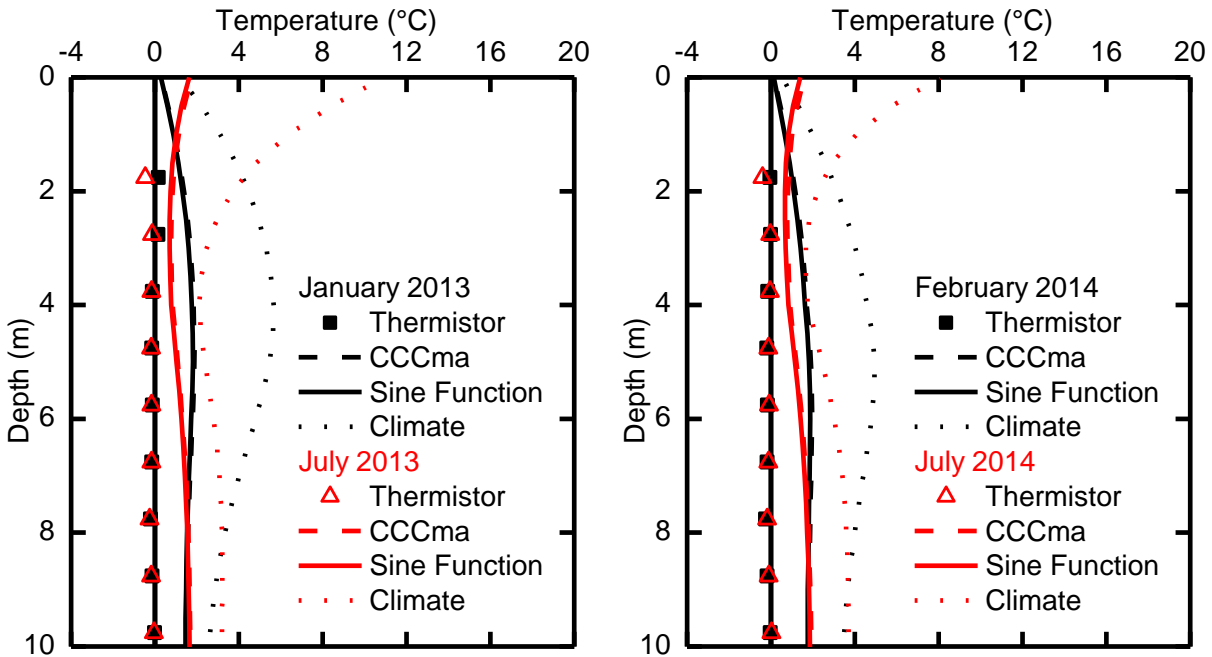Figure 5.14: Comparison of measured, Climate, and Sine Function results at the centreline of embankment.
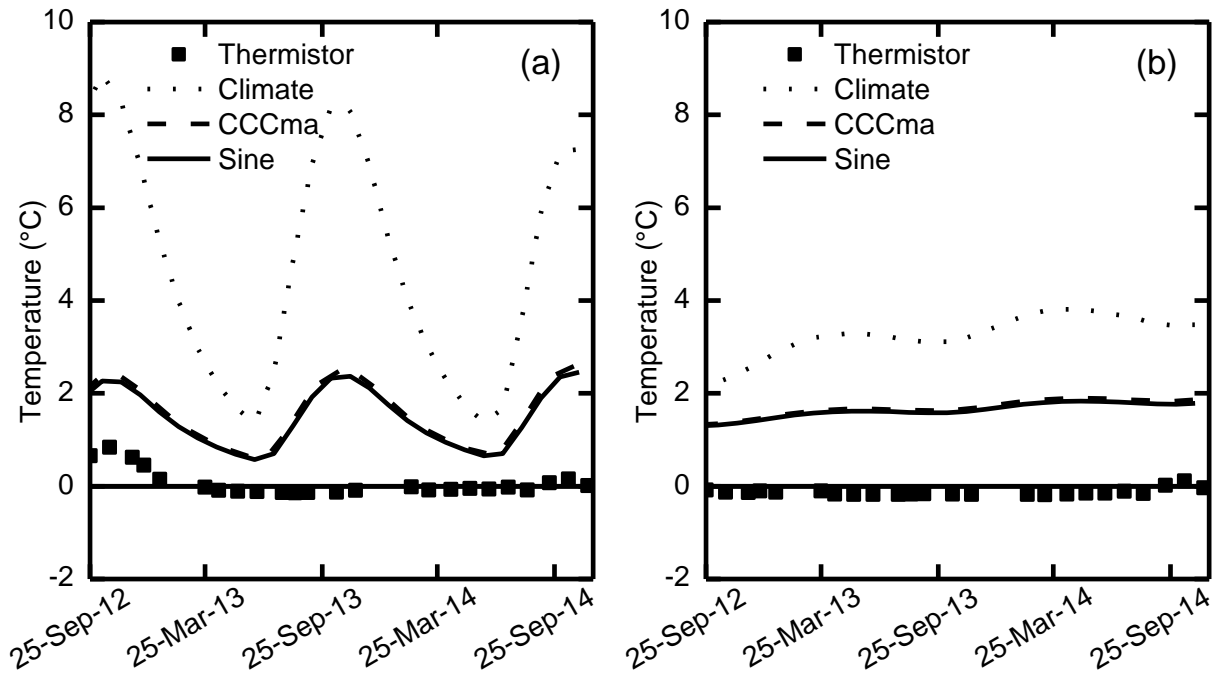
Figure 5.15: Comparison of measured, Climate, and Sine Function at a depth of (a) 3 m and (b) 9 m at the centreline of the embankment.
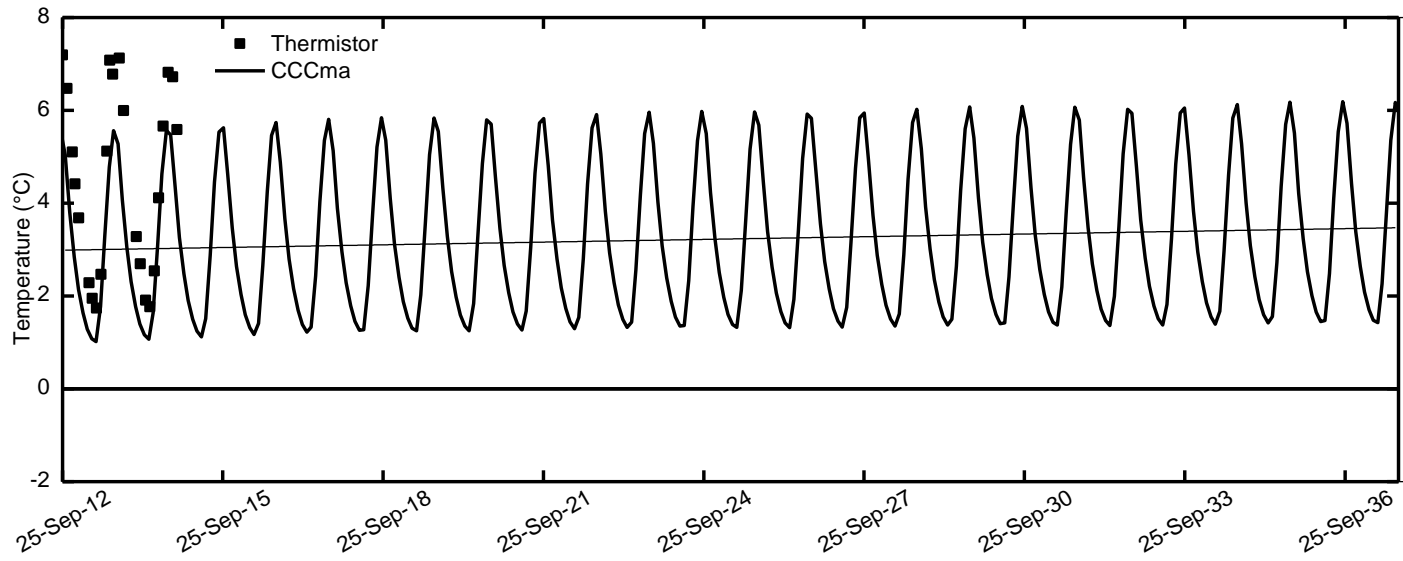
Figure 5.16: Temperature versus time for 25 years at 3 m below the toe of the embankment
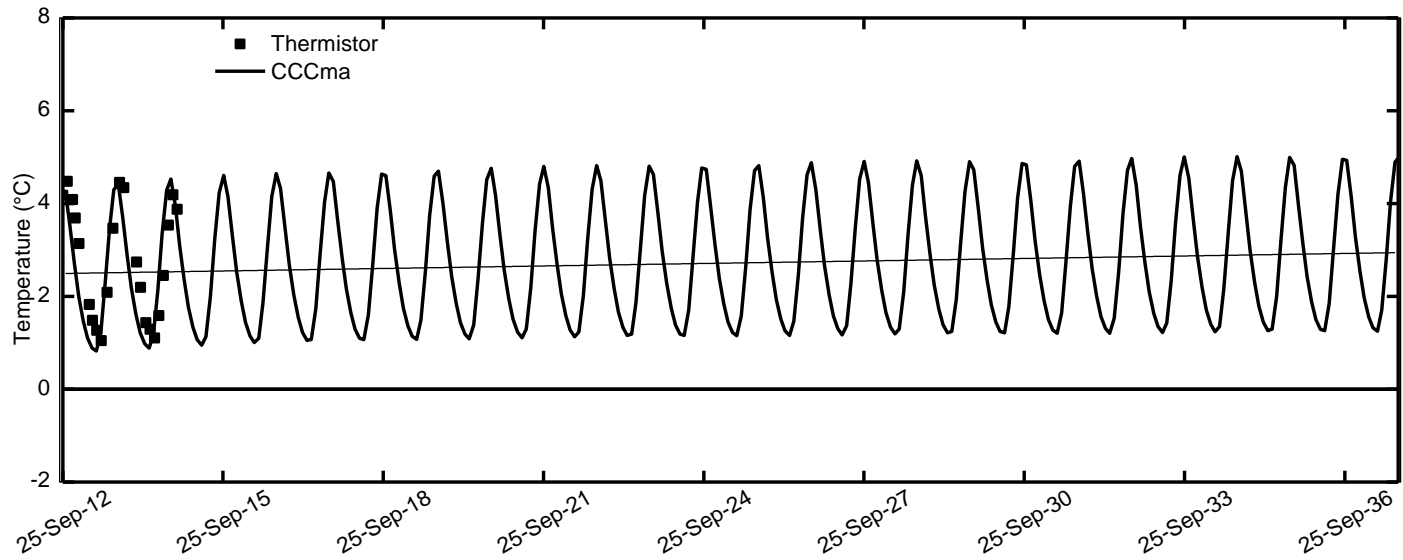
Figure 5.17: Temperature versus time for 25 years at 3 m below the mid slope of the embankment

154
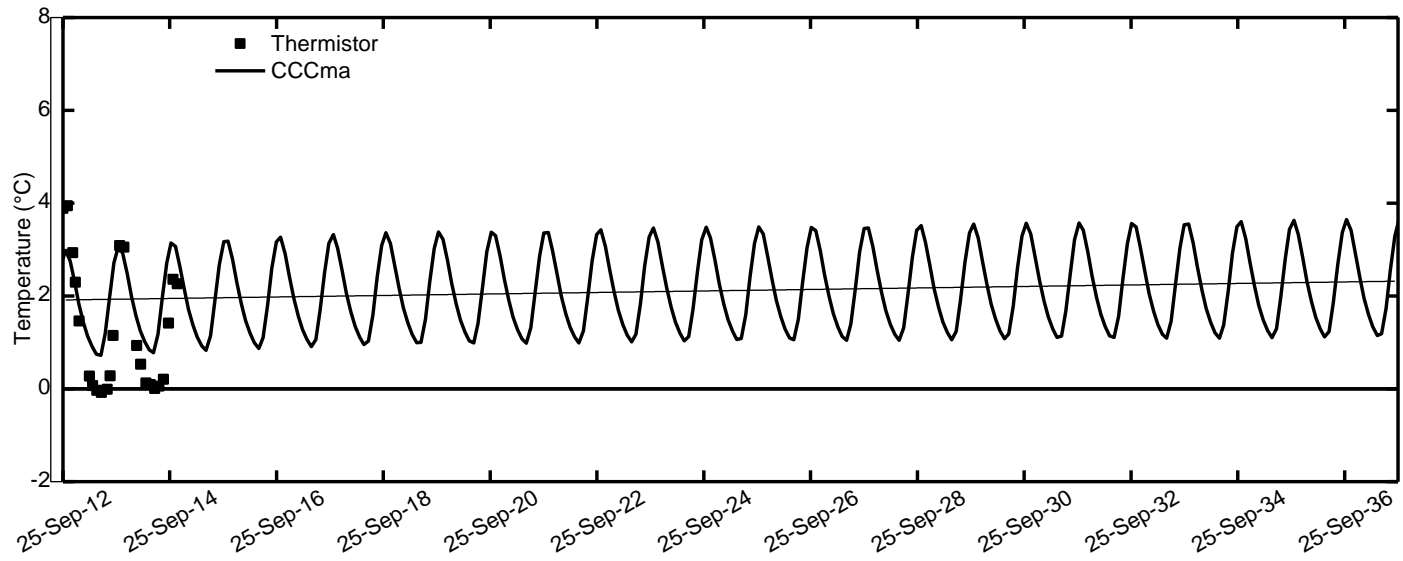
Figure 5.18: Temperature versus time for 25 years at 3.0 m below the shoulder of the embankment
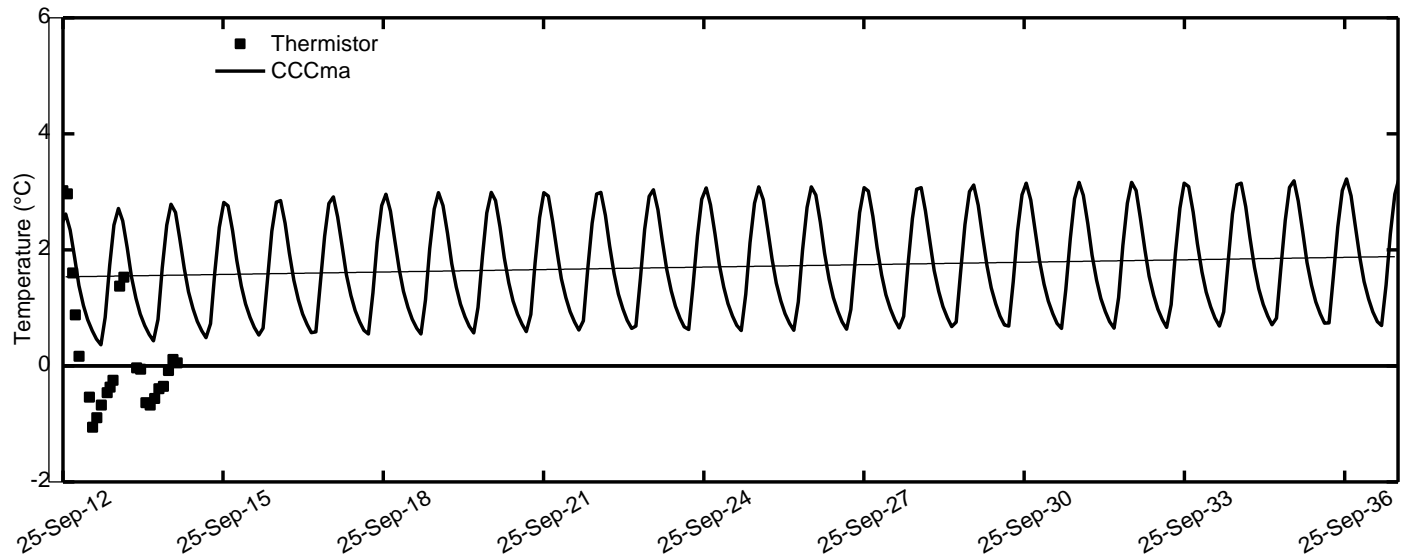
Figure 5.19: Temperature versus time for 25 years at 2.0 m below the centreline of the embankment

155
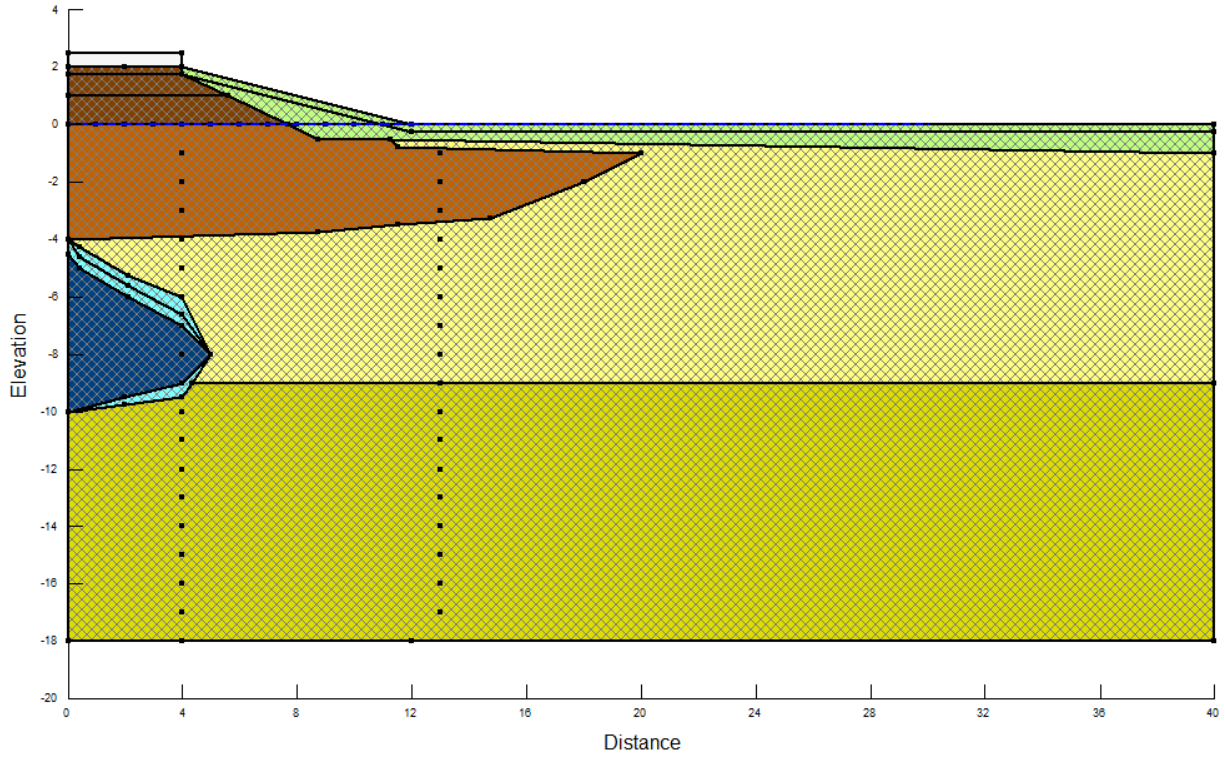
Figure 5.20: SIGMA/W Model Cross Section of the PR 391 Embankment Project Site
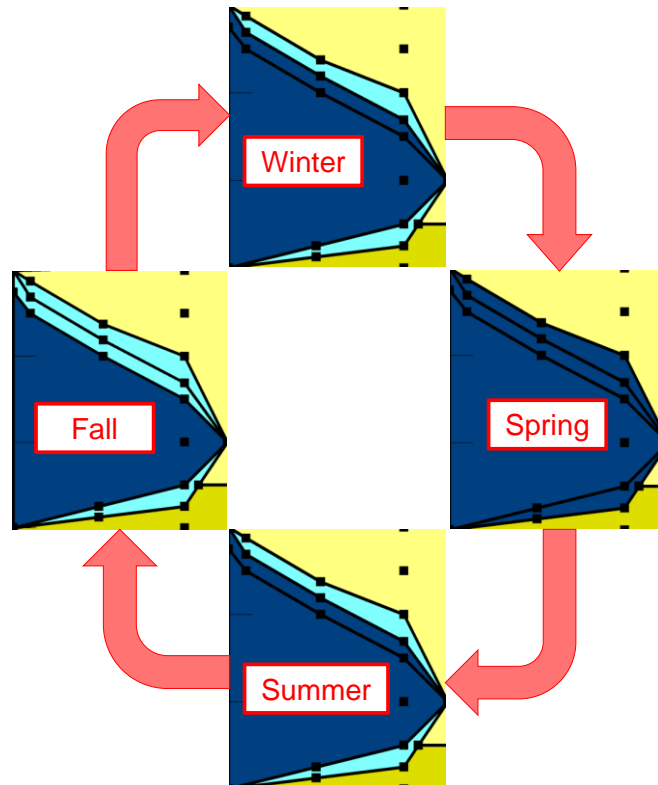
Figure 5.21: SIGMA/W Model. Seasonal changes in the frost bulb region.
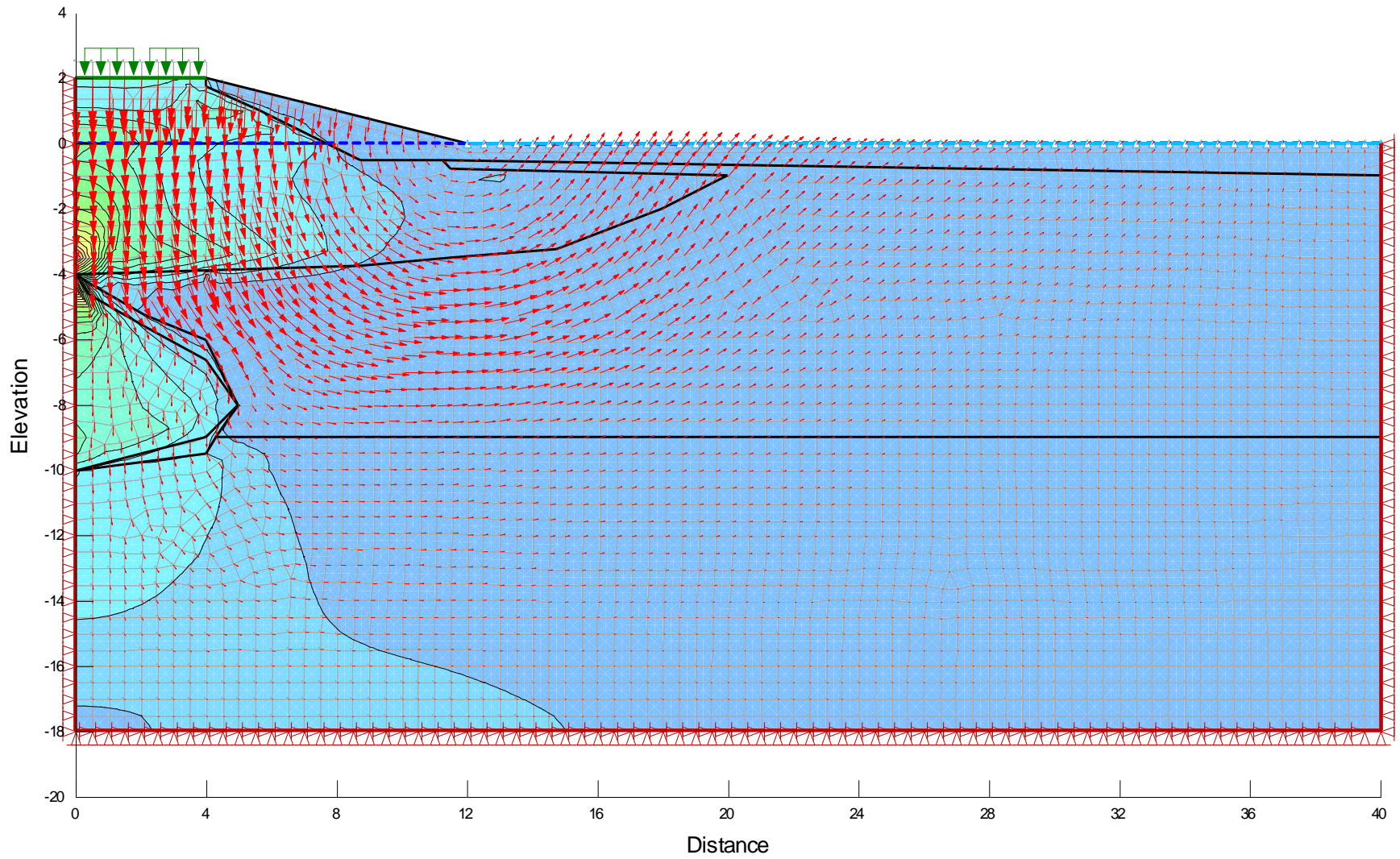
Figure 5.22: SIGMA/W Model after 720 days (to end of Summer 2014) showing Deviatoric Stress Contours with Deformation Arrows. Deviatoric stresses increase in 500 kPa contour intervals beginning at 0 kPa from lowest (blue) to greatest (red).
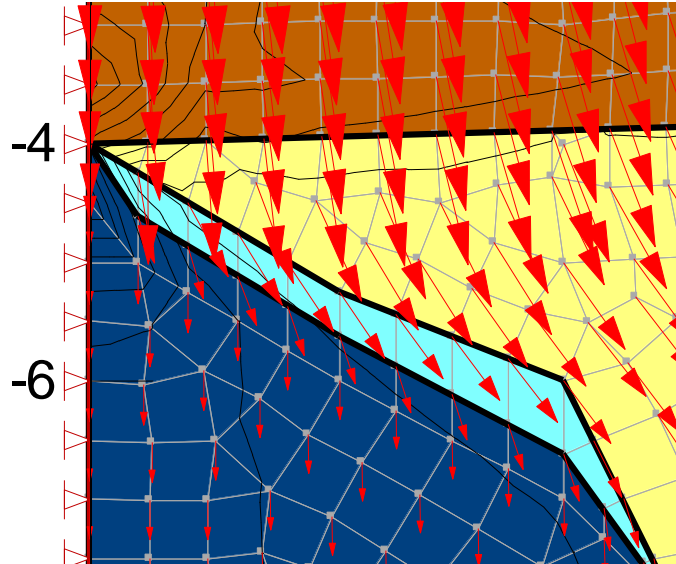
Figure 5.23: SIGMA/W Model after 720 days. Increased magnification showing increased outward lateral deformation on the top edge of the frost bulb arrows.
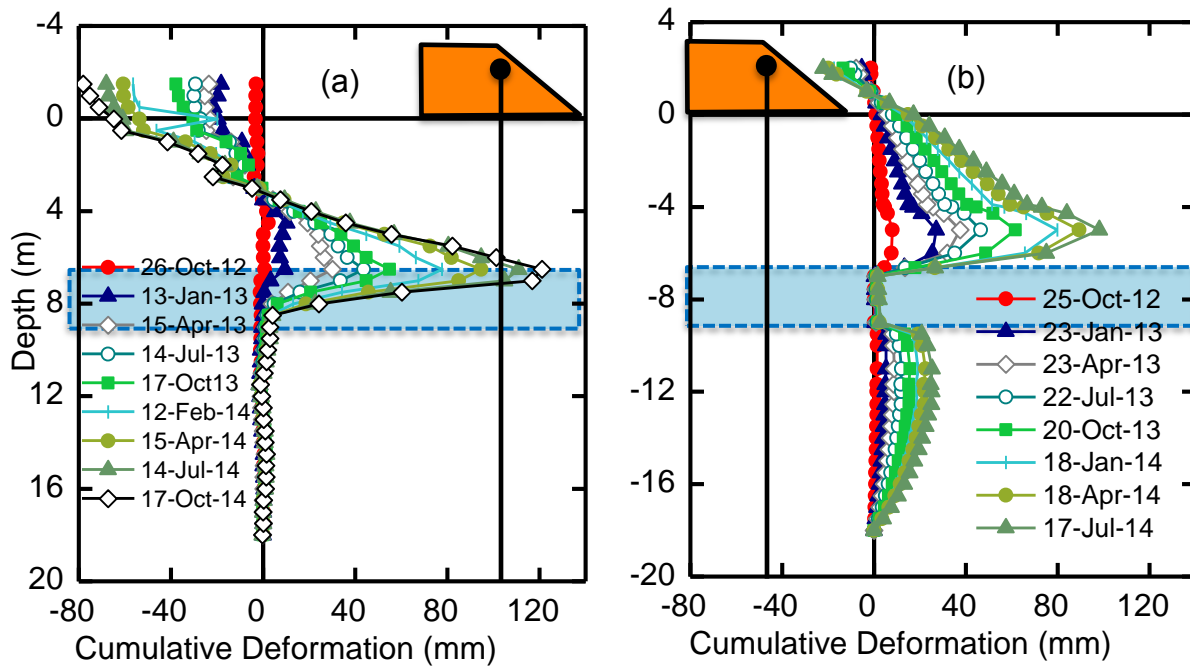
Figure 5.24: SIGMA/W Model. Lateral Deformations at the Shoulder Results from (a) the SAA and (b) the SIGMA/W Model. The location of the frost bulb is indicated by the blue region.
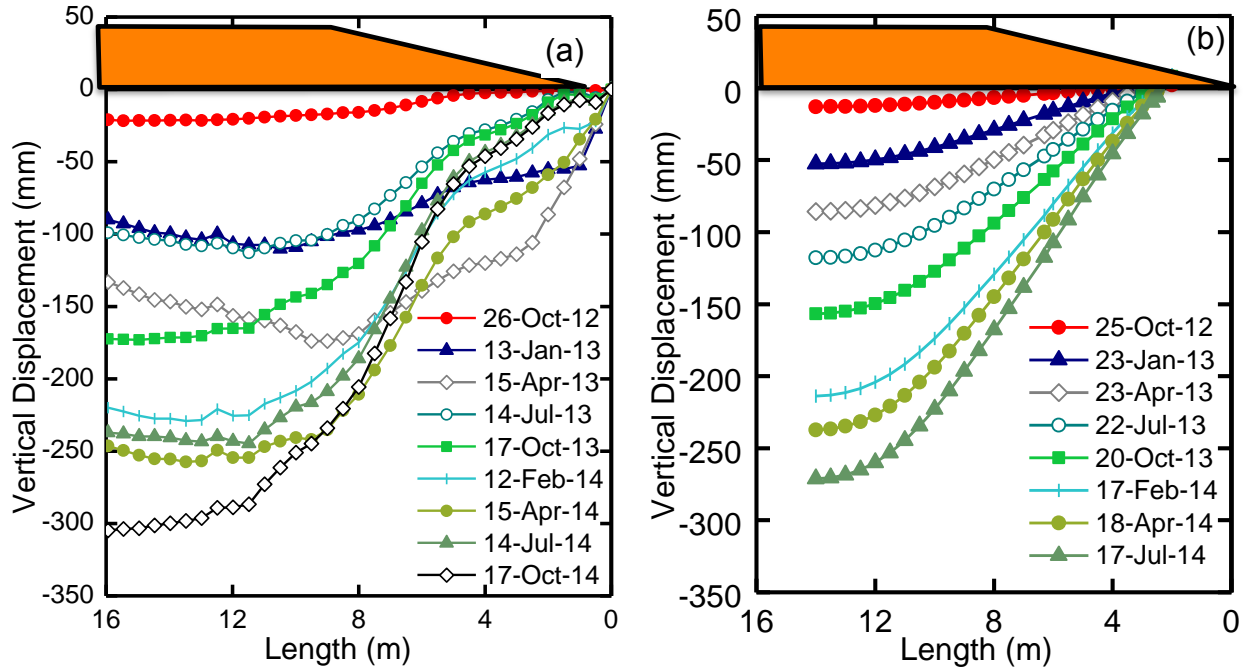
Figure 5.25: Horizontal Movement under the embankment from the toe to the centreline from (a) the SAA and (b) the SIGMA/W Model.
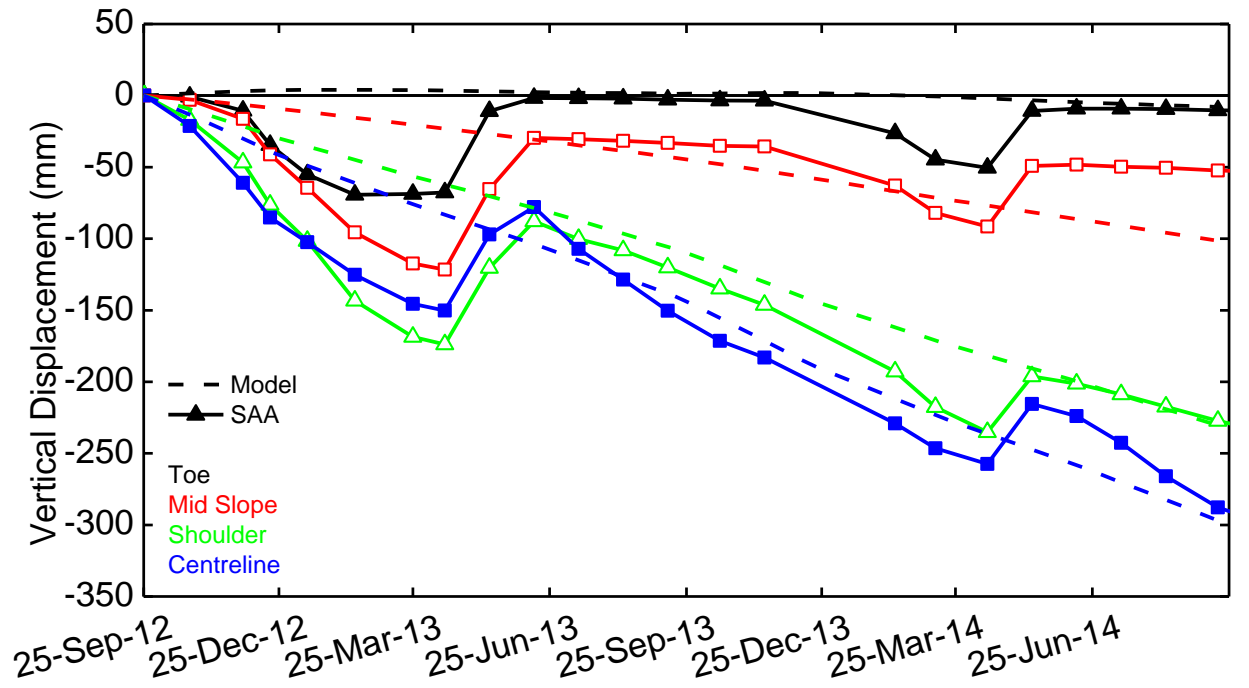
Figure 5.26: Horizontal Movement versus time at the toe (black), mid-slope (red), shoulder (green), and centreline (blue) as measured by the SAA (solid line with symbol) and simulated by the SIGMA/W Model (dashed line).

Chapter 6: Summary, Conclusions, and Future Work

6.1 Summary

The purpose of the research project was to examine the behaviour of a highway embankment constructed in a region of degrading permafrost. The project site is located 18 km north of Thompson, Manitoba, on Provincial Road (PR) 391. The research project was the continuation of research that began at the site in October 2008 and contributed to two Ph.D. theses (Batenipour, 2012; Kurz, 2013). The new research carried out by the author examined and supported two hypotheses outlined in Chapter 1. The first hypothesis stated sections of frozen ground (frost bulbs) were still present under the existing PR 391 embankment. The second hypothesis stated that the dominant operating mechanism for the settlement of the PR 391 embankment, in addition to thaw consolidation, was associated with the shear strains of the thawed soils along the top edge of the frost bulb. The research consisted of a geotechnical site investigation, field instrumentation installation, data collection and monitoring, laboratory testing, and numerical modelling.

In September 2012, new instrumentation was installed in the embankment to supplement the original instrumentation from October 2008. Thermistor strings were installed at the toe, mid slope, shoulder, and centreline of the embankment to measure temperature. Vibrating wire (VW) piezometers were installed at the toe and centreline of the embankment to measure pore water pressures. ShapeAccelArrays (SAA) were installed vertically at the shoulder and horizontally between the toe and centreline of the embankments. The SAAs measured displacements of the embankment laterally and vertically.

A remote monitoring system was developed and installed to collect data from the project site and to have access to those data at any time from any location. The project site was located

off the electrical grid so the data acquisition system was powered by solar energy. A satellite system made it possible to communicate with the data acquisition system from any location with an internet connection. The author took steps to address communication issues that flared up in the winter due to cold temperatures and snow accumulation.

Four-inch (101.6 mm) Shelby tube soil samples were taken during drilling in September 2012. Soil specimens underwent an extensive laboratory testing program that included water content, hydrometer analysis, Atterberg limit tests, one-dimensional consolidation oedometer tests, and consolidated undrained triaxial tests. The results supplemented the extensive laboratory testing that had been performed by Batenipour (2012) that used two-inch (50.8 mm) diameter specimens.

One key aspect of the research project undertaken by the author was the advancement of the numerical modelling of the PR 391 embankment. Batenipour (2012) and Kurz (2013) initially developed the thermal models using thermistor data from the toe and mid slope for model calibration. The author improved the thermal modelling by adding the newly available thermistor data at the shoulder and the centreline. In addition, available time-series were longer, allowing for a more accurate model validation. Thermal modelling was performed to simulate the thermal regime and to examine its current behaviour, as well as to make long-term projections about the degradation of the frost bulb as environmental conditions change. The load-deformation numerical model was a new development by the author for examining the deformation behaviour of an embankment under degrading permafrost. The annual freeze-thaw cycle changed the size of the frost bulb. The model examined how the frost bulb affected the lateral and vertical displacements in the embankment, and the frost bulb's impact on the long-term deformation performance of the embankment

6.2 Conclusions

The following conclusions were made based on the research conducted:

(1) Thermistor data confirmed the presence of permafrost in the form of a frost bulb under the PR 391 embankment. Sub-zero temperatures were consistently recorded at the shoulder between 7 and 9 m depth and at the centreline between 4 and 10 m since data collection began in September 2012. The presence of the frost bulb at the shoulder and centreline was also confirmed during drilling in September 2012.

(2) The displacements experienced by the embankment resulted from shear strains along the top edge of the frost bulb where thawing had taken place, in addition to thaw consolidation of the embankment. The SAA recorded the maximum outward, lateral displacement at the top edge of the frost bulb. The lateral displacement was negligible below the frost bulb. The downward vertical displacements were much more significant at the centreline than at the toe. An upward spike in displacement during the spring was related to the change in ground water conditions at the toe and swelling of the clay layer under the frost bulb. Frozen ground, like the frost bulb under the embankment, is less compressible than unfrozen and thawed ground. The load-deformation numerical model replicated the general displacement trends. Lateral displacements were restricted by the frost bulb. Additionally, the model demonstrated that shear strains developed along the weaker top edge of the frost bulb where thawing had occurred. Consequently, the greater downward displacements at the shoulder of the embankment were translated laterally away from the centreline along the weaker, thawed top edge of the frost bulb.

(3) The 'Canadian Centre for Climate Modelling and Analysis' thermal numerical model ('CCCma' model) predicted degradation and the eventual disappearance of the frost bulb

under the embankment. Though the model was unable to simulate the current state of the frost bulb, early indications show warming trends that are consistent with the predicted rise in air temperatures used by the 'CCCma' model. The degradation and eventual disappearance of the frost bulb may occur in the next twenty five years could lead to excessive deformation in the long-term performance of the embankment.

(4) The theorized improvement in testing precision and accuracy due to reduced edge effects associated with larger diameter specimens was not observed during laboratory tests. Consolidated undrained triaxial tests performed on the larger four-inch (101.6 mm) diameter specimens did not demonstrate a noticeable improvement on the results performed on the more conventional two-inch (50.8 mm) diameter specimens.

6.3 Future Work

The following suggestions are made by the author for future research work at the project site based on the work and conclusions of this research project:

(1) The next generation of thermal models requires a re-evaluation of the applied boundary conditions and material properties to enhance simulation of the frost bulb in the model. Future laboratory work could determine thermal properties of the gravel or the silty clay at various lateral or vertical extents. Other variables that are more difficult to incorporate in a model include snow clearing on the road, snow accumulation along the embankment slope, and solar radiation. Solar radiation depends on the direction the embankment faces, and a thermal model of the full cross-section using temperature data from both sides of the embankment could be developed to address the asymmetry of the highway embankment. The model has difficulty simulating the sub-zero temperatures of the frost bulb. Other finite element software could provide a better way to estimate the behaviour

163

of thermal properties near freezing temperatures. Future thermal models could enhance the simulation with 3D modelling in other finite element software such as SVHEAT.

(2) Future numerical models could couple thermal and mechanical analyses with groundwater conditions. In a coupled analysis, strength parameters are a function of temperature. At the moment, only thermal-hydro and hydro-mechanical models are possible in GeoStudio, but the company is working on a thermal-mechanical model. Ground water plays an important role in permafrost. Piezometers have collected pore water pressures at the centreline and the toe of the embankment. The only hydraulic boundary conditions applied in the author's load-deformation model were a water table and potential seepage face. In general, the flow of water at the site is not well understood. A thermal-hydro-mechanical coupled numerical model could be developed to simulate thermally induced displacements and convective heat flow from seepage.

(3) Manitoba Infrastructure and Transportation (MIT) agreed to continue support for the monitoring program and data collection at the PR 391 project site. MIT should consider installing instrumentation across the entire cross section in the future. Additionally, techniques, such as air convection embankments, could be implemented to slow the permafrost degradation at the site. Continued monitoring of permafrost conditions is highly beneficial for future researchers. It is unique to have data available over several freeze-thaw cycles and makes it an invaluable source of information to examine the long-term thermal and load-deformation behaviour of the embankment. Temperatures from the initial research between October 2008 and April 2011 were extremely helpful to the author. The author hopes that the data and findings from this research will be equally valuable in the future.

Work Cited

Andersland, O.B. & Ladanyi, B. (2004). *Frozen Ground Engineering* (2nd Ed.). Hoboken, USA: John Wiley & Sons.

Arctic Monitoring and Assessment Programme (AMAP). (2012). *Arctic Climate Issues* 2011: Changes in Arctic Snow, Water, Ice, and Permafrost. Oslo, Norway: Arctic Monitoring and Assessment Programme

Arenson, L. (2013). Permafrost Engineering 101. *CIVL 7450 Soil Properties and Behaviour*. Winnipeg, Canada: University of Manitoba.

ASTM D422 – 63 (Reapproved 2007), 'Standard Test Method for Particle-Size Analysis of Soils', Annual Book of ASTM Standards. American Society for Testing and Materials.

ASTM D2216 – 10, 'Standard Test Methods for Laboratory Determination of Water (Moisture) Content of Soil and Rock by Mass', *Annual Book of ASTM Standards.* American Society for Testing and Materials.

ASTM D2435/D2435M – 11, 'Standard Test Method for One-Dimensional Consolidation Properties of Soils Using Incremental Loading', *Annual Book of ASTM Standards.* American Society for Testing and Materials.

ASTM D4318 – 10, 'Test Method for Liquid Limit, Plastic Limit, and Plasticity Index of Soils', Annual Book of ASTM Standards. American Society for Testing and Materials.

ASTM D4767 – 11, 'Standard Test Method for Consolidated Undrained Triaxial Compression Test for Cohesive Soils', *Annual Book of ASTM Standards.* American Society for Testing and Materials.

Batenipour, H., Kurz, D.R., Alfaro, M., Graham, J. & Kalynuk, K. (2010). Results from an Instrumented Highway Embankment on Degraded Permafrost. *63rd Canadian* Geotechnical Conference & 6th Canadian Permafrost Conference, Calgary, Canada.

Batenipour, H, Alfaro, M., Graham, J. & Kalynuk, K. (2011). Deformations of a highway embankment on degraded permafrost. 14th Pan-American Conference on Soil Mechanics and Geotechnical Engineering and 64th Canadian Geotechnical *Conference*, Toronto, ON.

Batenipour, H. (2012). Understanding the Performance of Highway Embankments on Degraded Permafrost. Ph.D. Thesis, University of Manitoba, Winnipeg, Canada.

Beaulac, I. & Doré, G. (2006). Permafrost degradation and adaptations of airfields and access roads, Nunavik, Quebec, Canada. Proceedings of the *Annual Conference* of the Transportation Association of Canada, Charlottetown, Prince Edward Island.

Berger, A.R. & Iams, W.J. (1996). Geoindicators assessing rapid environmental changes in earth sciences. *Geologie en Mijnbouw*, 75 (4): 382 – 382.

Black, P. (1991). Historical perspectives in frost heave research: The early works of S. *Taber and G. Beskow*. Hanover, United States: Dept. of the Army, Cold Regions Research and Engineering Laboratory, Corps of Engineers.

Brown, J., Ferrians, O. J., Heginbottom Jr. ,J. A. & Melnikov, E. S. (2001). *Circum-Arctic* Map of Permafrost and Ground Ice Conditions. [Online image]. Retrieved from National Snow & Ice Data Center. http://nsidc.org/data/docs/fgdc/ggd318_map_circumarctic/index.html.

Brown, R.J.E. (1967). 'Permafrost in Canada', Geological Survey Map 124A, first edition, Canada.

Brown, R. J. E., G. H. Johnston, J. R. Mackay, N. R. Morgenstern, and W. W. Shilts. 1981. Permafrost distribution and terrain characteristics. Chap. 2 in *Permafrost Engineering Design and Construction,* ed. G. H. Johnston. New York: Wiley, pp. 31–72.

Brown, R.J.E. (1997). 'Disturbance and recovery of permafrost terrain', in *Disturbance* and Recovery in Arctic Lands: An Ecological Perspective, Kluwer Academic Publishers, Dordrecht, The Netherlands.

Brown, W.G. (1963). Graphical determination of temperature under heated or cooled *areas on the ground surface*. Ottawa, Canada: Div. of Building Research, National Research Council, Canada.

Budhu, M (2007). *Soil Mechanics and Foundations* (2nd Ed.). Hoboken, United States: John Wiley & Sons.

Burns, C. (2007). Permafrost. In *Encyclopedia of quaternary science* (pp. 2191 - 2199). Amsterdam, Netherlands: Elsevier.

Canadian Centre for Climate Modelling and Analysis (CCCma). 3rd Generation Coupled Global Climate Model (CGCM3.1/T47 IPCC SRES A2 Scenario Data). 2010. University of Victoria. Retrieved October 2014: http://www.cccma.ec.gc.ca/data/cgcm3/cgcm3_t47_sresa2.shtml

Chang, X., Ma, W. & Wang, D. (2008). Study of the strength of frozen clay at high confining pressure**.** Frontiers of Earth Science in China, **2** (2): 240 – 242.

Ciro, G. (2006). A Study of Adaption Strategies for Road Embankments Built on Permafrost Affected by Climate Change. M.Sc. Thesis, University of Manitoba, Winnipeg, Canada.

Davis, N. (2001). Permafrost: A Guide to Frozen Ground in Transition. Fairbanks, United States: University of Alaska Press

Dunnicliff, J., & Green, G. (1988). Geotechnical instrumentation for monitoring field *performance*. New York: John Wiley and Sons.

Environment Canada. Historic Data: Thompson Airport Station. Environment Canada. Retrieved November 2014: http://www.climate.weatheroffice.ec.gc.ca/climateData/canada_e.html.

Farouki, O. (1986). *Thermal properties of soils*. Clausthal-Zellerfeld, Germany: Trans Tech.

Fortier, D., Arenson, L., Fujan, N., Doré, G., Varlamov, S., Zabolotnik, S., Ingerman-Nielson, T. & Laurent, J.-F. (2012). Engineering Test Sections in Permafrost Environment: Performance of Permafrost Protection Measures and Mitigation Techniques to Permafrost Degradation. Proceedings of *10th International Conference on Permafrost*. Salekhard, Russia, pp. 153 – 154.

French, H.M. (1996). *The periglacial environment* (2nd Ed.) Longman: Harlow.

Fridleifsson, I.B., Bertani, R., Huenges, E., Lund, J.W., Ragnarsson, A. & Rybach, L. (2008). 'The possible role and contribution of geothermal energy to the mitigation of climate change.' IPCC Scoping Meeting on Renewable Energy Resources (pp. 59 – 80). Luebeck, Germany.

Ge, X, Yang, Z. & Still, B. (2013) 'Mechanical Properties of Naturally Frozen Ice-Rich Silty Soils', Proceedings of the ASTM International Symposium on Mechanical *Properties of Frozen Soils*, West Conshohocken, United States, pp. 124–139.

Geo-Slope. (2010a). Stress-Deformation Modeling with SIGMA/W 2007. Calgary, Canada: Geo-slope International.

Geo-Slope. (2010b). *Thermal Modeling with TEMP/W 2007*. Calgary, Canada: Geo-slope International.

Ghahremannejad, B. (2003). Thermo-Mechanical Behaviour of Two Reconstituted Clays. Ph.D. Thesis, The University of Sydney, Sydney, Australia.

Goering, D. (2004, July 1). Thompson drive to contain permafrost protection measures. Alaska Business Monthly.

Harlan, R.L., and Nixon, J.F. (1978). Ground thermal regime. Chapter 3 in *Geotechnical Engineering for Cold Regions,* ed. O.B. Andersland and D.M. Anderson. New York: McGraw-Hill, pp. 103-63.

Harris, S. (1988). Glossary of permafrost and related ground-ice terms. Ottawa, Ont.: Permafrost Subcommittee, Associate Committee on Geotechnical Research, National Research Council of Canada.

Hauck, C. (2013). New concepts in geophysical surveying and data interpretation for permafrost terrain. Permafrost and Periglacial Processe*, 24* (2): 131 – 137.

Hayley, D.W. & McGregor, R.V. (2007). The importance of permafrost, ice and seasonally frozen ground to road systems in Canada. *23rd World Road Congress*. Paris, France.

Heginbottom, J.A., Brown, J., Humlum, O., and Svensson, H. (2012) Permafrost and Periglacial Environments. In Williams, R.S., Jr. & Ferrigno, J.G., (Eds.), *State of the Earth's cryosphere at* the beginning of the 21st century–Glaciers, global snow cover, floating ice, and permafrost and periglacial environments (1386–A, 546). Washington D.C.: United States Geological Survey

Hinkel, K.M., Nelson, F.E., Park, W., Romanovsky, V., Smith, O., Tucker, W., Vinson, T. and Brigham, L.W. 2003, 'Climate Change, Permafrost, and Impacts on Civil Infrastructure', United States Arctic Research Commission: Permafrost Task Force Report, Special Report 01-03.

Intergovernmental Panel on Climate Change (IPCC) (2001) *Climate Change 2001: Impacts, Adaptation, and Vulnerability* (pp. 801 – 842). Cambridge, United Kingdom: Cambridge United Press.

Intergovernmental Panel on Climate Change (IPCC) (2013) *Climate Change 2013: The Physical Science Basis* (pp. 317 – 382). Cambridge, United Kingdom: Cambridge United Press.

Jin, H., Yu, Q., Wang, S. & Lü, L. (2008). Changes in permafrost environments along the Qinghai-Tibet engineering corridor induced by anthropogenic activities and climate warming. Cold Regions Science and Technology, **53**: 317-333.

Johansen, O. (1975). Thermal Conductivity of Soils. Ph.D. Thesis, CRREL draft translation 637, Trondheim, Norway.

Kelln, C.G., Sharma, J., Hughes, D. & Graham, J. (2008*).* An improved elastic-viscoplastic soil model. Canadian Geotechnical Journal, **45**: 1356-1376.

Konrad, J.-M. & Lemieux, N. (2005). Influence of fines on frost heave characteristics of a well-graded base-course material. Canadian Geotechnical Journal, **42**: 515-527

Kurz, D, Alfaro, M, Bartley G, and Graham, J. (2012*a*). Thermal conductivity of clay and peat samples from Northern Manitoba. *65th Canadian Geotechnical Conference*, Winnipeg, MB.

Kurz, D, Alfaro, M, Graham, J, and Batenipour, H. (2012*b*). 'Thermal modeling of an Instrumented Highway Embankment on Degraded Permafrost', *65th Canadian* Geotechnical Conference, Winnipeg, Manitoba.

Kurz, D.R. (2013). Understanding the Effects of Temperature on the Behaviour of Clay. Ph.D. Thesis, University of Manitoba, Winnipeg, Canada.

Lepage, J., Doré, G. & Fortier, D. (2012). Thermal effectiveness of the mitigation techniques used at Beaver Creek Experimental road site based on a heat balance analysis (Yukon, Canada). Proceedings of *15th International Specialty* Conference on Cold Regions Engineering, Quebec City, Quebec, pp. 42 – 51.

Lide, D. (1994). CRC handbook of chemistry and physics: A ready-reference book of chemical *and physical data* (75th ed. (1994-95 ed.). Boca Raton, FL: CRC Press.

Low, P., Anderson, D. & Hoekstra, P. (1968). Some thermodynamic relationships for soils at or below the freezing point: 1. Freezing point depression and heat capacity. Water Resources Research, **4** (2): 379 – 394.

Lynn Lake. Welcome. Lynn Lake. Retrieved September 2014: http://www.lynnlake.ca/.

Manitoba Hydro. A period of growth. Manitoba Hydro. Retrieved September 2014: http://www.hydro.mb.ca/corporate/history/hep_1970.html.

McGregor, R., Haley, D., Wilkins, G., Hoeve, E., Grozic, E., Roujanski, V., Jansen, A. & Doré, G. (2010). Guidelines for development and management of transportation *infrastructure in permafrost regions*. Ottawa: Transportation Association of Canada.

Measurand Shape Advantage. (2012). *ShapeAccelArray Brochure*. Measurand Shape Advantage.

Mesri, G., Feng, T.W. & Shahien, M. (1995). Compressibility Parameters During Primary Consolidation. Invited Special Lecture. International Symposium on Compression and Consolidation of Clayey Soils, Hiroshima, Japan,

Mesri, G. & Godlewski, P.M. (1997). Time and Stress Compressibility Inter relationship. *Journal of the Geotechnical Engineering Division*, 103 (GT5): 417 – 430. pp. 201 – 217.

Natural Resources of Canada (NRC). Permafrost in Canada. Atlas of Canada. Retrieved: October 9, 2012: http://atlas.nrcan.gc.ca/site/english/maps/environment/land/permafrost/1

OMNITrax. Hudson Bay Railway. OMNITrax. Retrieved October 2012: http://www.omnitrax.com/railroads/hudson-bay-railway-company.aspx.

Regehr, J. Milligan, C., Montufar & J. Alfaro, M. 2012. Review of Effectiveness and Costs of Strategies to Improve Roadbed Stability in Permafrost Regions. *Journal* of Cold Regions Engineering, **27**: 109-131

Remchein, D., Fortier, D., Dore, G., Stanley, B. & Walsh, R. (2009). Cost and Constructability of Permafrost Test Sections Along the Alaska Highway, Yukon. Proceedings of the Transport Association of Canada Annual Conference, Vancouver, B.C., pp. 1 – 20.

RST Instruments. (2014). *Thermistor Strings Brochure*. RST Instruments.

Skempton, A.W. (1954). The pore pressure coefficients A and B. Geotechnique, 4 (4): 143 – 147.

Slope Indicator. (2013). Multi-Level Vibrating Wire Piezometer Brochure. Slope Indicator.

Smith, S.L., Romanovsky, V.E., Lewkowicz, A.G., Burn, C.R., Allard, M., Clow, G.D., Yoshikawa, K., and Throop, J. (2010). Thermal State of Permafrost in North America: A Contribution to the International Polar Paper. Permafrost and Periglacial Processes, **21**: 117 – 135.

Sun, B., Yang, L., Liu, Q., Wang, W. & Xu, X. (2011). Experimental study on cooling enhancement of crushed rock layer with perforated ventilation pipe under air-tight top surface. Cold Regions Science and Technology, **68** (3): 150 – 161.

Tarnawski, V.R. & Wagner, B. (1996). On the prediction of hydraulic conductivity of frozen soils. Canadian Geotechnical Journal, **33**: 176-180.

Ting, J. M. Martin, R.T. & Ladd, C.C. (1983). Mechanisms of strength for frozen sand. J. Geotech. Eng. ASCE 109(10): 1286 – 1302.

Williams, P.J. (1986) Pipelines & Permafrost: Science in a Cold Climate. Don Mills, Canada: Carleton University Press.

Williams, R.S., Jr. & Ferrigno, J.G., (Eds.). (2012). *State of the Earth's cryosphere at the beginning of the 21st century–Glaciers, global snow cover, floating ice, and permafrost and periglacial environments (1386–A, 546)*. Washington D.C.: United States Geological Survey

Wissa, A.E.Z. (1969). Pore pressure measurement in saturated stiff soils. J. Soil Mech. Found. Div. ASCE 95(SM4): 1063–73.

Wood, D. (1990). Soil behaviour and critical state soil mechanics. Cambridge, England: Cambridge University Press.

Wu, D., Jin, L., Peng, J., Dong, Y. & Liu, Z. (2014). The thermal budget evaluation of the two-phase closed thermosyphon embankment of the Qinghai–Tibet Highway in permafrost regions. Cold Regions Science and Technology, **53**: 229 – 240.

Xu, J. & Goering, D. (2008). Experimental validation of passive permafrost cooling systems. Cold Regions Science and Technology, **53**: 283 – 297.

Yin, J.H., Zhu, J.G. & Graham, J. (2002). A new elastic viscoplastic model for time-dependent behaviour of normally and overconsolidated clays: theory and verification. Canadian Geotechnical Journal, **39**: 157-173.

Zhang, Y.., Chen, W. & Riseborough, D.W. (2008). Transient projections of permafrost distribution in Canada during the 21st century under scenarios of climate change. Global and Planetary Change, **60**: 443-456.

Zhang, T., Baker, T., Cheng, G. & Wu, Q. (2008). The Qinghai–Tibet Railroad: A milestone project and its environmental impact. Cold Regions Science and Technology, **53**: 229 – 240.

Appendix

This thesis contains electronic files relevant to their respective chapter. These files have been made available on a CD given to Dr. Marolo Alfaro. Typically, the files are data files, MS Excel spreadsheets, Origin graphing files, PDFs, pictures, or numerical models that are not suitable to be printed. The folders in the Appendix contain the following:

Chapter 3:

- Laboratory test results, soil logs, survey data, an x-ray diffraction report (not discussed in the thesis), and the geophysical survey report

Chapter 4:

- Code: The program code and wiring schematic for the data acquisition system

- Data: Raw data for all instrumentation as well as the Origin plots of all data (laboratory tests, instrumentation, and numerical models)

- Instrument: Information relevant to the components of the data acquisition system

Chapter 5:

- SIGMA: Deformation numerical model (GeoStudio file) and the MS Excel Spreadsheet comparing the simulated and measured data

- TEMP: Four sub-folders.

- Climate: All processed Environment Canada data used in thermal numerical models

- N-factor Back Calculations: Numerical model (GeoStudio) and MS Excel spreadsheet used to determine site specific n-factors

- Thermal Model: Numerical model (GeoStudio) with three analyses and forward projection as well as MS Excel Spreadsheet comparing simulated and measured data

- Snapshot: Numerical model (GeoStudio) and MS Excel Spreadsheet used to determine approximate frost bulb size used in the SIGMA model. Also contains video file showing the change in frost bulb size

Pictures:

- All pictures placed in folders named by the date taken are from site visits and laboratory tests

Papers

- Reports and conference papers

- Summary of all site visits